DROPLET HEAT AND MASS EXCHANGE WITH THE AMBIENT DURING DROPWISE CONDENSATION AND FREEZING

by

Julian Castillo

A Dissertation

Submitted to the Faculty of Purdue University

In Partial Fulfillment of the Requirements for the degree of

Doctor of Philosophy

School of Mechanical Engineering

West Lafayette, Indiana

December 2020

THE PURDUE UNIVERSITY GRADUATE SCHOOL
STATEMENT OF COMMITTEE APPROVAL

Dr. Justin Weibel, Chair

School of Mechanical Engineering

Dr. David B. Janes

School of Electrical and Computer Engineering

Dr. Liang Pan

School of Mechanical Engineering

Dr. Suresh Garimella

University of Vermont

Approved by:

Dr. Nicole L. Key

To those who are an exemplar

ACKNOWLEDGMENTS

I would like to express my deepest gratitude to my academic adviser, Dr. Justin A. Weibel, for the continuous guidance and unconditional support during my academic journey at Purdue University. Dr. Weibel motivated me to explore new avenues to resolve the challenges I encountered while pursuing answers to research questions.

I would also like to thank Dr. Suresh Garimella for being an exemplar of academic excellence and critical thinking, as well as for serving as a member of my advisory committee. Also, I want to express my appreciation to Dr. David Janes and Dr. Liang Pan, for being members of my advisory committee. Dr. Garimella, Dr. Pan, and Dr. Janes challenged me to think about my research differently. I would also like to thank Dr. Arvind Raman for encouraging me to apply to Purdue University and for his sincere friendship, Boiler up!

To all my past and present lab mates, I would like to express my gratitude. I deeply appreciate their generosity, willingness for helping, time, and friendship. Special thanks to Dr. Susmita Dash, Dr. Carolina Mira Hernandez, Dr. Pierre Valiorgue, Dr. Simone Mancin, Dr. Xuemei Chen, Dr. Kevin Drummond, Dr. Han Hu, Dr. Aditya Chandramohan, Dr. Gaurav Paatankar, Dr. Aakraty Jain, Dr. Taylor Allred, Dr. Todd Kingston, Dr Ankur Miglani, Matthew Clark, Rishav Roy, Sara Lyons, Aadytia Candadai, Serdar Ozguc, Srivathsan Sudhakar, Kalind Baraya, Yanbo Huang, Nick Vu, Tyler Shelly, Anali Soto, and Manohar Bongarala. Special thanks to Dr. Zhenhai Pan and Yanbo Huang for collaborating in the development of the models for droplet solidification presented in this thesis.

I would also like to thank my friends Guillermo Jaramillo, Ana Carolina, José Rivera, Omar Guerra, and Heather Akin, for their unconditional support.

I would like to thank my family in Colombia; my parents Patricia Chacon and Alexander Alvarez, and sisters, Carolina Castillo, Paola Alvarez and Marcela Alvarez for their unconditional love and support. Infinite gratitude to my partner in life Alys Jordan, who is always there to remind me that things will be okay. To the Jordan family, thank you for making me feel at home.

Finally, I would like to thank the financial support for my PhD studies and research provided by the Colombia-Purdue Institute (CPI), Fulbright, Latin American Scholarship Program of American Universities (LASPAU), and the Colombian Administrative Department for Science, Technology and Innovation (COLCIENCIAS).

TABLE OF CONTENTS

LIST OF TABLES

LIST OF FIGURES

NOMENCLATURE

A	area
B	matrix containing the droplet locations and sizes
C	vapor molar concentration
c_p	heat capacity
c	vapor concentration
D	diffusion coefficient
E_{mushy}	mushy zone constant
h_s	sensible enthalpy
h_{fg}	latent heat of evaporation
h_{fs}	latent heat of fusion
H	total latent heat
j	mass flux
L	latent heat for solidification
l	characteristic length of the sample
k	thermal conductivity
N	number of droplets in the system
$\dot{m}$	condensation rate of individual droplet
m''	mass flux
$\dot{M}$	total condensation rate
$\bar{M}$	molecular weight
p	center-to-center pitch between the droplets
P	pressure
Pe	Péclet number $\left(Pe = \zeta U/D\right)$
q	heat transfer rate
q''	heat flux
$\vec{r}$	position vector

$\bar{R}$ universal gas constant

R single droplet radius

$\langle R \rangle$ average droplet radius

RH relative humidity

s length along the arc of the droplet-gas interface

S_m mass source term

S_h energy source term

S_p momentum sink term

S condensing area

t time

T temperature

U air velocity above the substrate

v droplet volume

$\vec{V}$ fluid flow velocity

w mass fraction

x ice fraction

(x, y, z) Cartesian coordinates

Greek

(α, β, ϕ) toroidal coordinates

α thermal diffusivity

β liquid fraction

δ thickness of hydrodynamic boundary layer

ε numerical stability constant

Γ diffusivity coefficient (kg/ m s)

γ volumetric thermal expansion coefficient

ξ integration variable

η condensation correction factor

θ contact angle

μ	power law exponent
ρ	density
σ	sink density intensity per unit area
$\hat{\sigma}$	accommodation coefficient
κ	extension of the region that encloses a group of droplets
τ	integration variable
υ	normalized vapor concentration field
Ψ	intensity of droplet-to-droplet interaction
Ω	sink/source intensity for a freezing droplet
ζ	thickness of the concentration boundary layer

Subscripts

1	phase 1
2	phase 2
air	air
atm	at atmospheric conditions
c	contact area between the drop and the substrate
cell	computational cell at the droplet-gas interface
dew	at the dew point
e*q*	at the equilibrium freezing temperature (0 °C for water)
exp	experiment
ice	ice phase
film	film-like growth model
g	gas (vapor/air mixture)
iso	isolated from neighboring droplets
l	liquid phase
liq	at liquidus condition
lv	liquid-gas interface
n	nucleation
norm	component in direction normal to the liquid-gas interface

plate	at the cooling plate
PSSM	point sink superposition method
rec	recalescence
ref	reference
s	solid substrate
sat	at saturation conditions
sol	at solidus condition
sub	at the substrate
surf	at the surface of the drop
sys	in the presence of neighboring droplets (system)
ther	thermocouple
∞	far field

ABSTRACT

The distribution of local water vapor in the surrounding air has been shown to be the driving mechanism for several phase change phenomena during dropwise condensation and condensation frosting. This thesis uses reduced-order modeling approaches, which account for the effects of the vapor distribution to predict the droplet growth dynamics during dropwise condensation in systems of many droplets. High-fidelity modeling techniques are used to further probe and quantify the heat and mass transport mechanisms that govern the local interactions between a freezing droplet and its surrounding ambient, including neighboring droplets. The relative significance of these transport mechanisms in the propagation of frost are investigated. A reduced-order analytical method is first developed to calculate the condensation rate of each individual droplet within a group of droplets on a surface by resolving the vapor concentration field in the surrounding air. A point sink superposition method is used to account for the interaction between all droplets without requiring solution of the diffusion equation for a full three-dimensional domain. For a simplified scenario containing two neighboring condensing droplets, the rates of growth are studied as a function of the inter-droplet distance and the relative droplet size. Interactions between the pair of droplets are discussed in terms of changes in the vapor concentration field in the air domain around the droplets. For representative systems of condensing droplets on a surface, the total condensation rates predicted by the reduced-order model match numerical simulations to within 15%. The results show that assuming droplets grow as an equivalent film or in a completely isolated manner can severely overpredict condensation rates.

The point superposition model is then used to predict the condensation rates measured during condensation experiments. The results indicate that it is critical to consider a large number of interacting droplets to accurately predict the condensation behavior. Even though the intensity of the interaction between droplets decreases sharply with their separation distance, droplets located relatively far away from a given droplet must be considered to accurately predict the condensation rate, due to the large aggregate effect of all such far away droplets. By considering an appropriate number of interacting droplets in a system, the point sink superposition method is able to predict experimental condensation rates to within 5%. The model was also capable of predicting the time-varying condensation rates of individual droplets tracked over time. These results confirm that

diffusion-based models that neglect the interactions of droplets located far away, or approximate droplet growth as an equivalent film, overpredict condensation rates.

In dropwise condensation from humid air, a full description of the interactions between droplets can be determined by solving the vapor concentration field while neglecting heat transfer across the droplets. In contrast, the latent heat released during condensation freezing processes cause droplet-to-ambient as well as droplet-to-droplet interactions via coupled heat and mas transfer processes that are not well understood, and their relative significance has not been quantified. As a first step in understanding these mechanisms, high-fidelity modeling of the solidification process, along with high-resolution infrared (IR) thermography measurements of the surface of a freezing droplet, are used to quantify the pathways for latent heat dissipation to the ambient surroundings of a droplet. The IR measurements are used to show that the crystallization dynamics are related to the size of the droplet, as the freezing front moves slower in larger droplets. Numerical simulations of the solidification process are performed using the IR temperature data at the contact line of the droplet as a boundary condition. These simulations, which have good agreement with experimentally measured freezing times, reveal that the heat transferred to the substrate through the base contact area of the droplet is best described by a time-dependent temperature boundary condition, contrary to the constant values of base temperature and rates of heat transfer assumed in previous numerical simulations reported in the literature. In further contrast to the highly simplified descriptions of the interaction between a droplet and its surrounding used in previous models, the model developed in the current work accounts for heat conduction, convection, and evaporative cooling at the droplet-air interface. The simulation results indicate that only a small fraction of heat is lost through the droplet-air interface via conduction and evaporative cooling. The heat transfer rate to the substrate of the droplet is shown to be at least one order of magnitude greater than the heat transferred to the ambient air.

Subsequently, the droplet-to-droplet interactions via heat and mass exchange between a freezing droplet and a neighboring droplet, for which asymmetries are observed in the final shape of the frozen droplet, are investigated. Side-view infrared (IR) thermography measurements of the surface temperature for a pair of freezing droplets, along with three-dimensional numerical simulations of the solidification process, are used to quantify the intensity and nature of these interactions. Two droplet-to-droplet interaction mechanisms causing asymmetric freezing are identified: (1) non-uniform evaporative cooling on the surface of the freezing droplet caused by

vapor starvation in the air between the droplets; and (2) a non-uniform thermal resistance at the contact area of the freezing droplet caused by the heat conduction within the neighboring droplet. The combined experimental and numerical results show that the size of the freezing droplet relative to its neighbor can significantly impact the intensity of the interaction between the droplets and, therefore, the degree of asymmetry. A small droplet freezing in the presence of a large droplet, which blocks vapor from freely diffusing to the surface of the small droplet, causes substantial asymmetry in the solidification process. The droplet-to-droplet interactions investigated in thesis provide insights into the role of heat dissipation in the evaporation of neighboring droplets and ice bridging, and open new avenues for extending this understanding to a system-level description for the propagation of frost.

1. INTRODUCTION

1.1 Background

Collection of water by condensation from humid air is a commonly occurring natural phenomenon also present in several engineering systems. In nature, diverse plants and animals have adapted to survive in arid regions by harvesting water from moist air [1,2]. Condensation from atmospheric air has several practical applications and is an attractive alternative supply of fresh water in arid regions [3,4]. However, due to the limited amount of water vapor present in the air, requirement of cooling power [5], and the sensitivity of condensation to environmental conditions [3,6], accurate models that predict water harvesting capacity are critical to the design of harvesting systems for maximum yield [3,7,8]. Although, enhancing mass transfer during condensation in humid air is a topic that has been previously studied [9,10], modeling approaches still require further development to account for various factors in the prediction of water harvesting performance, such as ambient relative humidity [10], sub-cooling temperature, surface properties (*i.e.*, surface roughness), and contact angle [11]. Improved modeling approaches would allow for more accurate design and scaling of water harvesting systems.

During dropwise condensation from the ambient environment, water vapor present in air must diffuse to the surface of each droplet. The spatial distribution of water vapor in the local surroundings of each individual droplet determines the total condensation rate. However, available models for dropwise condensation in humid air assume that such systems of droplets grow either as an equivalent film or that the growth of each droplet is completely isolated [12,13]; the interactions between droplets are poorly described and, consequently, predictions of total condensation rates may mismatch experimental observations[11,12].

When dropwise condensation has occurred on substrates that are exposed to sub-freezing conditions, droplets can freeze and subsequently frost propagates and can cover the substrate. The accretion of frost negatively affects several industries including power generation and transmission [14–16] , aviation [17], and ground transportation [18]. For example, frost accumulation can deteriorate the aerodynamic efficiency and power output of wind turbines [19] and can alter the aerodynamic characteristics of flight when accumulated on the surface of aircraft wings [17] which has led to plane crashes [20]. Maintaining surfaces free of ice is costly, for example, airport de-

icing and anti-icing operations is estimated to be a market worth $1.3 billion by 2020 [21]; also, highway salting has been estimated to cost $800 dollars per ton [22]. Several methods for actively removing ice are have been developed [23]. However, those methods are costly, inefficient and in many cases harmful for the environment [24]. Passively preventing the accretion of ice on surfaces is attractive because it has the potential to reduce the cost and ecological impacts of maintaining surfaces free of ice. Significant efforts have been devoted to understand the mechanisms that govern frost formation [25] and to engineer surfaces that passively prevent the accumulation of ice and frost [26–31]. To rationally design surfaces that passively inhibit the accretion of frost, a deeper fundamental understanding of local freezing and the global percolation of ice is necessary.

Condensation frosting exhibits a rich variety of interdependent phase-change phenomena that occur locally (single droplet freezing, condensation halos, dry zones and ice bridges) and globally (percolation and densification), where coupled heat and mass transfer processes occur between newly growing ice, frozen and supercooled liquid surfaces. Heat transfer processes that are driven by the difference between the substrate temperature and the equilibrium temperature of water freezing (0°C) are coupled to differences in the vapor pressure field over ice (humidity sink) and water surfaces (humidity source). These local vapor gradients between surfaces that act as sinks and sources are believed to be the driving mechanism behind ice bridging, which in turn governs the propagation of frost [32]. Thus, a surface that passively delays the propagation of frost must prevent ice-bridging by reducing ice-bridging effectiveness. One limitation in the current understating of the propagation of frost is that models that describe the local interaction between freezing surfaces and supercooled liquid surfaces are not scalable to a system of many interacting surfaces, and often rely on approximate descriptions of the strength of those interactions. Models that describe sink/source interactions between frozen and supercooled liquid droplets that occur during frost propagation are required to provide a rationale for the design of surfaces that passively prevent the propagation of frost.

1.2 Objectives and Major Contribution

The main objective of this thesis is to contribute to the understanding of dropwise condensation and frost propagation by accurately describing characteristics of both phenomena

that critically depend on the local distribution of surrounding water vapor. The specific goals that will lead to this improved understanding are:

1) develop an accurate model that predicts the local vapor distribution around groups of droplets condensing in humid air;
2) benchmark the model using numerical simulations of the diffusion equation in quasi-steady state;
3) use the model to predict droplet growth during condensation experiments;
4) develop an experimental methodology for non-intrusive thermal characterization of droplet freezing using IR thermography
5) develop a detailed model of droplet solidification that describes the interactions between a freezing droplet and its surroundings (e.g. substrate and ambient air);
6) benchmark the model for droplet solidification against the IR temperature data;
7) extend the model for the solidification of a single droplet to the sequential solidification of a pair of adjacent droplets
8) quantify the heat and mass exchange between a freezing droplet, its environment, and its neighboring droplets.

A point sink superposition method (PSSM) has been developed to model the vapor species field around a system of droplets during dropwise condensation from humid air. The model superimposes the vapor distribution profiles of each droplet as they were isolated from each other. The model assumes that droplets can be treated as point sinks with an intensity tuned to resemble the vapor concentration field around each droplet The model captures the interactions of each droplet with its neighbors and describes growth characteristics that depends on local distribution of vapor, (such as: large droplet blocking the flux of vapor to smaller droplet; and droplets near geometrical discontinuities (e.g., the edge of a substrate) growing faster than droplets surrounded by many other droplets in all directions (e.g., in the middle of a substrate).

The PSSM has been compared to the predictions of numerical simulations of the three-dimensional vapor distribution surrounding a system of droplets on a cooled substrate. The interactions between pairs of condensing droplets is studied as function of the size and distance between the droplets. As the distance between the droplets decreases, the concentration of vapor in the region between the droplet decreases, limiting the growth of the droplets. Large droplets

limit the flux of water vapor reaching smaller neighboring droplets. The ability of the model to predict numerical simulation of the condensation rate of multiple droplets is demonstrated.

Droplet condensation rates predicted by the point sink superposition method are compared against condensation experiments. Droplet growth is tracked during the condensation process in order to measure the condensation rate of each droplet, which is then compared to the instantaneous condensation rates predicted by the point sink superposition method. At the experimental conditions, model predictions of the instantaneous and temporal droplet condensation rates are investigated as function of the number of interacting droplets taken into account in the system. These droplet growth characteristics are discussed in terms of the interactions between each droplet and all of its neighbors during different stages of droplet growth. By incorporating the interaction of all the droplets, the point sink superposition method can be used as a tool to accurately predict droplet growth during dropwise condensation from humid air.

A non-invasive technique to sample the temperature on the surface of freezing droplets from the side view has been developed. This technique demonstrates that, by reducing ambient radiation during sub-freezing infrared (IR) measurements, temperature maps with high spatial resolution can be used to track the evolution of the crystallization front during droplet recalescence, as well as to resolve the temperature gradients at the surface of solidifying microliter droplets. A detailed model for droplet solidification that uses the IR temperature data at the contact line of the droplet as boundary condition and provides a full description of the driving mechanism for heat and mass exchange between a freezing droplet, the substrate, and the ambient air has been developed. This detailed model is benchmarked successfully against the IR temperature recordings during the solidification of droplets with various sizes. The temperature distributions inside and outside of the droplets are used to identify two pathways for latent heat dissipation: heat transfer through the base of the droplet and heat exchange through the droplet interface. The temperature distribution within the droplet and substrate are used to investigate the heat spreading within the substrate. Whereas the temperature, velocity, and vapor concentration fields around the droplet obtained from the numerical simulations are used to investigate the role of heat conduction, natural convection, and evaporative cooling in the heat exchange through the interface. The heat transfer rate across the base and interface of the droplet are used to determine the relative significance between these two pathways for the interaction of a freezing droplet with its surroundings. Only a small fraction of heat is lost through the droplet-air interface via conduction and evaporative

cooling, whereas the heat transfer rate to the substrate of the droplet is shown to be at least one order of magnitude greater than the heat transferred to the ambient air.

The experimental and modeling techniques developed for quantifying the pathways for heat and mass exchange between a freezing droplet and its surroundings are extended to a system of two droplets. Infrared (IR) thermography measurements of the surface temperature of the freezing droplet and its neighbor, along with high-fidelity numerical simulations, are used to calculate the amount of heat transferred to the neighboring droplet through the substrate and ambient air. The infrared temperature maps on the surfaces of the droplets are used to demonstrate that that non-uniform heat transfer at the solidification front of a freezing droplet leads to an asymmetrical solidification with the conical tip of the final frozen droplet shape shifted away from its neighbor. The temperature field inside and outside of the droplet, as well as the velocity and vapor concentration fields around the droplet obtained from the numerical simulations, are used to investigate the role of evaporative cooling at the droplet interface and heat spreading in the substrate in the magnitude of the asymmetry. The impact of droplet size on the relative severity of the asymmetry was evaluated by solidifying pairs of droplets that were similar in size (~1:1 ratio) and dissimilar in size (~10:1 ratio). A small droplet freezing in the presence of a large droplet, causes substantial asymmetry in the solidification process.

1.3 Organization of the Document

Chapter 1 contained a background for this work and introduced the motivation, objectives and major contributions. Chapter 2 contains a review of the state of the art in dropwise condensation and condensation frosting. Chapter 3 introduces the point sink superposition method (PSSM) and compares numerical solution of the diffusion of water vapor in the three-dimensional domain containing systems of droplets against predictions obtained with the PSSM. Chapter 4 provides direct comparisons of the droplet growth dynamics measured during condensation experiments from humid air against predictions obtained with the PSSM. Chapter 5 quantifies the heat and mass exchange between a freezing droplet and its environment. Chapter 6 investigates the interactions between a pair of adjacent freezing droplets on a cooled substrate. Chapter 7 summarizes the conclusions of the studies presented in the thesis and proposes future research directions.

2. LITERATURE REVIEW

This chapter reviews the current state of the art on dropwise condensation and condensation frosting phenomena in humid air and discuss strategies to develop surfaces that passively prevent the accretion of frost.

2.1 Dropwise Condensation from Humid Air

For during dropwise condensation at a set of fixed conditions (*i.e.*, ambient temperature, ambient relative humidity, and surface sub-cooling temperature), the characteristics of droplet growth are time- and space-dependent. These variations are attributed to differences in the vapor concentration field surrounding each droplet, which vary cyclically from initial nucleation of a droplet to eventual roll-off. The spatiotemporal droplet growth has been often characterized by three stages [12]–[14]. In the first stage (*i*), droplets are distributed homogeneously and the distance between the drops is relatively larger than the average radius of the droplets. A common simplification is to assume that the droplets grow as if they are isolated from one another. As time progresses and droplets grow larger, the distance between droplets decreases. When the length of the vapor concentration profiles scales to the distance between drops, and the vapor distribution profiles overlap, it has been approximated that this closely-packed set of similarly-sized droplets can be approximated as a liquid film. In the second stage (*ii*), droplets coalesce, leading to a constant surface area coverage and self-similar growth pattern. Even though the size of the droplets can be different over a broad range, it is still commonly assumed that droplet growth can be described with a filmwise-like growth approximation. As the droplets grow and the number of coalescence events decreases, the distance between droplets will increase, causing new droplets to nucleate in the bare space between the larger droplets. Two families of drops will be present on the surface, small droplets corresponding these re-nucleated droplets and large droplets that originated at earlier stages. Later, in the final stage (*iii*), droplets approach the capillary length and will roll off the surface due to gravity. In summary, within each cycle, droplets increase in size by two primary mechanisms: direct condensation of vapor at the liquid-gas interface and coalescence of multiple droplets. The growth of a system of droplets by condensation has been often described by the limiting theoretical cases of filmwise-like growth for closely-spaced

droplets that compete for vapor in their surroundings or isolated growth of droplets spaced far apart.

While these simplified descriptions of the condensation process are well accepted, and have historically been an invaluable tool for explaining empirical observations, there are some specific growth characteristics that cannot be reasonably captured. For example, it has been observed that equally sized neighboring droplets growing in close proximity to each other have condensation rates up to 40% lower than predicted by isolated droplet growth models [11] and small droplets experience a reduced rate of growth when in close proximity to large droplets [16]; both phenomena are attributed to blocking of the lateral flux of vapor to the droplets[15]. Local vapor distribution has also been shown to play a fundamental role in understanding several freezing phenomena such as inter-droplet ice bridging [16], [17] and frost halos [32]. Also, geometric discontinuities such as surface edges and corners can also lead to changes in the vapor concentration filed around the droplets which can dramatically affect the rate of growth. Medici *et al.* [12] observed that droplets near the edges or a corner of a substrate grew ~500 % faster than a droplet near the center. In general, the total rate of condensation on a surface depends on the distribution of vapor in the surroundings that is governed by interactions within the entire set of droplets on the surface as well as the substrate boundaries, which is time- and space-dependent; modeling approaches are required that can capture all of these transport complexities.

At a given instant during the condensation process, the condensation rate of each individual droplet on a surface could be calculated by numerically solving the diffusion equation for the entire domain; however, due to the large number of differing size droplets, numerically modeling dropwise condensation in this multi-scale domain is rarely employed. Analytical solutions for the diffusion equation are available for the case of a single isolated droplet [38], but this approach is only applicable for the condensation of droplets separated by large distances [11], which might rarely occur under practical conditions. To account for interactions between droplets in the vapor concentration field, superposition methods have been used to describe the evaporation of suspended droplets during combustion [39]. Annamalai *et al.* [40] assumed suspended drops can be treated as point vapor sources to develop a point source method that solves for the evaporation rate of multiple droplets by superimposing Maxwell's solutions for the evaporation of individual droplets. The literature lacks a model that takes into account droplet interactions when solving the vapor concentration field during dropwise condensation of humid air on a substrate.

2.2 Condensation Frosting

Condensation frosting occurs in three distinct stages: supercooled dropwise condensation, onset of freezing, and percolation.

2.2.1 The Onset of Freezing

Individual droplet freezing has been observed to occur in four distinct steps [41–43]: (1) ice-embryo nucleation, (2) recalescence, (3) solidification/freezing and (4) cooling of the frozen droplet. Figure 2.1 shows a schematic representation of the droplet temperature evolution during freezing, with each of these steps indicated. After the substrate has been cooled below the dew point (T_{dew}) and water has condensed on the substrate, droplets can remain in their liquid state below the equilibrium freezing temperature of water (T_{eq}) due to the degree of supercooling required for the nucleation of an ice embryo.

Nucleation occurs stochastically within any droplet [41] and more commonly will occur heterogeneously at the contact surface between the droplet and the substrate; in some cases, nucleation near the liquid-air interface can be induced by evaporative cooling [44]. After an ice embryo has nucleated, a fraction of the liquid droplet rapidly solidifies, releasing the latent heat of fusion which is partially absorbed by the rest of the liquid droplet. As a result of this process called recalescence which is labeled with (2) in Figure 2.1, the temperature of the droplet increases rapidly to the equilibrium freezing temperature (T_{eq} = 0 °C for water) in approximately t_{rec} ~ 10 ms depending on the size of the droplet [42,43]. Since recalescence is a rapid process controlled by the kinetics of dendritic ice formation, the sudden increase of temperature is often assumed to occur adiabatically [45]. Thus, the fraction of ice created during recalescence has been estimated by balancing the latent heat released with the sensible heat required to heat the droplet from subcooled temperature at which recalescence occurs (T_{rec}) to the equilibrium freezing temperature (T_{eq}) [46]. However, droplet freezing on substrates with low thermal conductivity can exhibit some evaporation as result of the sudden increase in temperature during recalescence [47]. Mass and heat transfer studies during recalescence are needed to accurately determine the fraction of ice formed and the mass and heat that could be released to the ambient via evaporation.

Immediately after the very rapid partial freezing of the droplet during recalescence, a freeze front propagates from the bottom of the droplet to the top, freezing all the liquid remaining from

recalescence [25,42,44,47–54]. In the absence of advective flow of the air above the droplet, freeze front propagation results in a droplet with a symmetric conical tip [59], [62] that is independent of the contact angle the substrate temperature [63] as depicted in Figure 2.1. Different from recalescence, the kinetics of freeze front propagation is limited by the rate at which heat is dissipated to the substrate by conduction and to the environment by convection [25,47]. As a result, the time required for complete freezing (t_f) is significantly slower than the time to complete recalescence (t_{rec}), with $t_{rec} \approx 0.2t_f$ being considered as a good estimate [42,46]. Single droplet freezing experiments have shown that t_f can vary from fraction of a seconds to tens of seconds (0.2 ms < t_f <10 s), depending on contact angle and the size of the droplet (10 μm < R_c < 1 mm) [42], [51], [57], [46].

Even though significant efforts have been made on predicting freeze front evolution and t_f by simulating heat transfer and fluid flow during droplet freezing, less attention has been devoted in determining heat loss and mass transfer to the environment (*e.g.* evaporation of liquid during freezing). Feuillebois and co-workers [49,50] derived analytical functions to estimate t_f by solving simplified Stefan problem on droplets with fixed shapes. Chaudhary and Li [42] numerically solved the enthalpy-based heat conduction equation and considering the effect of initial fraction of ice from recalescence. Their simulations were compared to the top-most droplet temperature to determine the freezing time t_f strong dependency with on T_{rec} and θ. Vu *et al.* [54] used a front-tracking method to numerically solve for droplet solidification in a cooled plate. Their numerical approach was able to simulate changes in volume and variation of droplet shape during freeze front propagation. Zhang *et al.* [57] used the equivalent heat capacity method and consider the variation of thermal properties with temperature to predict the effect of contact angle in freezing time. Later Zhang *et al.* [58] included as initial condition to their model the effect initial fraction of ice and pre-recalescence temperature. Their simulations accurately predict the evolution of solidification front and the freezing time during experiments.

The lack of a complete characterization of the heat conduction through the droplet has limited direct comparisons with numerical simulations. Chaudhary and Li [42] inserted thermocouples along the vertical direction of a freezing droplet, their results indicate that the temperature above the front remains at 0 °C for during most of the solidification process while

solid part of the droplet below the front cools down to the temperature of the substrate as in the illustrated in Figure 2.1 (b). Hu and Jin [59] used laser-induced phosphorescence to measure temperature distribution within a freezing droplet. The absolute values of the temperature measured were off by several degrees in comparison with previous reports. Nevertheless, their results show that negligible temperature gradients exist in the water-ice mix above the freeze front. Wang *et al.* [60] reported side view IR temperature measurements of the surface of a freezing droplet, where droplet temperature wrongly increased above T_{eq} = 0 °C after recalescence, possibly as a result of spurious reflection of thermal radiation from the environment. One limitation of the simulation approaches mentioned above is that heat and mass transfer through the droplet-vapor interface was neglected. To the date, the temperature gradients occurring during droplet freezing have not been determined accurately, which has prevented validation of the models and numerical solutions of single droplet freezing existing in the literature and have limited the study of thermal coupling of the droplet with the substrate and with the air above the droplet-air interface.

Differences in the air surrounding the droplet can affect how the freeze front propagates. Jin *et al.* [52] observed freeze front progression of a droplet freezing while exposed to forced convection. They observed that an airflow moving from left to right causes the leftmost point of the front to propagate at slower rate in comparison to the rightmost point of the interface, which ends with a droplet with an asymmetric tip with respect to the center of mass of the droplet. Vu [61] reported numerical simulation of the heat transfer and fluid flow processes occurring during droplet freezing; their results suggested that asymmetries in the freezing process are caused by dragging forces deforming the volume of the droplet. Jung [44] attributed asymmetric freezing on droplets exposed to forced convection to evaporative cooling. This result suggested that asymmetric conditions (*e.g.* velocity field and vapor concentration) in the droplet-air interface could be the cause of asymmetric freezing. Studies that consider heat and mass transport through the droplet-air interface could elucidate the mechanism behind asymmetric freezing. Changes in the distribution of water vapor around the droplet also can arise from the presence of neighboring droplets as well, however these effects have not been yet investigated. Studies that account for the mass transfer occurring at the liquid-vapor interface could help to understand droplet freezing asymmetries due to changes in the distribution of vapor around the droplet.

When a sessile droplet freezes on a substrate with low thermal conductivity in a dry environment, liquid droplets that later crystalize in a frost halo can appear. This phenomena was first reported as the ejection of microdroplets by Cheng [62] in 1970 and, almost four decades later, Jung *et al.* [47] showed that frost halos result from the evaporation starting at the sudden release of latent heat after recalescence and can continue during droplet solidification. Their results indicated that the intensity of the halo depends on the percentage of the latent heat released during recalescence that is transferred to the substrate versus to the environment. Nath *et al.* [25] hypothesizes that the nucleation of the ring of microdroplets around the water/ice droplet is caused by the flux of vapor form the surface of the droplet to the substrate, with this flux being driven by the difference between the supersaturated pressure required to nucleate ice on the substrate ($p_{n,sub}$) and the saturation vapor pressure over ice at 0 °C. However, this claim has not yet been demonstrated experimentally. Models that describe condensation/frost halos are lacking in the literature; numerical studies on droplet freezing have focused on heat transfer inside the droplet [42,50,58,63], neglecting the mass transfer process occurring at the liquid-air interface. Condensation/freezing halos have only been observed during freezing of large droplets surrounded by small ones, where the effect of neighboring droplets on the distribution of vapor is negligible, studies on of freezing of a system of many are required to explain the suppression of halos.

2.2.2 Percolation

After a single droplet has completely solidified and reaches a thermal equilibrium with the substrate, a flux of vapor from the supercooled liquid neighboring droplets towards the surface of the solid droplet results from the difference between the water vapor pressure of ice and water at the same temperature. Thus, a frozen droplet acts as a water vapor sink that evaporate liquid droplets in the neighborhood. In the case where a condensation halo around the droplet occurs, the frozen droplet evaporates all the microdroplets that are part of the halo. In the absence of condensation halos, Dooley [64] first observed that frost propagates by ice bridges that grow at the expense of vapor evaporating from the nearest supercooled liquid droplets. In cases where the ice bridge connects the frozen droplet with its supercooled liquid neighbor, the neighboring droplet freezes; otherwise, the neighbor droplet is completely evaporated, creating a dry zone. Frost propagates in the directions where ice bridges are successful at connecting freezing droplet to supercooled liquid neighbors.

A water vapor pressure gradient induced by the difference between the saturation pressure above ice surface and the liquid water has been proposed as the governing mechanism responsible ice bridging. Guarrama-Cetina *et al.* [65] suggested that the growth of ice crystals during ice bridging is limited by the transport of vapor towards the frozen droplet by diffusion. In this case, the evolution of the ice bridge is determined by local vapor pressure gradient, leading to a linear evolution of the ice bridge with time. Guarrama-Cetina et al. [65] and Petit and Bonaccurso [66] observed that the ice bridge length (measured as the distance between the edge of the frozen droplet and the center of the liquid droplet) increases linearly only at early stages of growth, with velocities varying from approximately 0.5 to 1.6 μm /s, followed by a non-linear region due to an acceleration of the freezing process. Nath and Boreyko [67] used scaling analysis of the diffusion of vapor during ice-bridging between an ice droplet and a liquid neighboring droplet to estimate rate of growth of the ice bridge as:

$$v_b \sim \frac{D}{\rho_i R T_w} \frac{p_{s,l} - p_{n,i}}{\delta}, \tag{2.1}$$

where $p_{s,l}$ is the saturation pressure of the liquid droplet and $p_{n,ice}$ the vapor pressure adjacent to the growing ice bridge and the interface of the ice droplet and δ is the distance between the surfaces of the frozen droplet and it neighboring liquid droplet. Equation (2.1) suggest that the velocity of propagation is proportional to the rate of evaporation of the neighboring water droplet and to $\left(p_{s,l} - p_{n,ice}\right)$, where $p_{s,l} > p_{n,ice}$ for ice bridges to occur. However, it is not clear in the literature whether $p_{n,i}$ is saturated [68–71] or supersaturated [72–76]. Nath and Boreyko [67] measured ice bridging velocity to estimate the vapor pressure at the ice-vapor interface. Their results suggested that the vapor pressure over a growing frost layer cannot be supersaturated and therefore must be smaller than the saturation pressure above water $p_{s,l}$. Nonetheless, ice bridging occurs in the presence of several droplets in its surroundings, which can significantly reduce the concentration of vapor around the freezing droplet. Thus, an accurate description of the vapor distribution in a system of many droplets where one droplet freezes are required to accurately describe the velocity of ice-bridge propagation.

Local heating of the substrate caused latent heat released during droplet freezing has also been studied as a possible mechanism responsible for the evaporation of neighboring droplets. Chavan *et al.* [46] estimated the latent heat released into the substrate by measuring the freezing time of droplets of different size resting on surfaces with different thermal conductivities, and used it to numerically calculate the heat transferred to a hypothetical neighboring droplet. The results of their numerical simulations suggested that the latent heat transferred form the freezing droplet to the neighboring droplet accounts for a small fraction of the evaporation, even during inter-droplet ice bridging, in accordance with Nath and Boreyko [67] scaling analysis described in equation (2.1). Experimental characterization of the heat transfer processes occurring during inter-droplet ice are lacking in the literature; measurements of the temperature evolution of frozen droplets, ice-bridges and evaporating droplets could elucidate the role of heat transfer in inter-droplet ice bridging.

In-plane propagation of frost occurs after the first droplet freezes, which likely occurs near the edge of the surface [65], ice bridges propagate and form frost over the substrate. The direction in which frost percolates depends on the ability of an ice bridge to connect to a liquid neighbor droplet before it evaporates completely. Thus, the size and distance of the neighboring droplets controls whether or not frost will propagate from a frozen droplet to its nearest neighbor. Boreyko and Collier [26] used scaling analysis to derive a criterion for the propagation of frost via ice bridges for a pair of droplets given as $S^* = L_{\max} / d$, where $L_{\max}$ is the distance between the edge of the frozen droplet and the center of the liquid droplet and the d is the initial projected diameter of the liquid droplet before evaporation. Thus, an ice bridge will connect a frozen droplet with its neighboring droplet only for values of $S^* < 1$. Otherwise when $S^* > 1$, the neighboring droplet will evaporate completely before the bridge connects the two droplets, leading to a dry zone around the frozen droplet.

On substrates with high thermal conductivity, the time scale of individual bridge growth is much greater than the time scale of single droplet freezing. Droplets freeze faster on substrates with high thermal conductivity. However, the time scale for frost propagation depends on the time scale of ice bridging. A typical time scale for the percolation of frost varies between 1-10 s and is given by the ratio between the average separation between the droplets surfaces $\langle \delta \rangle$ and the rate of growth of the bridge v_b ($\tau_b \sim \langle \delta \rangle / v_b$) [25,26,65,66]. Thus, the velocity of propagation can be

controlled by tuning inter-droplet distances. One possible approach is to spatially control nucleation sites with chemically/physically engineering micropatterning hydrophilic regions with hydrophobic background [27,77,78]. However, controlling nucleation sites is not sufficient to control the speed of propagation of frost since spatial control is break after droplets have grown enough to coalesce beyond the micropatterns. Boreyko *et al* [27] demonstrated that the longer the delay in the first freezing event to occur, the faster frost will propagate as a result of the shrinking spacing between droplet surfaces. The percolation of in-plane frost depends on spatiotemporal mass transfer processes between liquid surfaces (supercooled droplets) and ice surfaces (freezing droplets and ice bridges). Current descriptions of the dynamics of the propagation of the freezing front are reduced to sink-source interactions between either a frozen droplet and a supercooled liquid droplet or between an ice-bride and an evaporating liquid droplet. Models for ice bridging that account for the transient mass transfer between all the ice droplets and all the supercooled droplets at a system level have the potential accurately describe the describe preferential direction, magnitude and other characteristics of inter-ice propagation. The thermal characteristics of the crystallization of ice during the propagation of in-plane frost have been overlook in the literature. Non-intrusive temperature map measurements of the substrate during percolation could evidence what is global effect of latent on the dynamics of freeze front propagation. After a network of interconnected frozen droplets cover the substrate, freezing propagates in the vertical direction, growing a thicker layer of ice. This out-of-plane growth of ice often called densification has been extensively studied; Léoni *et al*. [79] reviewed the current state of the art.

Ice-bridging is the main mechanism through which in-plane frost propagates. Nath and Boreyko [67] suggested that a surface capable of passively delaying or even completely halting frost must promote the failure of ice-bridging. This is made possible by having dry zones such that $S^* > 1$ and such that the nucleation and growth of new droplets in bare areas between preexisting droplets is prevented.

Condensation dry zones can be attained by using of hygroscopic substances such as salty water [80,81] or antifreeze glycols [28]. By spatially distributing hygroscopic humidity sinks, the distribution of vapor above the substrate is such that condensing embryos growth is suppressed temporarily [25,77]. By using scaling analysis, Guadarrama-Cetina *et al* [82] estimated the extension of the of the dry zone that a humidity sink would generate. By placing droplets at a distance such that the dry areas created by each droplet overlapped, Sun *et al.* [28] determined that

macroscopic arrays of water-hygroscopic salt or propylene, spaced less than twice of the radius of the condensation dry zone of the droplets as if they were alone, was sufficient to prevent frost for about 2 h. Later Sun *et al*. [83] controlled water vapor distribution by engineering a porous layer covering a second hygroscopic liquid infused layer to inhibit frost growth. They use finite element analysis to determine the concentration profile above the surface for a wide range of pore size and spacemen, their results indicate that vapor concentration above the substrate can be effectively controlled by changing the thickness of hygroscopic infused layer, pore size and distance. A method capable to quantitatively map the distribution of vapor in the presence of multiple humidity sinks regions could provide a rationale for the design of surfaces that passively prevent the formation of frost.

Controlling the water vapor concentration above the substrate by using hygroscopic substances can only prevent the accretion of frost temporarily. As the concentration of the solute in the hygroscopic solution decreases, the intensity of the humidity sink decreases and after few minutes the new droplets grow in the spaces between the sinks and frost propagates in the substrate [28,80]. In applications where the surface most be keep free-of-frost for longer times than the time required to dilute the sinks this technology is impractical. Given that the air above ice has a lower vapor than the air above liquid water at the same temperature, dry zones around ice surfaces have been reported [67]. Since ice can harvest vapor from its surroundings without diluting, ice itself have been proposed as a potential hygroscopic material. However, the potential application of ice in preventing the propagation of in-plane frost has several drawbacks, one of those being that ice humidity sinks will promote the growth out-of-plane frost.

Although significant progress has been made in the development of anti-frost substrates, a technology that passively prevents frost is still lacking. Advances in the understanding of the couple heat and mass transfer processes occurring during frost formation and propagation could lead to develop new strategies to create frost free substrates.

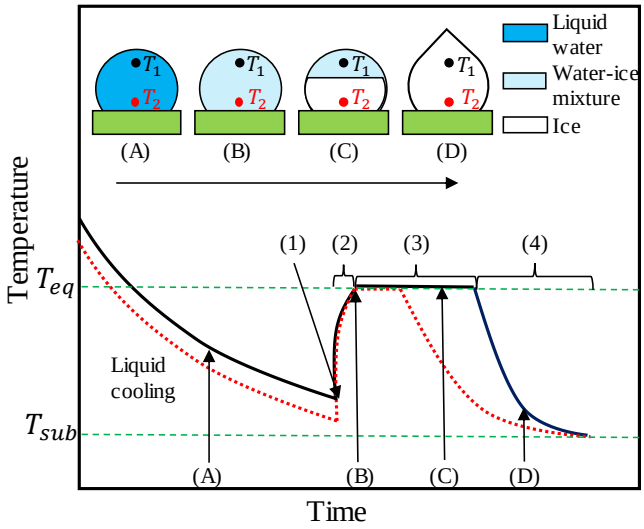

Figure 2.1. Schematic diagram of the temperature evolution during droplet freezing on a substrate that has been cooled down to T_{sub}, below equilibrium freezing temperature, T_{eq}. Two temperature traces are provided for the base (T_1, dashed red line) and the top (T_2, solid black line) of the droplet as indicated in the inset sketches. Inset droplet schematics (A)-(D) correspond to specific times within each one of the four stages of freezing (1)-(4).

3. POINT SINK SUPERPOSITION METHOD FOR PREDICTING DROPLET INTERACTION EFFECTS DURING VAPOR-DIFFUSION-DRIVEN DROPWISE CONDENSATION IN HUMID AIR

This chapter presents a modeling approach to calculate the condensation rate during dropwise condensation from humid air by incorporating the interactions between all droplets using a point sink method to superpose solutions of the vapor-diffusion-driven condensation of each individual droplet. The model requires as input the thermodynamic conditions (substrate temperature, air temperature, and relative humidity of the air), the location of the droplets, and the droplet contact angle. The model is used to predict condensation of a pair of neighboring droplets for a range of inter-droplet distances and relative sizes; the results are compared to the predictions of a three-dimensional numerical solution of the diffusion equation. This comparison is also drawn for the prediction of the condensation rate of each individual droplet in representative systems of many droplets extracted from previously reported experimental images. The model captures blocking effects due to differences in droplet size, as well as the effects of the complex spatial distribution of vapor concentration, on the condensation rate of each droplet. This compact model achieves an intermediate complexity that retains good accuracy compared to the complete numerical solution of vapor concentration field, while accounting for critical additional physical phenomena compared to alternative analytical modeling approaches. The material in this chapter was published in March 2018 in the *International Journal of Heat and Mass Transfer* [84]

3.1 Model Description

3.1.1 Condensation of an Isolated Droplet

For a droplet that is resting on a cooled surface kept at a constant temperature (T_s) below the temperature (T_∞) of the surrounding air at some relative humidity (RH), condensation of water vapor will occur on droplet surface. In quiescent air, growth of the droplet is governed by the diffusion of water molecules to this liquid-vapor interface. The concentration of water vapor $c(\vec{r},t)$ in the air surrounding the droplet obeys the diffusion equation:

$$\frac{\partial c(\vec{r},t)}{\partial t} = D\nabla^2 c(\vec{r},t) \tag{3.1}$$

The diffusion time scale for small condensing drops is of the order of $R^2/D \approx 10^{-7}$ s [85] (*e.g.*, for an initial drop radius of ~5 μm and a diffusion coefficient of 25.4×10^{-6} m^2 /s for water vapor in air), which is significantly smaller than the time scale of the growth of a droplet during condensation. Thus, the vapor concentration field adjusts rapidly compared to changes in the drop shape and the droplet condensation process can be assumed to be quasi-steady. Equation (3.1) can be rewritten as:

$$\nabla^2 c = 0 \tag{3.2}$$

The solution to this Laplace equation must satisfy the boundary conditions at the substrate, at the surface of the droplet, and far away from the droplet. The vapor concentration at the surface of the droplet $c(\vec{r}_s) = c_s$ is assumed to be equal to the saturated vapor pressure at the droplet surface temperature. This assumption is valid when there is a small temperature drop across the height of the droplet during diffusion-driven condensation; the additional effects of external convection [86], thermocapillary flows [87], and the release of latent heat [88] on the interface temperature are not considered. In the far field, the vapor concentration $c(\vec{r} \to \infty) = c_\infty$ corresponds to the vapor pressure at the air temperature and relative humidity. There is zero mass flux normal to the substrate (*i.e.* $\partial c/\partial z\big|_{z=0} = 0$). For an analogous process of droplet evaporation, where the boundary conditions are the same but the mass flux direction changes, Popov [38] provided a closed-form solution for the concentration field in toroidal coordinates. Ucar and Erbil [11] and Guadarrama-Cetina *et al.* [82] later used this solution to describe droplets growing by condensation on polymeric surfaces under the assumption that they were isolated from one another. Rewriting the solution for an evaporating droplet, the distribution of vapor in the area surrounding a condensing droplet is given by:

$$\frac{c_\infty - c(\alpha,\beta)}{c_\infty - c_s} = \sqrt{2\left(\cosh(\alpha)-\cos(\beta)\right)}\left\{\int_0^\infty \frac{[\cosh(\theta\tau)][\cosh((2\pi-\beta)\tau)]}{[\cosh(\pi\tau)][\cosh((\pi-\theta)\tau)]} P_{-1/2+i\tau}(\cosh(\alpha))d\tau\right\}$$

(3.3)

where α and β are toroidal coordinates ($0 \le \alpha \le \infty$ and $\pi - \theta < \beta < \pi + \theta$), θ is the contact angle of the droplet with the substrate, and $P_{-1/2+i\tau}\cosh(\alpha)$ is the Legendre function of the first kind given by:

$$P_{-1/2+i\tau}\left(\cosh(\alpha)\right) = \frac{2}{\pi}\coth\left(\pi\tau\right)\int_\alpha^\infty \frac{\sin\left(\tau\xi\right)}{\sqrt{2\cosh\left(\xi\right)-2\cosh\left(\alpha\right)}}d\xi \tag{3.4}$$

Equation (3.4) requires two numerical integrations with respect to τ and ξ. For the special case of a contact angle of the droplet set θ = 90 deg in equation (3.3), the solution of equation (3.3) in toroidal coordinates converges to the solution of equation (3.2) in Cartesian coordinates:

$$\frac{c_\infty - c(\alpha,\beta)}{c_\infty - c_s} = \sqrt{\frac{\cosh\alpha - \cos\beta}{\cosh\alpha + \cos\beta}} = \frac{R_c}{|\vec{r}|} \tag{3.5}$$

where $|\vec{r}| = \sqrt{x^2+y^2+z^2}$ is the Euclidian distance from the origin to any point in the domain. In general, for any contact angle, the rate of growth of a single drop $\dot{m}_{iso}$ can be obtained by integrating the flux of vapor from the surroundings at the surface of the droplet $j(r)$:

$$\dot{m}_{iso} = \frac{dm}{dt} = \rho_l \frac{dV}{dt} = \rho_l \int j(r)ds = \pi R_c D\left(c_\infty - c_s\right) f(\theta) \tag{3.6}$$

where R_c is the contact radius of the droplet. The condensation rate from the surface of the drop $j(r)$ and $f(\theta)$ are given by:

$$j(r) = \frac{D(c_\infty - c_s)}{R_c}\left[\frac{1}{2}\sin\theta + \sqrt{2}\left(\cosh\alpha + \cos\theta\right)^{3/2}\int_0^\infty \frac{\cosh\theta\tau}{\cosh\pi\tau}\tanh\left[\left(\pi-\theta\right)\tau\right]d\tau\right] \tag{3.7}$$

$$f(\theta) = \frac{\sin\theta}{1+\cos\theta} + 4\int_0^\infty \frac{1+\cosh 2\theta\tau}{\sinh 2\pi\tau} \tanh\left[(\pi-\theta)\tau\right] d\tau \tag{3.8}$$

where for small contact angles $f(\theta \to 0) \to 1$, while for large contact angles $f(\theta \to 180°) \to \infty$.

3.1.2 Point Sink Superposition Method for Vapor-Diffusion-Driven Dropwise Condensation

Due to the linearity of the Laplace equation, the solution for the vapor concentration field surrounding a system of droplets can be described as a linear combination of the solutions for individual drops. A point sink superposition method treats each condensing droplet as a point vapor sink located at the center of the droplet. The model requires as inputs the sink intensities as if they were single isolated droplets in conjunction with the size and spatial distribution of the droplets; the substrate temperature and the contact angle of the droplet are also required. Some of the additional assumptions are inherited from the single-droplet condensation model introduced in Section 3.1.1: (i) there is negligible thermal resistance across the droplet (*i.e.*, the temperature at the droplet surface is equal to the temperature of the substrate), (ii) vapor transport to the surface is governed by diffusion, and (iii) the condensation process can be treated as quasi-steady. In the two subsequent sections, the point sink method for a single condensing drop and systems of condensing droplets are introduced.

3.1.2.1 Point Sink Method for a Single Condensing Droplet on a Substrate

For a single point sink, the governing equation (3.2) transforms to a Poisson equation given by:

$$\nabla^2 c(\vec{r}) = \sigma\delta(\vec{r} - \vec{r}_j) \tag{3.9}$$

where $\delta(\vec{r} - \vec{r}_j)$ is the Dirac delta function representing a sink with density per unit area σ located at a point $\vec{r} = \vec{r}_j$. The distribution of vapor in the surroundings of a point sink can be calculated by integrating equation (3.9) from $\vec{r} = 0$ to and arbitrary location $\vec{r}$:

$$c_\infty - c(\vec{r}) = \frac{\sigma}{|\vec{r}|} \tag{3.10}$$

If the point sink is assumed to capture vapor as a droplet located at the center of a hemispherical cap, the mass absorbed by the sink should be equal to the mass crossing the area of the hemispherical cap with contact angle θ; for the case of a droplet with contact angle θ = 90 deg, the intensity is equal to $\sigma = \dot{m}_{iso}/2\pi D = R_c\left(c_s - c_\infty\right)$ as predicted from equation (3.5). In general, for any contact angle the sink intensity per unit area can be derived from equation (3.6) and it is given by $\sigma = \dot{m}_{iso}/\pi f\left(\theta\right)D$. Equation (3.10) provides the vapor concentration field in the surroundings of a single point sink with the intensity of a vapor-diffusion-driven condensing droplet with contact angle θ.

3.1.2.2 Point Sink Method for Multiple Condensing Droplets on a Substrate

For a system with N sinks at arbitrary locations $\vec{r}_j$ with j = 1, 2, 3 …, N having the condensation intensity of droplet of with contact angle θ, the concentration of the vapor at a location $\vec{r}$ in the domain due to the N humidity sinks is obtained from the superposition of the concentration contours produced by each humidity sink (developed in Section 3.1.2.1) and is given by:

$$c_\infty - c(\vec{r}) = \sum_{j=1}^{N} \frac{\dot{m}_{sys,j}}{\pi D f(\theta)} \frac{1}{\left|\vec{r} - \vec{r}_j\right|} \tag{3.11}$$

where $\left|\vec{r} - \vec{r}_j\right|$ is the distance from an arbitrary location $\vec{r}$ to the location of the j^{th} humidity sink located at $\vec{r}_j$, and $\dot{m}_{sys,j}$ is the rate of condensation of the j^{th} humidity sink in the system.

It is of interest to calculate the effect that an array of surrounding sinks would have on the condensation of a single droplet in the system. Let a point sink be replaced by a droplet i at the location $\vec{r}_i$, while all the other j locations are occupied by surrounding point sinks. The location of this droplet's surface is described by a vector $\vec{r}_{si}$ from the droplet center and the concentration of vapor at the surface of the droplet can be obtained from substituting $\vec{r} = \vec{r}_i + \vec{r}_{si}$ in equation (3.11) which results in:

$$c_\infty - c_s(\vec{r}_i + \vec{r}_{si}) = \sum_{j=1}^{N} \left(\frac{\dot{m}_{sys,j}}{\pi D f(\theta)} \frac{1}{\left| \vec{r}_i + \vec{r}_{si} - \vec{r}_j \right|} \right) \tag{3.12}$$

Because the temperatures of all droplets are assumed to be equal (at the substrate temperature), the vapor concentration at the surface of the droplet is the same for every droplet in the system, $c_s(\vec{r}_1 + \vec{r}_{s1}) = c_s(\vec{r}_2 + \vec{r}_{s2}) = .. = c_s(\vec{r}_i + \vec{r}_{si})$. While the magnitude of $\vec{r}_{si}$ is different for each point on the droplet surface, it can be assumed that this magnitude is small in comparison with the distance between the droplets $\left|\vec{r}_{si}\right| \ll \left|\vec{r}_i - \vec{r}_j\right|$. If we further assume $\left|\vec{r}_{si}\right| \approx R_{ci}$ for the term i in the summation, then equation (3.12) can be rewritten as a system of N equations:

$$c_\infty - c_s = \frac{\dot{m}_{sys,i}}{\pi D f(\theta) R_{ci}} + \sum_{j=1, j\neq i}^{N} \left(\frac{\dot{m}_{sys,j}}{\pi D f(\theta) R_{ci}} \frac{R_{ci}}{\left| \vec{r}_i - \vec{r}_j \right|} \right) \tag{3.13}$$

where i = 1, 2, … N represents each droplet location on the substrate, and j = 1, 2, … N represents the surrounding humidity sinks at each droplet location, as shown in Figure 3.1.

The solution of the condensation rate of each droplet in the system is simplified if droplet-to-droplet interaction is cast as a correction factor η given by the ratio between the condensation rate of the droplet within the system of multiple droplets versus the condensation rate of the droplet as if it was isolated:

$$\eta = \frac{\dot{m}_{sys}}{\dot{m}_{iso}} \tag{3.14}$$

where η = 1 indicates that a droplet will grow as if it were isolated. Because all the droplets are assumed to have the same vapor concentration at their surfaces, by dividing equation (3.13) by $(c_\infty - c_s)$ and using the definition of the correction factor given in equation (3.14) the system of equations (3.13) can be rewritten in terms of the correction factor η as:

$$\eta_i + \sum_{j=1, j\neq i}^{N} \eta_j \left(\frac{R_{cj}}{\left|\vec{r}_i - \vec{r}_j\right|} \right) = 1 \tag{3.15}$$

The solution of the system of equations provides the correction factor for each droplet; from equation (3.14) the condensation rate for each droplet can be obtained. Introducing the normalized concentration field as:

$$\upsilon(\vec{r}) = \frac{c_\infty - c(\vec{r})}{c_\infty - c_s} \tag{3.16}$$

and dividing equation (3.11) by $c_\infty - c_s$, the potential concentration field can be rewritten in terms of the correction factor as:

$$\upsilon(\vec{r}) = \sum_{j=1}^{N} \left(\frac{\dot{m}_{sys,j}}{\pi D f(\theta)\left(c_\infty - c_s\right)\left|\vec{r} - \vec{r}_j\right|} \right) = \sum_{j=1}^{N} \left(\frac{\eta_j R_{cj}}{\left|\vec{r} - \vec{r}_j\right|} \right) \tag{3.17}$$

Thus, the normalized concentration contour field is obtained once the correction factors have been determined from equation (3.15).

Equations (3.14) to (3.17) provide a closed-form solution for the instantaneous condensation rate and normalized local vapor concentration for vapor-diffusion-driven dropwise condensation from humid air by the point sink superposition method.

3.2 Results

3.2.1 Condensation of a Pair of Droplets

This section compares the condensation rates predicted for a pair of neighboring droplets obtained using the point sink superposition method developed in Section 42 against a three-dimensional numerical solution of the diffusion equation. The case considers two droplets resting on a substrate with a contact angle of θ = 120 deg, separated by a pitch p and contact radii R_{c1} and R_{c2}. The condensation rates are predicted for a range of contact radii varying from 10 μm to 310 μm and inter-droplet distances from 120 μm to 1140 μm. The temperature of the droplets is

assumed to be equal to the substrate temperature $T_{sub} = 5\ ^{\circ}C$, and thus the vapor concentration at the surface of the droplet is $c_s = 0.0035$ kg/m^3. The concentration at the outer surface of the domain is taken at $c_\infty = 0.00124$ kg/m^3 for 70% relative humidity at an air temperature of $T_{air} = 20\ ^{\circ}C$.

The condensation rate correction factors from the point sink method can be obtained by solving the system of equations in the Equation (3.15) for two droplets as:

$$\eta_1 = \frac{\left(1 - \frac{R_{c2}}{p}\right)}{\left(1 - \frac{(R_{c1})(R_{c2})}{p^2}\right)} \qquad \eta_2 = \frac{\left(1 - \frac{R_{c1}}{p}\right)}{\left(1 - \frac{(R_{c1})(R_{c2})}{p^2}\right)} \tag{3.18}$$

By substituting the corrections factors given into Equation (3.17), the normalized concentration field for two drops can be calculated as:

$$\upsilon(\vec{r}) = \frac{\eta_1 R_{c1}}{|\vec{r} - \vec{r}_1|} + \frac{\eta_2 R_{c2}}{|\vec{r} - \vec{r}_2|} \tag{3.19}$$

The numerical simulations are performed by using the finite volume schemes implemented in ANSYS Fluent 17.2 [89]. Figure 3.2 (a) shows the meshed spherical cap used as computational domain; the pair of droplets, which are much smaller than the overall domain, are located on the substrate in the center as shown in the zoomed view in Figure 3.2 (b). As boundary conditions, the vapor concentration was prescribed at the outer surface of the domain and on the surface of each drop, and a zero flux condition was prescribed on the substrate surface. The shape and size of the domain were chosen to ensure domain-independent results. Considering all of the different cases, a typical domain used a mesh with ~10^6 elements; a mesh independence analysis, with local refinements near the surfaces of the droplets in the regions of high concentration gradients, was performed to confirm that results of the numerical calculations were independent of the size of the elements used. The criteria for convergence was set at a normalized absolute error of ~10^{-12}.

The effects of inter-droplet distance on the condensation rate are first explored by changing droplet pitch between two droplets of the same size $R_c = R_{c1} = R_{c2}$. Figure 3.3 (a) shows the

correction factor $\eta = \eta_1 = \eta_2$ as function of the droplet pitch for all of the sizes considered. The predictions using the point sink method (shown as solid lines) closely matches the results of the numerical simulations (shown as symbols). The relative error between these two values, for all the cases considered, remains below 4%. For a selected case, Figure 3.4 shows the normalized vapor concentration field $\upsilon(\vec{r})$ at the substrate plane in a region near the two droplets; local agreement between the model and the numerical simulations is observed in the field.

Each droplet will grow as if it were completely isolated for a correction factor equal to unity; in the limit of the droplet pitch being very large $(p \to \infty)$, the droplets will have no effect on each other $(\eta \to 1)$. All of the cases shown in Figure 3.3 tend to η = 1 with increasing pitch; only for relatively extreme separation distances (*e.g.*, droplets separated by a pitch one hundred times their radii) does this value become near unity. At a given pitch, the correction factor reduces as the size of the droplets increase. If the correction factor is replotted as a function of the non-dimensional ratio between the pitch of the droplet pair and their contact radii, as shown in Figure 3.3 (b), then all of the data from Figure 3.2 (a) fall onto a single master curve for the correction factor. From Figure 3.3 (b), it can again be observed that the correction factor increases with an increasing ratio between the droplet pitch and their contact radii. This curve can be used to define a threshold separation distance at which it can be assumed that droplets of the same size have negligible interaction with each other. For example, a value of p/R_c > 25 (*i.e.*, droplets separated at a distance more than 25 times greater than their contact radii) the correction factor is η > 0.95.

The reduction of the condensation rate as the droplets become closer (*i.e.*, as the pitch decreases) is further examined in Figure 3.5 by plotting contours of the normalized concentration field $\upsilon(\vec{r})$ around the two droplets given by Equation (3.19) at the plane that coincides with the substrate at z = 0. The panels of Figure 3.5 show the results for two droplets with contact radii R_c = 60 μm at different pitches. A zone of depleted vapor emerges between the droplets that significantly reduces the concentration gradient normal to the droplet surface in the direction toward the other droplet (compared to the opposing direction). As the distance between the droplets decreases, this depletion zone becomes more severe as the maximum concentration of vapor decreases; hence, the condensation rate of each drop will be further reduced as they are brought closer. From the example case shown in Figure 3.5, two droplets with R_c = 60 μm separated by a distance equal to

p = 180 μm would condense 25% less rapidly compared to the same size isolated droplet. Even for pitches that are 9 times larger than the droplet radius, the condensation rate would be reduced by 9.5%.

The relative sizes of the droplets in the pair also plays an important role in affecting the condensation behavior. This is analyzed by considering a droplet with contact radius R_{c1} = 10 μm that is in the surroundings of a relatively larger droplet with a contact radius R_{c2}. Figure 3.6 (a) and (b) respectively show the condensation rate correction factors for these two droplets, η_1 and η_2 for R_{c2} increasing from 10 μm to 310 μm, as function of droplet pitch. The relative error between the point sink superposition method prediction (solid lines) and the numerical simulation results (data points) increases as the ratio between the droplet radii increases and the pitch is reduced; for all the cases the relative error was larger for the smaller drop.

There is a very significant reduction in the condensation rate of the small droplet as the size of the larger neighboring droplet increases (see Figure 3.6 (a)). For example, at p = 600 μm, for the larger droplet increasing in size from 10 μm to 310 μm, the correction factor of the smaller droplet decreases from η_1 = 0.98 to η_1 = 0.41. Comparatively, the correction factor for the larger droplet is universally $\eta_2 > 0.98$ for all the cases at this pitch. This can be further explained by Figure 3.7, which shows the normalized vapor concentration field $\upsilon(\vec{r})$ at the substrate for R_{c1} = 10 μm and R_{c2} = 60 μm at different pitches. The concentration field is almost entirely governed by the larger droplet, which causes the smaller droplet to lie in a zone of depleted vapor. As the large droplet comes closer, the smaller droplet has a reduced concentration of vapor available in its immediate surroundings; however, the concentration field observed from the perspective of the larger droplet is relatively unaffected.

Reduced condensation rates for small droplets in the surroundings of relatively larger droplets has previously been observed in experiments; Leach *et al*. [36] reported small droplets near larger droplets grew 20% slower compared to more isolated droplets of the same size. Depletion of vapor has also been reported as a factor causing the inhibition of droplet nucleation on the bare substrate nearby large droplets during condensation [82].

3.2.2 Condensation in a System of Droplets

This section first compares the overall condensation rates and water vapor distribution obtained for a system of multiple droplets using the point sink superposition method against a numerical simulation of the same system. The computational domain, boundary conditions, and implementation approach used for the numerical simulations are similar to those described in Section 3.2.1, but updated to accommodate more than two droplets at the center of the domain. Secondly, the point sink superposition method is used to predict the condensation rate of randomly distributed systems of droplets having size distributions resembling previously reported experimental data [10]; these predicted rates are compared against alternative reduced-order prediction methods.

To implement the point sink superposition method, the locations and sizes of the droplets in the system are inserted into equation (3.15), and the correction factor and condensation rate of each droplet are obtained by solving the system of equations. Subsequently, the normalized local vapor concentration field at the substrate is obtained by substituting the correction factors into equation (3.17). The thermodynamic conditions (*i.e.*, substrate temperature, air temperature, relative humidity and vapor concentrations) are the same as defined previously in Section 3.2.1.

3.2.2.1 Comparison of Point Sink Superposition Method Versus Prediction via Numerical Simulations

The point sink superposition method predictions are first compared with numerical simulations to verify the superposition approach for a system of multiple droplets. The system of droplets used for this comparison is shown in Figure 3.8, which contains 16 droplets and resembles a time during condensation when the drop size distribution is broad and there are larger bare spaces between the droplets. The vapor concentration field is shown for the numerical simulation in Figure 3.8(a) and for the point sink method in Figure 3.8 (b); the vapor distributions around the droplets obtained from both models are observed to be similar. The ability of the point sink superposition method to match the numerical simulations can be further investigated by comparing the condensation rates of each individual droplet, as well as the total condensation rate, predicted by both of the models, as summarized in Table 3.1. The total condensation rate error was found to be ~14%, and the error for individual droplets was generally on the same order. These findings are consistent with the comparisons presented for the case of two condensing droplets shown in Section 3.1.2.1.

Because the vapor concentration distribution around the droplets determines their condensation rate, droplets of similar size have a higher condensation rate when they are nearer the edge of the system. For example, droplet 16 in the system of droplets shown in Figure 3.8, which is located near the edge of the system, has a larger condensation rate compared to droplet 8 located near the center. The area surrounding the droplets deep in the center of the array is almost entirely depleted of vapor, and all droplets interact and significantly influence one another. This behavior, which causes droplets near the edge of the system to grow faster than droplets near the center, has previously observed by Medici *et. al.* [12]. Another unique validation case for a different system of droplets is provided in the Appendix A.

3.2.2.2 Comparison of Point Sink Superposition Method Versus Prediction via Conventional Reduced-Order Models

The condensation rates predicted for a system of droplets using the point sink superposition method, which accounts for the complete vapor diffusion behavior, is compared against condensation rates estimated using the highly simplified approaches of assuming completely isolated droplet growth or filmwise-like growth behavior, as is often employed in the literature [16,20]. The condensation rate of isolated droplet growth is obtained from equation (3.6), while the condensation rate of filmwise-like growth is obtained from a simplified one-dimensional diffusion resistance analysis. This filmwise growth model assumes that a system of closely-spaced droplets behaves as a film of equivalent condensate volume. By solving equation (3.2) in the direction normal to the surface of the film and from scaling the extension of the concentration profile to a region where the diffusion of vapor is dominant, the condensation rate of the film can be obtained as previously reported by Medici *et. al* [12].

Two different characteristic droplet systems are considered for this analysis, as shown in Figure 3.9. The system shown in Figure 3.9 (a) resembles the earliest stages of growth (*i.e.*, regime *i* as discussed in Section 2.1) after nucleation when the droplets have similar sizes and are closely spaced, while Figure 3.9 (b) resembles a later stage during condensation when there are a significant number of coalescence events (*i.e.*, regime *ii* as discussed in Section 2.1) that leads to a broader droplet size distribution. These systems of droplets are randomly generated to achieve the same droplet distribution characteristics as observed in our previous experiments [10]. The point sink superposition model is evaluated considering the entire domain area in Figure 3.9. To avoid the influence of edge effects, the comparisons only consider the condensation behavior

within a region near the center of the system (*viz.* within the dashed square shown in Figure 3.9); it was separately confirmed that this region is not affected by the edges of the domain, and therefore representative of the condensation behavior on an infinite plane.

The total condensation rates of the droplets enclosed by the dashed squares shown in Figure 3.9 are summarized in Table 3.2 (a). The total condensation rate estimated by the isolated droplet growth model severely overpredicts condensation rates obtained by the point sink superposition method for both systems. During evaluation of the point sink superposition model, the average condensation rate correction factor for the droplets within the area enclosed by the dashed square shown in Figure 3.9 (a) was found to be $\langle \eta_i \rangle = 0.13$. Droplets in closer proximity to neighboring droplets grow at smaller rates compared to droplets that are spaced further away from their neighbors. For example, the condensation correction factor of the droplet *a1* in Figure 3.9(a) is lesser than the similarly sized droplet *a2* (see Table 3.2 (b)). Large bare spaces between the droplets promote higher condensation rates for individual droplets because vapor can diffuse vertically toward the substrate and then laterally toward the peripheral of the droplets; conversely, droplets in the neighborhood block the lateral diffusion of the vapor, causing depletion of vapor, as discussed in Section 3.2.1. In comparison to the system of droplets shown in Figure 3.9 (a), the system of droplets shown in Figure 3.9 (b) has a smaller average condensation correction factor of $\langle \eta_{ii} \rangle = 0.07$ due to a reduction of the distance between droplets. There is also a broader distribution of sizes and vapor in the surrounding of relatively small droplets is depleted by large droplet neighbors. For instance, the small droplet *b1* shown in Figure 3.9 (b) has a condensation correction factor equal to $\eta = 0.02$, compared to $\eta = 0.10$ for a larger droplet *b2*. While filmwise-like growth is commonly used to characterize droplet growth in such systems, the filmwise-like condensation model can lead to errors in prediction because its intrinsic assumption of an equivalent condensate volume yields a condensing interface with a different area compared to the total surface area of the droplets; in addition, the filmwise-like condensation model heavily relies on scaling approximations to predict the concentration profile. Even though the filmwise-like condensation model provides a better prediction compared to assuming that droplets grow as if they were isolated, the filmwise-like growth model overestimates the total condensation rate by ~60% compared to the prediction of the point sink superposition method for the specific systems shown in Figure 3.9.

3.3 Conclusions

This chapter presented a methodology to calculate the condensation rates of each individual droplet within large systems of many droplets during vapor-diffusion-driven dropwise condensation from humid air. This methodology treats each individual droplet as a point humidity sink so as to allow superposition of the solutions to the diffusion equation for each individual drop. The model thereby captures the interaction between all droplets within the system, accounting for spacing between droplets and their relative differences in size (such as the effect of large droplets on blocking water vapor flux toward small nearby droplets). This methodology is shown to accurately predict the total condensation rate and local vapor distribution for systems of droplets by validation against a three-dimensional numerical solution of the diffusion equation. In comparison with highly simplified droplet growth models, *viz.*, assuming completely isolated droplets or filmwise-like growth, the critical importance of including droplet interaction effects is demonstrated by comparing to the total condensation rate calculated using the point sink method for droplet systems representative of dropwise condensation.

Table 3.1. Condensation rate of individual droplets, as well as the overall condensation rate, for the system of droplets shown in Figure 8. The error compares condensation rates from the numerical simulations to those obtained using the point sink superposition method.

Droplet Tag	$\dot{m}$ **[x10^{-12} kg/s]**		**Error [%]**
	Numerical	**Model**	
1	3.4	3.0	11.0
2	3.8	4.9	30.3
3	8.5	8.6	2.1
4	19.5	21.3	9.3
5	44.0	50.3	14.3
6	23.6	26.5	12.3
7	17.6	27.8	58.1
8	25.4	34.1	34.5
9	20.6	22.6	9.7
10	42.4	50.1	18.2
11	1.0	0.4	56.6
12	35.3	38.7	9.7
13	70.1	79.2	13.0
14	73.6	80.4	9.2
15	27.9	31.2	12.1
16	59.0	65.1	10.3
Total	**475.3**	**544.2**	**14.5**

Table 3.2. (a) Total condensation rates calculated by the point sink method, the isolated droplet growth model, and the filmwise-like growth model for the systems of droplets inside the dashed square shown in Figure 9 (a) and Figure 9 (b). (b) Correction factor for droplets a1, a2, b1 and b2.

System	$\dot{m}$ **[x10^{-10} kg/s]**		
	Isolated	**Film**	**Model**
Figure 3.8 (a)	39.2	7.9	5.1
Figure 3.8 (b)	53.3	7.9	4.7

(a)

Droplet Tag	η
a1	0.14
a2	0.09
b1	0.02
b2	0.10

(b)

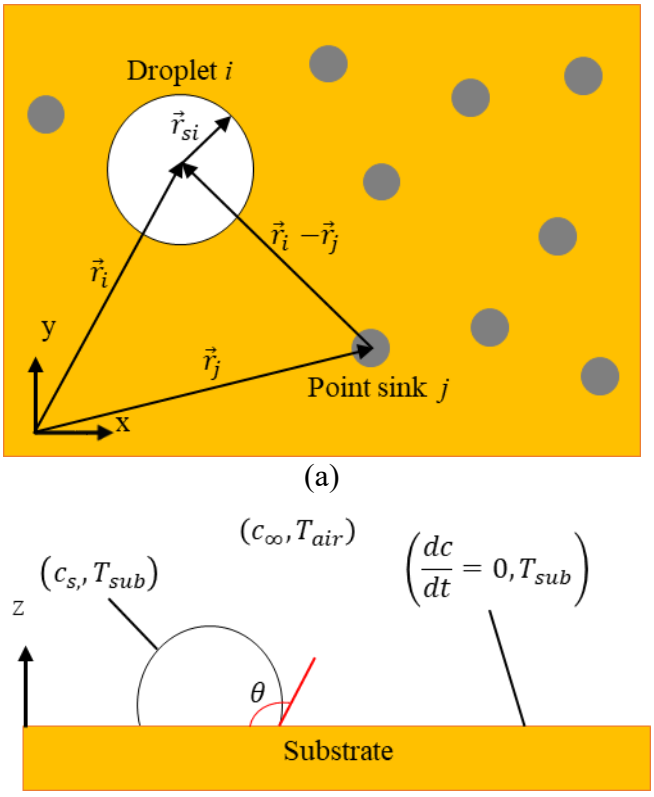

Figure 3.1. Schematic diagram of a droplet condensing on a substrate surrounded by multiple point humidity sinks: (a) the top view shows the vector position of the center droplet *i* and surrounding humidity sinks at the locations of the other droplets *j*, and the (b) side view shows the substrate, droplets, and boundary conditions.

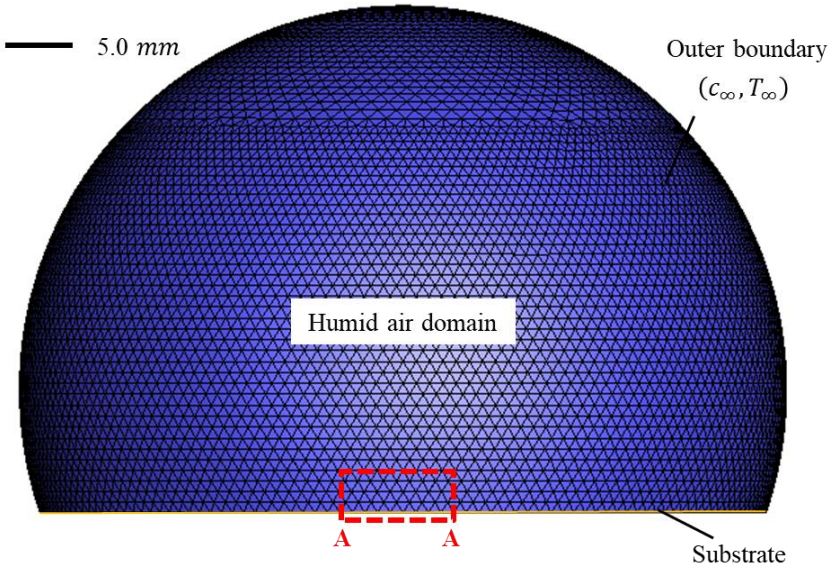

(a)

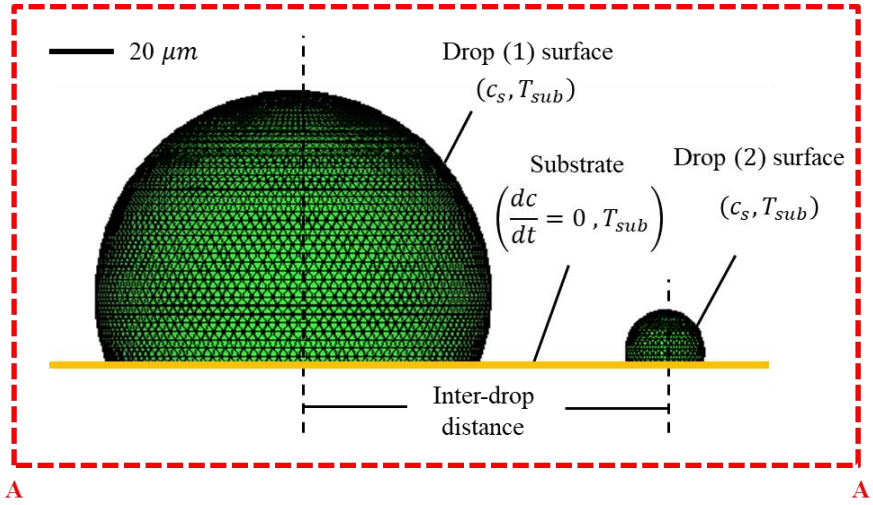

(b)

Figure 3.2. Schematic diagram of the computational domain and boundary conditions used for numerical simulation of a condensing pair of droplets. (a) The far-field outer boundary of the domain (blue surface) is represented by large spherical cap, with (b) the pair of droplets (green surfaces) located on the substrate at the center (as shown in ~250× magnified section view A-A). For the case shown in (b), the pair of droplets have contact radii R_{c1} = 10 μm and R_{c2} = 60 μm and are separated at a distance p = 110 μm.

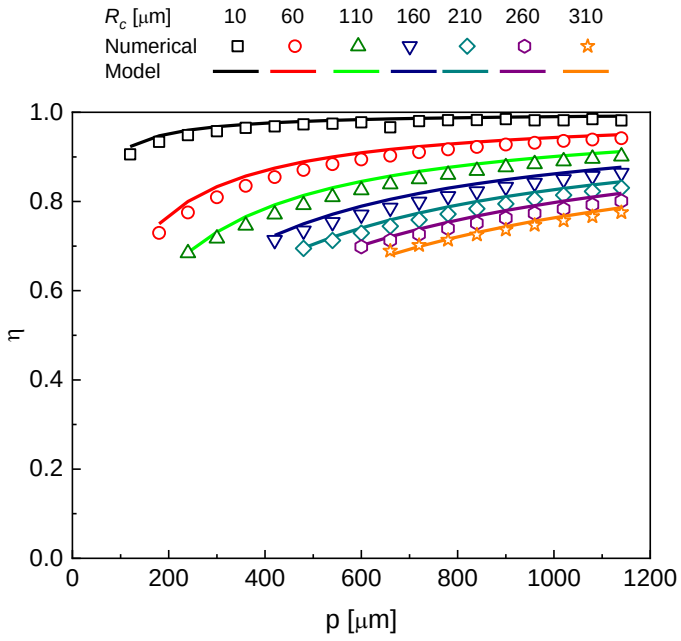

(a)

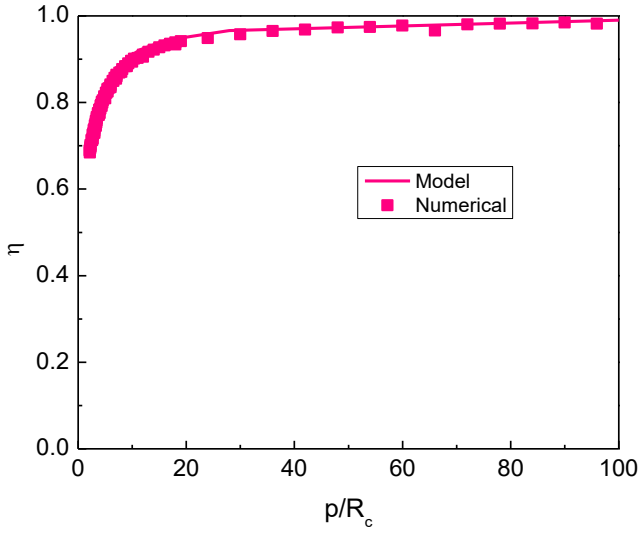

(b)

Figure 3.3. (a) Condensation rate correction factor η for a pair of equally sized droplets having varying contact radii R_c as function of droplet pitch p (correction factor compared to the case of an isolated droplet). The predictions using the point sink method are shown as solid lines while results of the numerical simulations are shown as symbols. (b) Correction factor for all of the cases in (a) presented as a function of the ratio between the droplet pitch and contact radii, p/R_c.

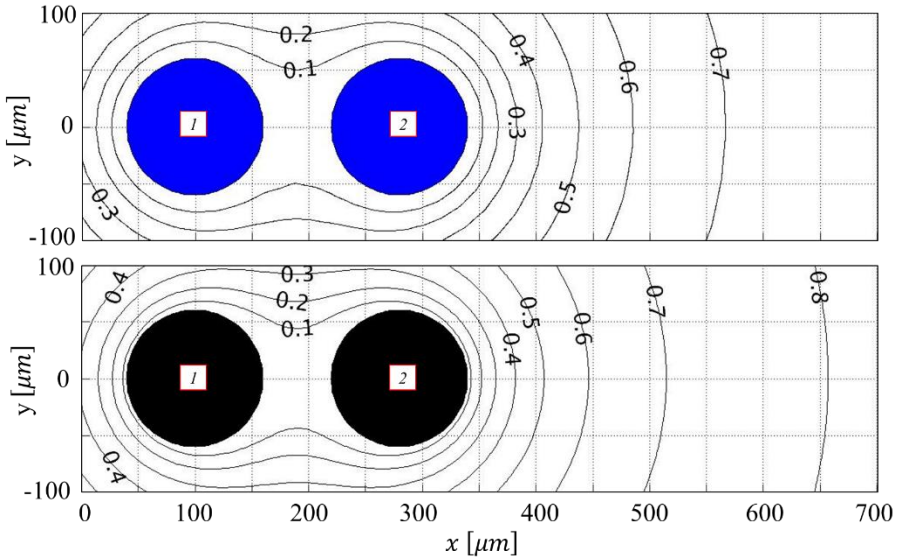

Figure 3.4. Normalized vapor concentration field $\upsilon(\vec{r})$ at the substrate plane in a region surrounding condensing droplets having the same size $R_c = R_{c1} = R_{c2} = 60$ μm spaced apart at a pitch $p = 120$ μm. Results are shown for the numerical simulations (top panel) and for point sink method based prediction (bottom panel).

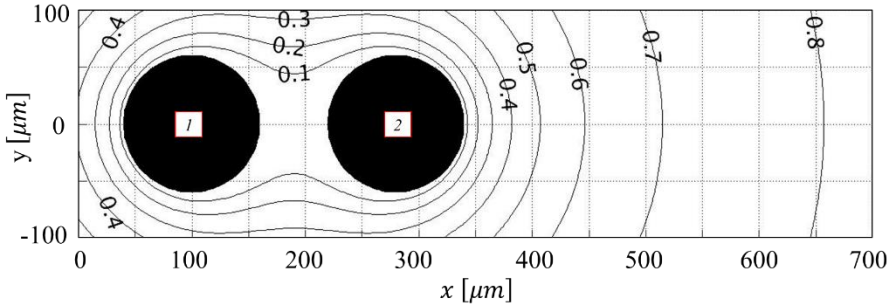

(a)

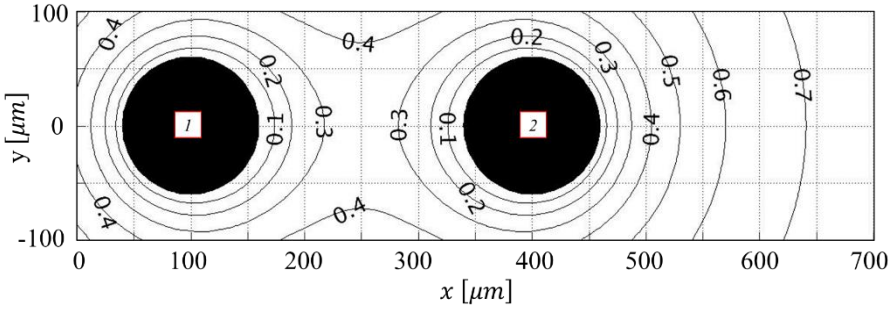

(b)

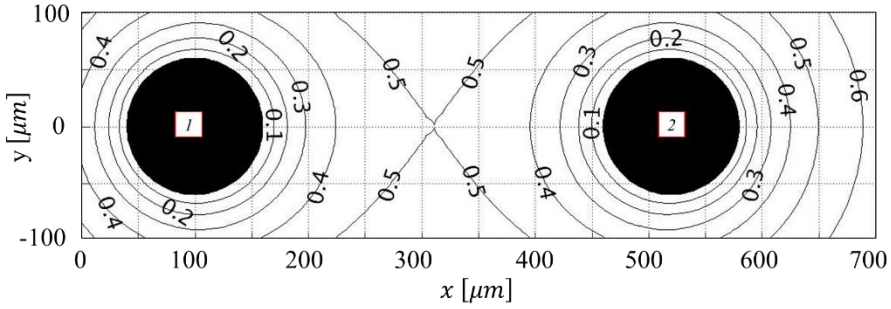

(c)

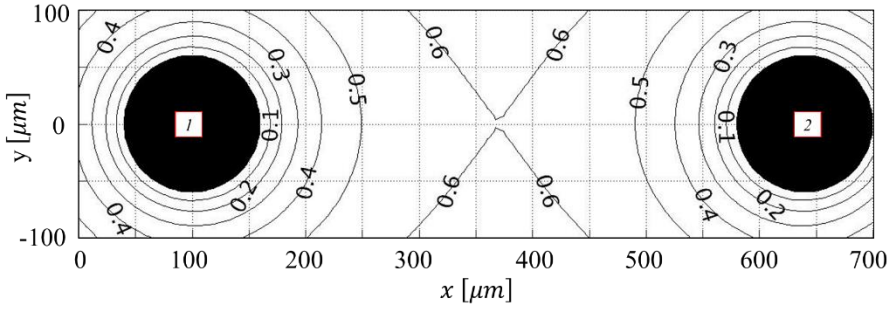

(d)

Figure 3.5. Normalized vapor concentration field $\upsilon(\vec{r})$ at the substrate plane predicted using the point sink superposition method in a region surrounding two condensing droplets having the same size $R_c = R_{c1} = R_{c2}$ = 60 μm and spaced apart at four pitches of (a) 180 μm, (b) 300 μm, (c) 420 μm, and (d) 540 μm.

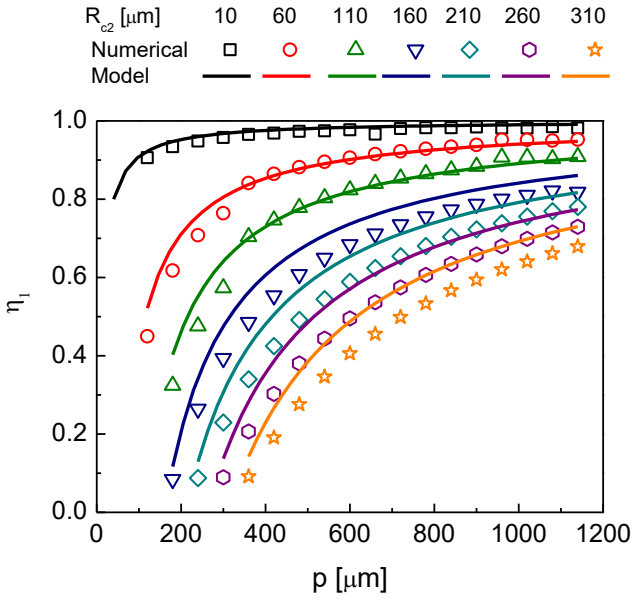

(a)

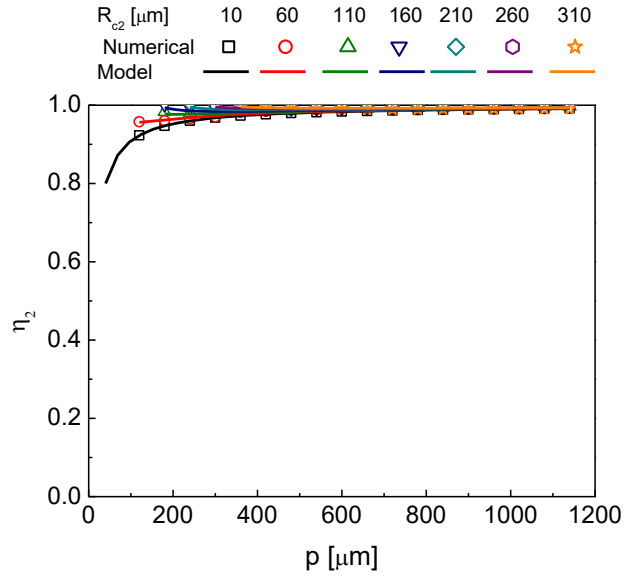

(b)

Figure 3.6. Condensation rate correction factors (a) η_1 for a small droplet, R_{c1} = 10 μm, and (b) η_2 for the relatively larger neighbor droplet, 10 μm < R_{c2} < 310 μm, as function of the pitch between the two droplets. The predictions using the point sink method are shown as solid lines while results of the numerical simulations are shown as symbols.

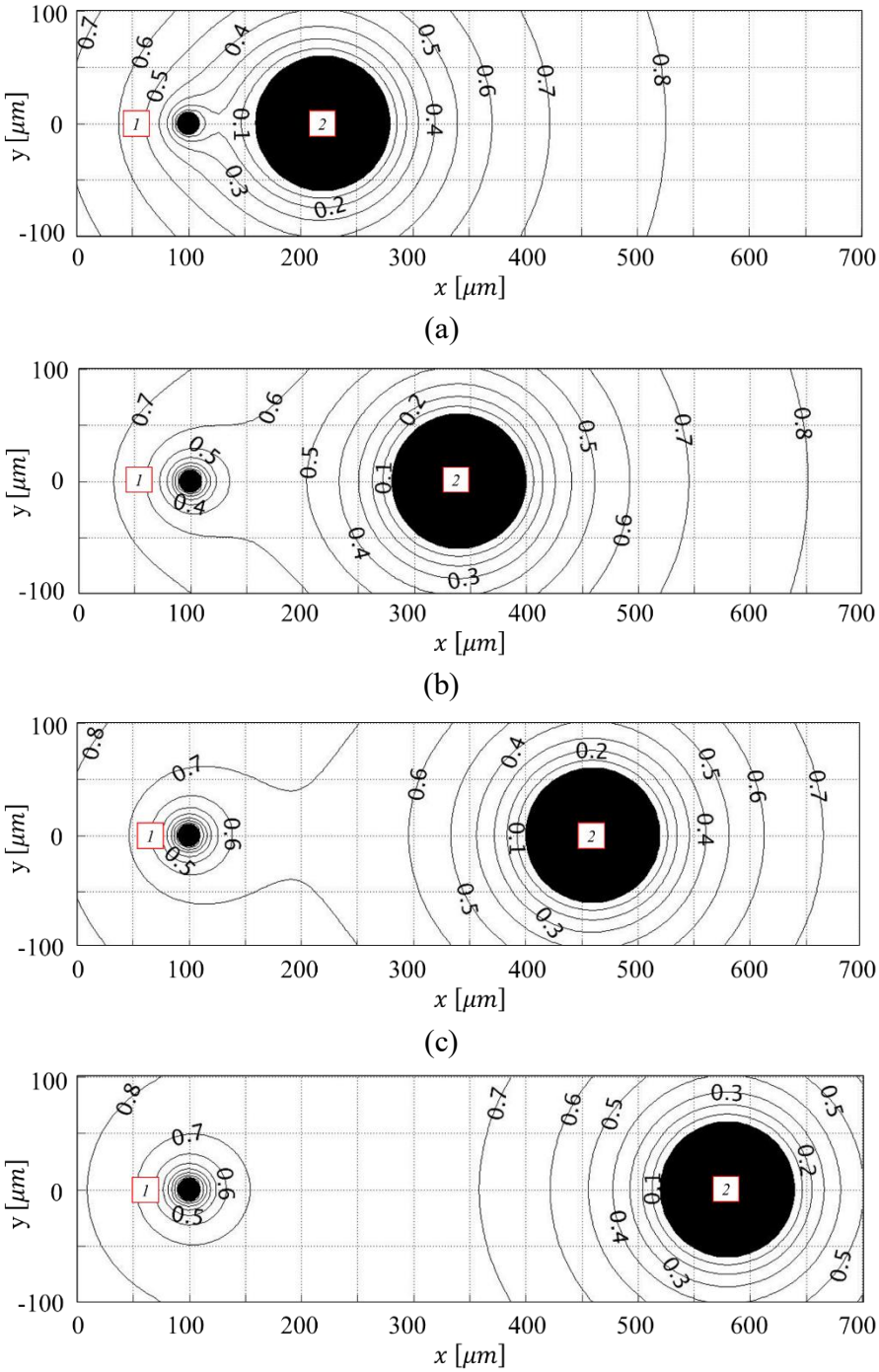

Figure 3.7. Normalized vapor concentration field $\upsilon(\vec{r})$ at the substrate plane predicted using the point sink superposition method for a small condensing droplet R_{c1} = 10 μm nearby a larger condensing droplet R_{c2} = 60 μm at four pitches of (a) 120 μm, (b) 240 μm, (c) 360 μm, and (d) 480 μm.

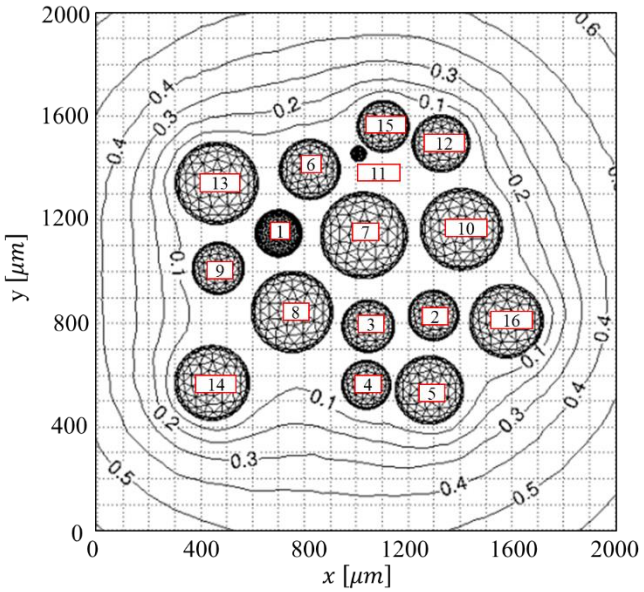

(a)

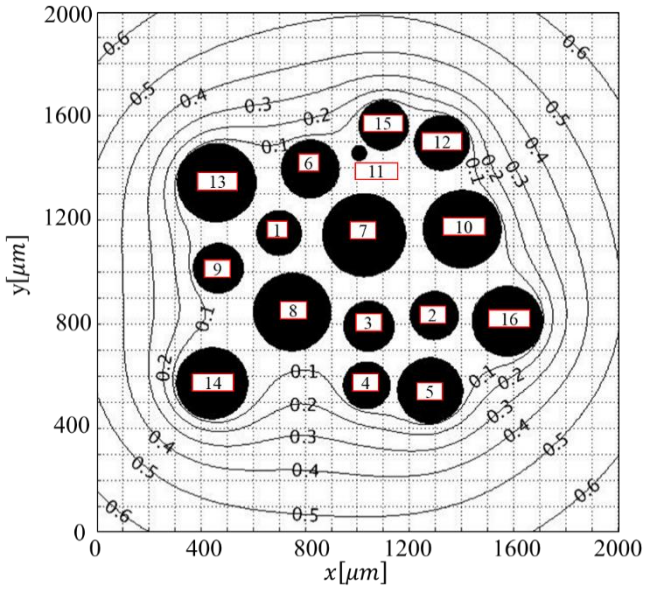

(b)

Figure 3.8. Normalized vapor concentration field $\upsilon(\vec{r})$ at the substrate plane for a system of 16 condensing droplets obtained using (a) the numerical solution of the vapor diffusion equation and (b) the point sink superposition method modeling approach.

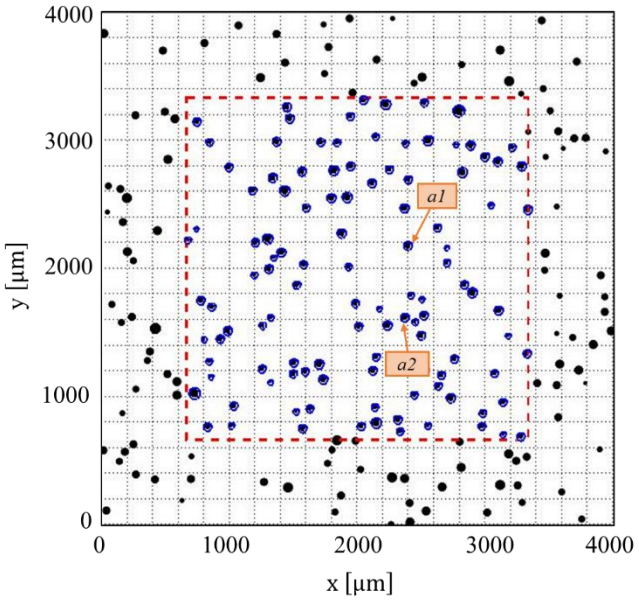

(a)

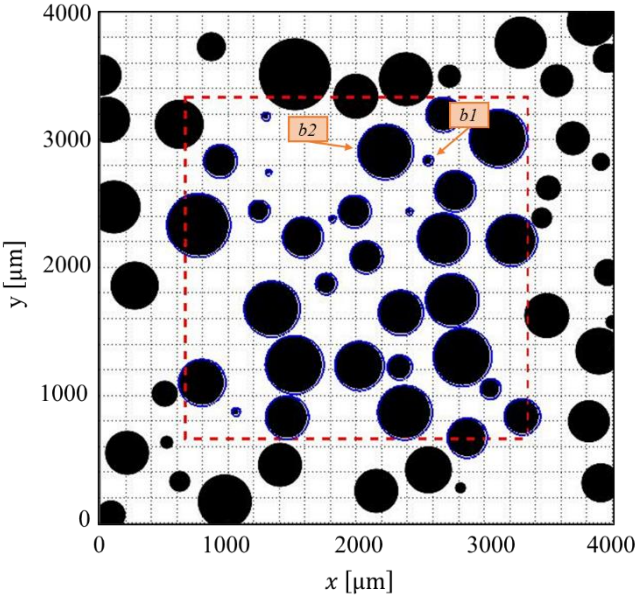

(b)

Figure 3.9. Systems of randomly generated droplets having (a) 172 droplets with an average radius of 30.1 µm and standard deviation of 5.0 µm and (b) 66 droplets with average radius of 143.3 µm and standard deviation of 69.9 µm. Analysis of the condensation behavior is restricted to within the dashed squares containing a subset of (a) 112 and (b) 32 droplets

4. PREDICTING THE GROWTH OF MANY DROPLETS DURING DIFFUSION-DRIVEN DROPWISE CONDENSATION EXPERIMENTS USING THE POINT SINK SUPERPOSITION METHOD

This chapter presents direct comparisons of droplet condensation rates predicted by the point sink superposition method against dropwise condensation experiments from humid air. Droplet growth is tracked during the condensation process in order to measure the condensation rate of each droplet, which is then compared to the instantaneous condensation rates predicted by the point sink superposition method. At the experimental conditions, model predictions of the instantaneous and temporal droplet condensation rates are investigated as function of the number of interacting droplets taken into account in the system. These droplet growth characteristics are discussed in terms of the interactions between each droplet and all of its neighbors during different stages of droplet growth. By incorporating the interaction of all the droplets, the point sink superposition method can be used as a tool to accurately predict droplet growth during dropwise condensation from humid air. The material presented in this chapter was published in April 2019 in the *International Journal of Heat and Mass Transfer* [90]

4.1 Experimental description

4.1.1 Substrate Preparation

Smooth 20 × 20 mm^2 silicon substrates were silanized to render them hydrophobic. The silicon substrates were first cleaned with piranha solution (3:1 H_2SO_4:H_2O_2) for 10 min, rinsed with DI water, and blown dry with N_2. The samples were then spin-coated with a 1:1000 v/v solution of trichloro(1H,1H,2H,2H-perfluorooctyl) silane (Sigma-Aldrich) in hexane (Sigma-Aldrich) at 2500 rpm and baked on a hot plate at 140 ℃ for 1 h to evaporate the solvent. The sample surface had a measured average roughness of 0.001 μm (NewView 6000, Zygo) and a contact angle with a 5 μl droplet water of 119.5 deg, as measured from side-view images using a goniometer (ramé-hart, 290-F1).

4.1.2 Experimental Setup

Condensation experiments were carried out inside a custom-made environmental chamber equipped with air conditioning and cooling systems. A description of the condensation test facility

is presented here, which is a modified version of the facility previously introduced in detail in Ref [10]. A schematic diagram showing the flow conditioning systems and a picture of the test section are provided in Figure 4.1. The humidity conditioning system mixes dry and humid air adiabatically to achieve the relative humidity desired in the downstream test section. Two mass flow controllers (FMQ 5400, 0-2 SLM, Omega) regulate the amount of dry gas that passes through the humidifier or bypasses to the adiabatic mixer, before the gas mixture enters the test section. A hygrometer (HX93V2-RP1, Omega) inside the test section measures the relative humidity and provides feedback to a PID control loop that actuates the two mass flow controllers. All signals are acquired using a data acquisition system (PCI-6120, National Instruments). The relative humidity can be controlled to set points between 20% and 75% with a measurement uncertainty of ± 2.5%. The temperature inside the test section is monitored by a built-in temperature sensor in the hygrometer with a measurement uncertainty of ± 0.6 °C.

The temperature of the substrate is maintained constant through the experiments by using the cooling system attached to the test section as depicted in Figure 4.1. A chiller (ThermoFlex, 900 W, Thermo Scientific) circulates cooled water through a cooling plate (CP12, Lytron) that mounts flush with bottom of the test section and maintained at a constant temperature. A thermoelectric cooler (ZT8, Laird Technologies) attached to the top of the cold plate is used for fine-tuning of the sample temperature.

The stack of components inside the test section used to thermally bridge the sample to the cooling system was modified as compared to Ref.. [10]. An aluminum block, placed between the thermoelectric device and sample substrate, was decreased in size ($20 \times 20 \times 6.35$ mm^3) to reduce thermal inertia of the system and improve the response time of the sample temperature control system. The temperature of the sample was sensed by a 2 wire Pt1000 RTD (PRTF-10-2-100-M30-450-E-GG, Omega) that fits in a hole located at 2.5 mm from the top surface of the aluminum sample holder. The temperature signal closes a PID control loop programmed in a temperature controller (MTTC-1410, Laird Technologies). The substrate is attached to the sample holder with carbon conductive double-sided tape (PELCO Image Tabs). The cooling system is capable of maintaining a constant set-point temperature to within ± 1.0 °C and with a measurement uncertainty of ± 0.1 °C as sensed by the RTD.

4.1.3 Experimental Procedure and Visualization

The substrate is attached to the sample holder, which is then attached to the thermoelectric cooler inside the test section. The test section is sealed and purged with dry air for ~20 min until the relative humidity reaches 20%. At the same time, the cold plate is used to cool down the entire test section until the temperature of the sample and the gas mixture inside the chamber stabilize at ~20 °C.

Once the gas inside the chamber has reached constant temperature and relative humidity, the gas mixture flow controller is turned on. Once the relative humidity inside the chamber reaches the set point, the thermoelectric cooler controller is turned on and set to the desired sample temperature. After ~1 min, the temperature of the sample reaches a constant value within ± 2% of the set-point temperature. The relative humidity controller compensates for drying of the air inside the chamber caused by the rapid sample cooling. Within ~2 min after the thermoelectric has been turned on, the relative humidity inside the chamber reaches a constant value with ± 5% error relative to the set-point value.

Each condensation experiment is carried out at a specified relative humidity and substrate temperature. This chapter presents condensation experiments performed at a constant substrate temperature of T_{sub} = 10.0 °C, constant air temperature of T_{∞} = 20.5 °C, and three different relative humidity values of RH = 70, 60, and 50%.

Video of the condensation process is recorded viewing normal to the sample using a camera (EO-5023M, Edmund Optics) at 150× magnification using a long-focal-distance zoom lens (VH-Z50L, Keyence) with in-line illumination provided by a 300 W Xe arc lamp (Titan 300, Sunoptic Technologies). The video recording was synchronized with the data acquisition system, such that each image corresponds to a known set of experimental conditions. Once the sample temperature and the chamber relative humidity are constant, the camera starts recording, corresponding with the initial time t = 0 min.

4.1.4 Image Post-Processing

An automated video post-processing script developed in MATLAB is used to obtain information about the spatial distribution and temporal evolution of the droplets during the condensation experiments. The algorithm extracts a sequence of snapshot images from the video

recordings and, within each image, detects each droplet by recognizing their boundaries as circles with centers coinciding with the centers of the droplets. Figure 4.2 (a) and (b) show snapshot images taken at 9 and 16 min during experiment at RH = 70%. The edges of the droplets are depicted as blue circles, while the dashed red lines represent the Delaunay triangulation from the droplet centers.

The spatial resolution was calibrated by measuring circular patterns on a calibration target (100 × 100 mm2, 1.0 mm spacing, Glass Distortion Target, Edmund Optics) using the detection algorithm described above, which is capable of detecting subpixel variations in circular patterns. At 150× magnification, the calibrated spatial resolution is 0.88 ± 0.0015 μm/pixel. This apparently high sensitivity comes from the ability of the circle detection algorithm capable of detecting subpixel variations in circular patterns. The ~1.7 × 1.7 mm^2 field of view surveyed during the experiments is located near the center of the 20 × 20 mm^2 substrate. Droplets with contact radii from 12 μm to 100 μm were detected. The droplets are assumed to be spherical caps with a constant contact angle equal to 119.5 degrees.

The algorithm is used to track individual droplets, as is demonstrated for droplet $a1$, which appears in both sequential frames of. The algorithm is also used to track groups of droplets among which coalescence events can be identified as time progresses. For example, the nearest neighbors of droplet $a1$, droplets $b1$ through $b7$ in (a), correspond to droplets $c1$ through $c5$ in (b), where droplets $b1$ and $b2$ merged to form droplet $c2$.

The condensation rate of each droplet is calculated as the ratio between the change in mass over the time elapsed between successive images, using a five-point moving average to filter spurious noise. Information regarding coalescence events is used to note changes in condensation rate due to coalescence. Changes in the condensation rates of individual droplets between ~10^{-15} to ~10^{-13} kg/s can be resolved by the algorithm, with uncertainties proportional to the measurement uncertainty in droplet size.

Because the area of the substrate that can be surveyed at high magnification is limited to a region that is only ~8.5% of the total substrate area, an algorithm was developed to generate artificial droplets outside the interrogation window. The algorithm creates droplets to mimic the size distribution and density of the droplets inside the interrogation window. The purpose and use of this algorithm are further described in the results (Sections 4.2.1.1 and 4.2.1.2).

4.2 Results

4.2.1 Comparison of the Point Sink Superposition Method (PSSM) with Experiments

This section compares the instantaneous condensation rates of individual and groups of droplets measured during condensation experiments against predictions of the point sink superposition method (PSSM). The case considered in this section is for droplets growing during at T_{sub} = 10 °C, RH = 70%, and T_{∞} = 20.5 °C. At these conditions, the water vapor concentration at the surface of the droplet is c_s = 0.0095 kg/m^3 and the vapor concentration in the far field is c_{∞} = 0.0126 kg/m^3. The PSSM calculation considers the size and location of the droplets inside the interrogation window as described in Section 4.1.4. Additional comparisons for experiments at RH = 50% and RH = 60% are provided in Appendix A.

4.2.1.1 Condensation Rate of a Single Droplet

A top-down view of the model domain employed to predict the condensation rate of a single droplet is depicted in **Error! Reference source not found.** (a). Near the center of the image, the droplets inside the field of view during the experiment at t = 31 min are filled red, while the droplets outside the camera field of view are filled white. Among the droplets inside the field of view, the condensation rate is predicted with the PSSM for the droplet of interest (filled blue). The instantaneous condensation rate predicted for a droplet highly depends on the number of neighboring droplets considered in the calculation (N_{PSSM}), due to the competition for surrounding vapor. The calculated condensation rate of the droplet of interest ($\dot{m}_{PSSM}$) is plotted against N_{PSSM} in **Error! Reference source not found.** (b), with N_{PSSM} sorted in ascending order based on the distance from the droplet of interest. By increasing N_{PSSM} in each calculation, the predicted $\dot{m}_{PSSM}$ converges to the measured condensation rate for the droplets of interest $\dot{m}_{exp} = 1.77 \times 10^{-12} \pm 6.14 \times 10^{-13}$ kg/s (represented by the horizontal line in **Error! Reference source not found.** (b). This is quantified via the decrease in percentage error of $\dot{m}_{PSSM}$ relative to $\dot{m}_{exp}$ with increasing N_{PSSM} and, similarly the decrease in the residual of $\dot{m}_{PSSM}$ between increments of N_{PSSM} , as shown in **Error! Reference source not found.** (c).

When only the group of seven nearest neighbors to the droplet of interest is considered, connected by a green line in **Error! Reference source not found.** (a), the prediction is

approximately eight times larger than the measured condensation rate. Vapor-diffusion-based models that only account for the interaction with nearest neighboring droplets would grossly overestimate the condensation rate of the droplet. As more droplets inside the field of view are added to the calculation, the relative error between $\dot{m}_{PSSM}$ and $\dot{m}_{exp}$ drops sharply. However, after including all the red-filled droplets in the field of view (N_{PSSM} = 61), $\dot{m}_{PSSM}$ is still a couple of times greater than $\dot{m}_{exp}$, which indicates that droplets located even outside the field of view have a significant effect on the vapor distribution surrounding the droplet of interest. Since the droplets located outside the field of view can not be surveyed, their effects are represented by creating artificial droplets in the domain, surrounding the field of view, using the algorithm described in Section 4.1.4. As more of these additional droplets are included in the calculation, $\dot{m}_{PSSM}$ continues to approach toward $\dot{m}_{exp}$. When N_{PSSM} = 564 (purple vertical lines in **Error! Reference source not found.** (b) and (c)), the residual of the condensation rate is three orders of magnitude smaller than $\dot{m}_{exp}$ and of the same order of magnitude as the minimum condensation rate that can be detected by the experimental apparatus (~10^{-15}); at this point, the relative error in the prediction is 15.33%. At N_{PSSM} = 753, the relative error between $\dot{m}_{PSSM}$ and $\dot{m}_{exp}$ is 0.06 %.

From these results, we observed that a large number of droplets must be considered in a system to accurately predict the condensation rate. If a sufficient number of droplets are considered, the PSSM model can be used to accurately predict the condensation rate of a single droplet within the system. In general, the number of droplets required is expected to depend on the size and spatial distribution of its neighboring droplets.

4.2.1.2 Condensation Rate of a Group of Droplets

In this section, the condensation rate prediction is extended to a group of 30 droplets within the same domain as was considered in Section 4.2.1.1. A top-down view of the domain shown in **Error! Reference source not found.** (a) is reproduced in Figure 4.4 (a). All droplets in the group of interest are filled blue inside the boundary defined by the yellow line; droplets in the experimental field of view are filled red. Each droplet of interest has been assigned an identification number shown in the zoomed-in view of the domain in Figure 4.6. Figure 4.4 (b) shows the predicted total condensation rate of the group of droplets ($\dot{M}$) versus the number of

droplets included in the prediction (N_{PSSM}), where the blue horizontal line is the total condensation rate measured during experiments $\dot{M}_{\exp} = 3.04 \times 10^{-11} \pm 1.61 \times 10^{-12}$ kg/s. The condensation rate for each droplet within the group is shown in Figure 4.5 (b).

When the prediction includes all droplets in the field of view ($N_{PSSM} = 61$), $\dot{M}_{PSSM}$ is about three times larger than $\dot{M}_{\exp}$, and the condensation rate of each individual droplet is also overpredicted, as shown in Figure 4.5 (b). As more droplets are included in the model, $\dot{M}_{PSSM}$ converges to the measured $\dot{M}_{\exp}$, as indicated in Figure 4.4 (b). The residual of the calculated $\dot{M}_{PSSM}$ and the error relative to $\dot{M}_{\exp}$ are plotted as a function of N_{PSSM} Figure 4.4 (c); both quantities decrease as N_{PSSM} increases. When $N_{PSSM} = 526$ the difference between $\dot{M}_{PSSM}$ and $\dot{M}_{\exp}$ reaches a minimum, and $\dot{m}_{PSSM}$ for each droplet approximates its corresponding $\dot{m}_{exp}$ value as shown in Figure 4.4 (b) and Figure 4.5 (b), respectively. In average, the relative error for individual droplets was 2.9% and standard deviation of 42.1%. When $N_{PSSM} = 569$, the residual of $\dot{M}_{PSSM}$ is three orders of magnitude smaller than $\dot{M}_{\exp}$ and the model slightly underpredicts $\dot{M}_{\exp}$ with an error of -1.24 %.

The number of droplets that must be included in the domain to accurately predict the total condensation rate of groups of droplets is different at differing times of the condensation process, as the size and distribution characteristics of the droplets changes. Table 4.1 summarizes the number of droplets N_{PSSM} required in the system to minimize the error in the condensation rate between the model and measurements, as well as the max cord length of the region that encloses these droplets (κ). The N_{PSSM} required to minimize the relative error decreases as the condensation process progresses , but κ does not vary significantly, with an average equal to 2531 $\pm$ 7.8 μm. During regime (i), the number of droplets per-unit-area is large, as droplet coalesce and grow (during regime (ii)) the number of droplets decreases. As a result, for a set region of the substrate, the number of droplets per unit area will reduce with time, The value of κ provides a case-specific criterion for assessing the number of droplets that must be included in a system to accurate predict the condensation rate.

4.2.1.3 Temporal Evolution of the Condensation Rate of Single Droplets

This section focuses on predicting the temporal evolution of the condensation rate of individual droplets observed during the condensation experiments at T_{sub} = 10 °C, RH = 70%, and T_{∞} = 20.5 °C. Figure 4.6 (a) shows two typical droplets tagged as d and e in a sequence of images at t = 14.5 and 17. 0 min . The measured and predicted time-varying condensation rates of droplets d and e are plotted in Figure 4.6 (b). Periods of continuous growth are interrupted by sudden jumps in the condensation rate that result from the coalescence events depicted in Figure 4.6 (a). The number of droplets used in the PSSM model predictions correspond to all the droplets enclosed in the region defined by κ = 2530 μm.

Overall, the instantaneous condensation rates predicted at each instant of the growth closely match the condensation rates measured experimentally for droplets d and e. The trends in the condensation rates of the droplet do not correspond with the ones expected from the isolated growth model ($\dot{m} \sim t^{1/2}$) and film-like model ($\dot{m} = constant$). Before the first coalesce event, the condensation rate of droplets d and e follow a power law $\dot{m} \sim t^{\beta}$ where β = -0.11 for droplet d and β = 0.12 for droplet e. Within an image, each droplet has distinct growth characteristics that depend on its size and its interactions with their respective neighbors.

4.2.2 Comparison with Isolated Droplet and Film-Like Models for Condensation

This section aim is to compare the experimental condensation rates of individual droplets and group of droplets presented in Sections 4.2.1.1 and 4.2.1.2 against the isolated growth model and the film-like model. Introduction to section. The isolated growth model given in equation (3.6) neglects the interaction between neighboring droplets. It assumes that droplet grow during dropwise condensation in a pattern such that the distance between droplet is so larger that the vapor distributions surrounding each droplet have no effect on each other. In comparison with the condensation rate measured for the single droplet of interest considered in Section 4.2.1.1, the condensation rate predicted by the isolated model from equation (3.6) ($\dot{m}_{iso}$ = 6.46 × 10^{-11} kg/s) is over an order of magnitude larger. Similarly, the total condensation rate for the group of droplets considered in Section 4.2.1.2. predicted by the isolated model ($\dot{M}_{iso}$ = 6.42 × 10^{-10} kg/s), is two orders of magnitude larger the measured condensation rate. The isolated model for dropwise condensation significantly overpredicts experimental condensation rates. When droplets become

densely packed on a surface, it has been commonly assumed [12,13,82,91] that the water vapor distributions around each droplet overlap such that they grow as a film of equivalent volume spread over the surface. The film-like growth model treats the vapor concentration profile as varying linearly in the direction normal to the substrate. Medici *et al.* [12] determined an explicit expression for the temporal evolution of the thickness of a film from which the condensation rate of each droplet is a constant given by:

$$\dot{M}_{film} = \frac{D\left(c_\infty - c_s\right)}{\zeta} S\,, \tag{4.1}$$

where S is the area of the condensation substrate, and ζ is the thickness of the concentration boundary layer, which corresponds to the extent of the region where the transport by diffusion dominates over the transport due to convection. A primary challenge in applying the film-like model comes from accurately determining the value of ζ. Approximate estimates of ζ are often obtained from a scaling analysis for natural convection above a horizontal cooled plate. By assuming that the transport by natural convection is negligible ($Pe < 1$) in the scaling analysis, Medici *et al.*[12] derived an expression for ζ in terms of experimental conditions:

$$\zeta \sim \left[\frac{D\delta^{3/2}}{4\left(\beta g \Delta T\right)^{1/2}}\right]^{1/3} \tag{4.2}$$

where $\delta \sim LGr^{-1/5}$ is the thickness of hydrodynamic boundary layer caused by buoyancy effects, with L being the characteristic length of the sample, $\Delta T = T_\infty - T_{sub}$, and $\beta = 2/\left(T_\infty + T_{sub}\right)$ is the volumetric thermal expansion coefficient for air.

For the experimental conditions T_{sub} = 10 °C, RH = 70%, and T_∞ = 20.5 °C , the concentration boundary layer is estimated to $\zeta \approx 1.0$ mm. To compare the film-like growth model to the results presented in Section 4.2.1.2, the substrate area S is assumed to be equal to the area of the region defined by connecting the centers of the droplets of interest (yellow line in Figure 4.4 (b)). From equation (4.1) the condensation rate predicted by the film-like growth model is

equal to $\dot{M}_{film}$ = 5.55 × 10^{-11} kg/s, an overprediction of the measured total condensation rate for the group of droplets by 82.8 %.

4.2.3 Intensity of Droplet-to-Droplet Interaction

Equation (3.15) can be rewritten in matrixial form as:

$$\dot{m}_{sys,i} = \dot{m}_{iso,i} B_{ij}^{-1} \tag{4.3}$$

where B_{ij} is an N by N matrix with diagonal elements ($i = j$) equal to unity and off-diagonal elements ($i \neq j$) equal to:

$$B_{ij} = \left(\frac{R_{cj}}{\left| \vec{r}_i - \vec{r}_j \right|} \right) \tag{4.4}$$

For an arbitrary droplet i, the condensation correction factor η computed from equation

$$\eta_i = B_{i,j=i}^{-1} + \sum_{i,j \neq i}^{N} B_{ij}^{-1} \tag{4.5}$$

where $B_{i,j=i}^{-1}$ is greater than unity and $\sum_{i,j \neq i}^{N} B_{ij}^{-1}$ is negative and represents the contributions caused by neighboring droplets. In relation to all the droplets in the system, any given droplet j reduces the condensation rate of the droplet of interest with an intensity given by:

$$\Psi_{ij} = \frac{B_{i,j \neq i}^{-1}}{\sum_{i,j \neq i}^{N} B_{ij}^{-1}} \tag{4.6}$$

where Ψ_{ij} will be equal to unity when the droplet of interest i interacts with a neighboring droplet j while any other interaction of droplet i is negligible, Ψ_{ij} will be equal to zero when the interaction of droplet i with droplet j is negligible.

Figure 4.7 (a) and (b) depict the absolute value of the intensity of the interaction between a central droplet of interest and all other droplets in the domain at times of 2.0 min and 31.0 min, respectively. The conditions used in the calculation were as the ones used in Section 4.2.1.3 (T_{sub} = 10 °C, RH = 70%, and T_{∞} = 20.5 °C). Similarly, the number of droplets included in this calculation corresponded with the droplets enclosed by max cord length of the region κ = 2531 μm. The color of each droplet represents the intensity of the interaction. The intensity of the interaction is larger for the nearest neighboring droplets and attenuates with distance from the droplet of interest. The red dashed line in the figure encloses 90% of the total interaction intensity between the droplet of interest and all droplets in the domain. At earlier stages of the growth (within regime (*i*)), in Figure 4.7 (a), the sum of the interaction intensities of the nearest droplets is only 42.2 % of the total interaction intensity, while the region that contains 90% of the total interaction intensity extends far beyond the nearest droplets, ~1000 μm from the droplet of interest. At a later time (within regime (*ii*)) in Figure 4.7 (b), the sum of the interaction intensities of the nearest droplets increases to 87.2% of the sum of the interaction with all neighboring droplets. In this case, the distance at which the interaction intensity sums to 90% of the total is a decreased distance comparable to the separation the nearest neighbors, ~300 μm. Note that even though a large proportion of the total interaction intensity occurs between a droplet and its nearest neighbors, this conclusion does not mean that it is accurate to calculate the magnitude of condensation rate of a droplet by considering only its nearest neighbors (refer to Section 4.2.1.1). Rather, the strong interactions with the nearest neighbors governs the condensation rate relative to each other, but the interactions with all the other droplets determines the specific magnitude of the condensation rater. Models that consider only the interactions with nearest droplets offer a limited description of droplet growth that can predict trends, but not quantitative condensation rates.

4.2.4 Effects of Droplet Size and Spatial Distribution on the Condensation Rate

This section focuses on using the predictions of the point sink superposition method to gain insight into the effects of droplet size and spatial distribution on the condensation rate of each droplet within the system. Figure 4.8 shows individual droplet condensation rates versus their corresponding contact radius for a set of images taken at t = 2.0, 6.0, 21.0 and 31.0 min. At any given time, the condensation rate is proportional to droplet size. As time proceeds, the distribution of droplet sizes broadens and the average droplet size increases; as a result, the average

condensation rate and the range of condensation rates observed in each image increases with time. However, across different times, larger droplets do not always necessarily grow at larger rates; droplets having similar sizes but belonging to images taken at different times can have significantly different condensation rates. For example, droplets ranging from ~40 μm to ~45 μm in contact radius at t = 6.0 min grow at higher rates than the same size droplets at 21.0 min. This behavior could not be captured by dropwise condensation models that calculate the total condensation rate by summing the condensation rates of individual droplets as they were isolated from one other.

T These differences in the condensation rates of droplets can be explained in terms of the spatial distribution of droplets in their surroundings and their size relative to the size of their neighbors. Voronoi polygon constructions based on the droplet center positions have been used extensively to characterize condensation rates and relative distance from neighboring droplets. Prior studies [12,33,35,91–93] have suggested that droplets with larger Voronoi polygons grow at faster rates; the area of the Voronoi polygon is the sum of the footprint area of the droplet located at the center of the polygon and the bare area surrounding the droplet. Large droplets that are surrounded by large bare areas are able to capture relatively more of the water vapor that is diffusing from the ambient toward the substrate and laterally in between neighboring droplets. **Error! Reference source not found.** (a) and (b) shows the predicted condensation rates and Voronoi constructions of droplets from snapshot images taken at t = 2 min and t = 31 min, respectively. The color of each droplet indicates its condensation rate. The red lines define the boundary of each Voronoi polygon, and the color inside each polygon represents the magnitude of the polygon area. At t = 2 min, the droplets that grow at faster rates have polygons with larger areas even though they have similar size, such as comparing droplet f to droplet g in Figure 4.8 (b).). At later times, droplets that have polygons with larger areas do not necessarily grow faster. We have previously shown that the condensation rate of pairs of droplets predicted by the PSSM is sensitive to the ratio of between the droplet sizes. Large droplets can limit the vapor diffusion of small droplets in their surroundings For example, droplet h in **Error! Reference source not found.** (b) has a larger Voronoi polygon area than its neighbor droplet l, but grows at a smaller rate, because droplet l has a larger size and it is surrounded by smaller neighbors than droplet h. Thus, the size of a given droplet in relation to the size of its neighbors can significantly influence the condensation rate.

Figure 4.8 (c) shows individual droplet condensation rates versus their corresponding ratio between the contact radius of each droplet to the average contact radius of its nearest neighbors

$R_{ci}/\langle R_{cj} \rangle$ for a set of images taken at t = 2.0, 6.0, 21.0 and 31.0 min. The condensation rate of individual droplets increases with the ratio between their contact radii and the average contact radius of their nearest neighbors. At the earliest stages of the growth, when the droplets have similar sizes as shown in Figure 4.8 (a) the condensation rate is relatively insensitive to the droplet relative size $R_{ci}/\langle R_{cj} \rangle$ and the condensation rate mostly depends on the spatial distribution of the droplets. At later times, similar variations in droplet relative size lead to greater changes in the condensation rate.

4.3 Conclusions

The point source superposition method is used to predict experimental condensation rates of individual droplets, within a system of many droplets on a substrate, formed during vapor-diffusion-driven dropwise condensation from humid air. The point sink superposition method accurately predicts the experimental growth rates of individual droplets, and the total condensation rate of groups of interacting droplets, by superposing the vapor distributions of all droplets on the substrate. Assuming that droplets grow completely isolated from one another severely overpredicts the measured condensation rates. It is shown through use of the point sink superposition method that a large number of interacting droplets, over a length scale of the substrate much larger than the separation distance between droplets, must be considered to accurately predict the experiments. Even though the interaction between nearest neighboring droplets is the strongest, only including the such neighboring droplets in the close vicinity still severely overpredicts condensation rate of an individual within the system. This highlights a limitation of modeling approaches that describe the condensation rate based on the interactions between nearest neighbors. The point superposition method, which captures the interactions between all droplets within the system and accounts for their locations and sizes, is used as a tool study the interactions between condensing droplets in the experiments as a function of droplet size and pitch. Relative droplet size effects on condensation rates are more prominent at later stages of the growth, when the size distribution of droplet is broader.

Table 4.1. Max cord length of the region (κ) that encloses the given number of droplets (N_{PSSM}) required to predict the measured condensation rate with minimum relative error (for a group of 30 droplets at different times during experiment at T_{sub} = 10 °C, RH = 70%, and T_{∞} = 20.5 °C).

Time [min]	N_{PSSM}	κ [μm]
11	982	2330
16	820	2340
21	811	2790
26	586	2600
31	526	2620

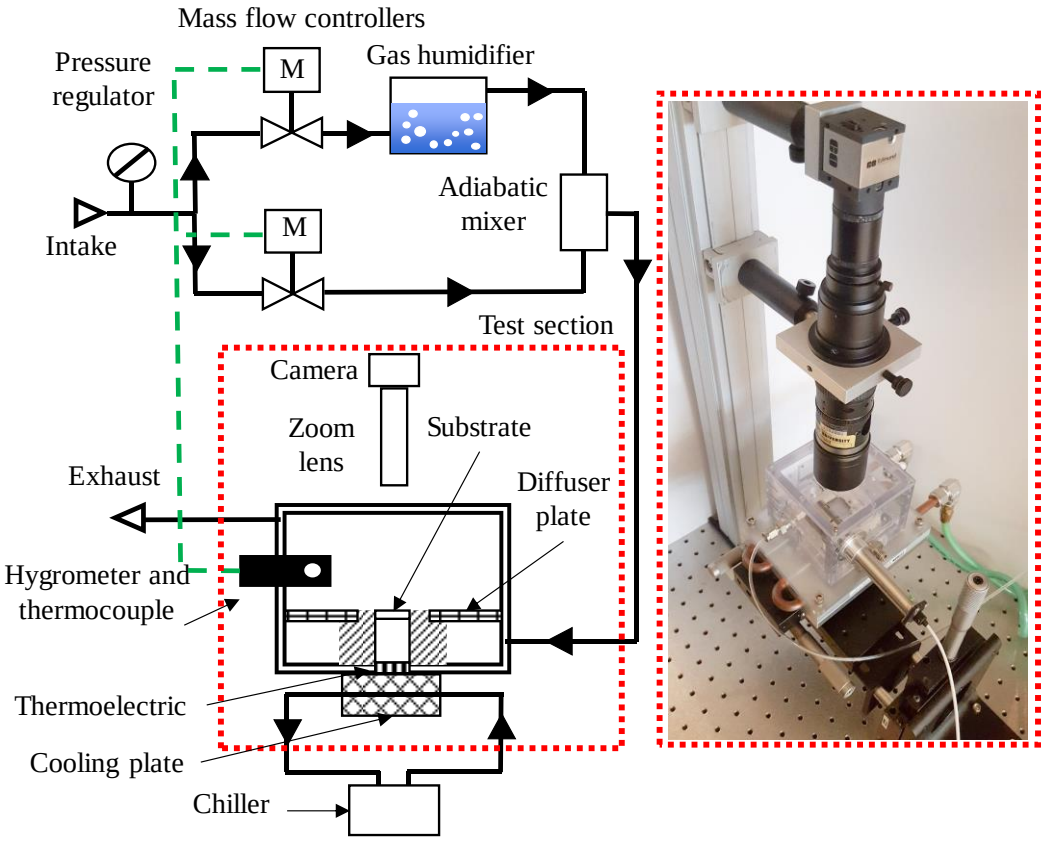

Figure 4.1. Schematic diagram depicting the condensation testing faculty and a photograph of the test section

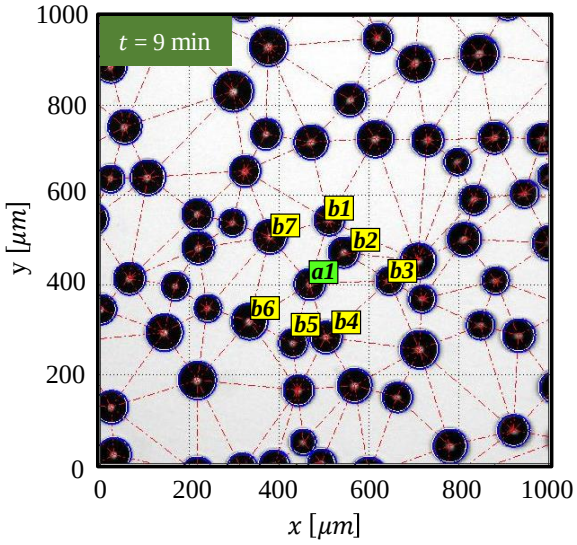

(a)

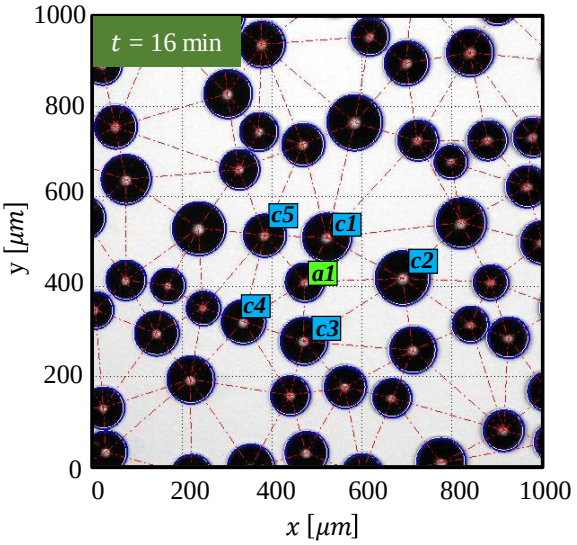

(b)

Figure 4.2. Example snapshot images from the experimental conditions T_{sub} = 10 °C, RH = 70%, and T_{∞} = 20.5 °C at (a) 9 min to (b) 16 min following droplet recognition and tracking.

Figure 4.3. Prediction of the condensation rate of a single droplet within a system of many droplets. (a) Top-down view of the domain used for the PSSM calculation, consisting of droplets inside the experimental field of view at T_{sub} = 10 °C, RH = 70%, T_{∞} = 20.5 °C and t = 31 min (filled red) and artificial droplets generated outside the field of view (filled white). (b) Predicted condensation rate for the droplet of interest, filled blue in (a), as the number of neighboring droplets considered in the model increases. The blue window defines upper and lower bounds of the experimental error. (c) Relative error between the predicted and measured condensation rate and residual of the condensation rate between increments in the number of droplets included. The purple and orange polygons in (a) include all droplets necessary to predict $\dot{m}_{iso}$ with residual ~10^{-15} kg/s and relative error 0.06 % (also shown with corresponding dashed vertical lines in (b) and (c))

Figure 4.3 continued

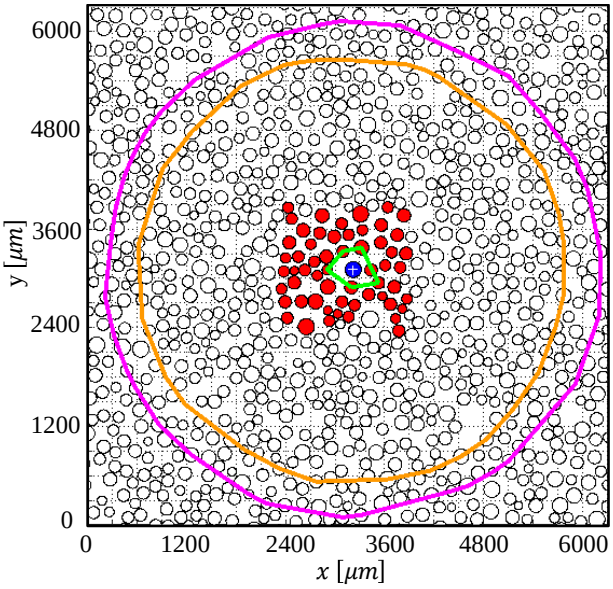

(a)

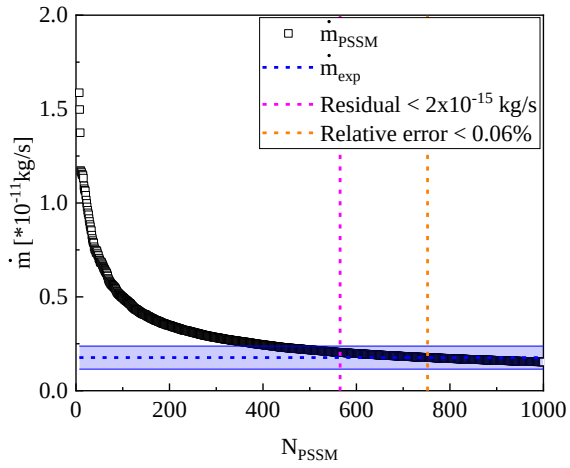

(b)

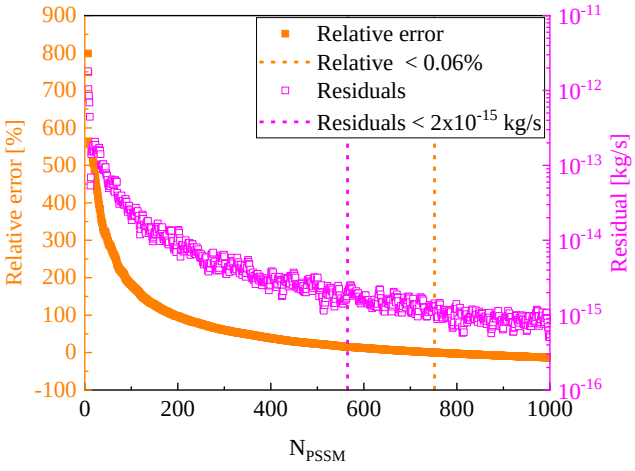

(c)

Figure 4.4. Prediction of the total condensation rate for 30 droplets within a system of many droplets. (a) Top-down view of the domain used in the PSSM calculation with droplets inside the field of view at T_{sub} = 10 °C, RH = 70%, T_{∞} = 20.5 °C and t = 31 min (filled red) and artificial droplets generated outside the field of view (filled white). (b) Predicted total condensation rate for the group of droplets filled blue in (a) versus the number of neighboring droplets considered in the model. The blue window defines upper and lower bounds of the experimental error. Relative error between the predicted and measured total condensation rate and the residual of the total condensation rate between increments in the number of droplets included. The purple and orange polygons in (a) include all droplets necessary to predict $\dot{m}_{iso}$ with residual ~10^{-14} kg/s and relative error 0.15 % (also shown with corresponding dashed vertical lines in (b) and (c))

Figure 4.4 continued

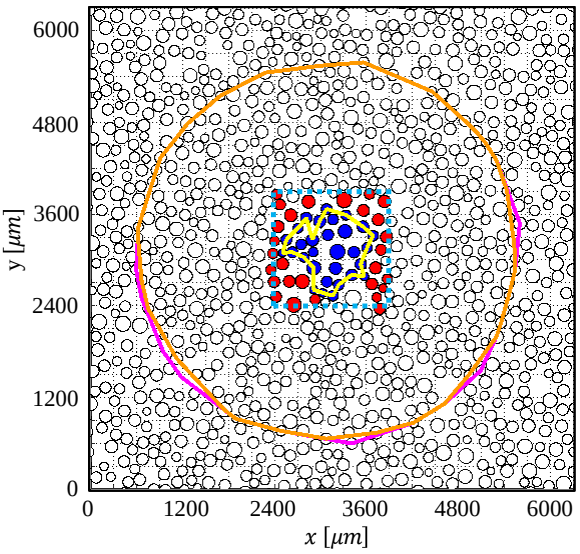

(a)

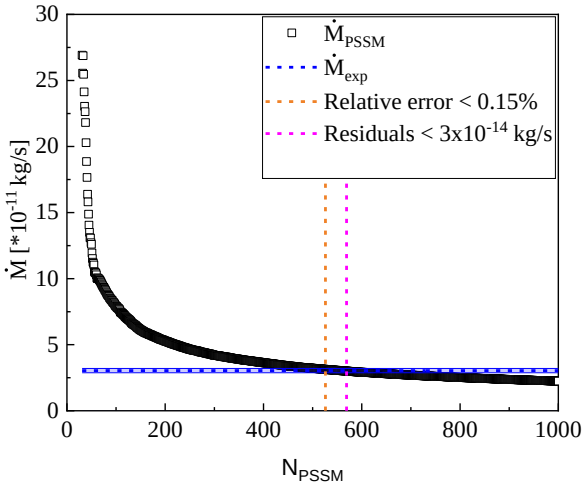

(b)

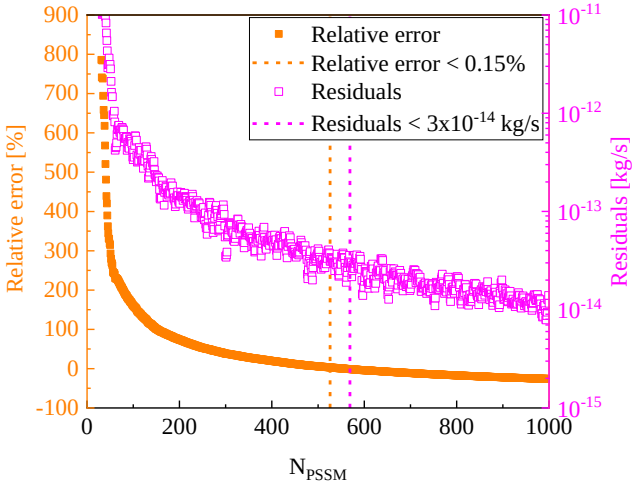

(c)

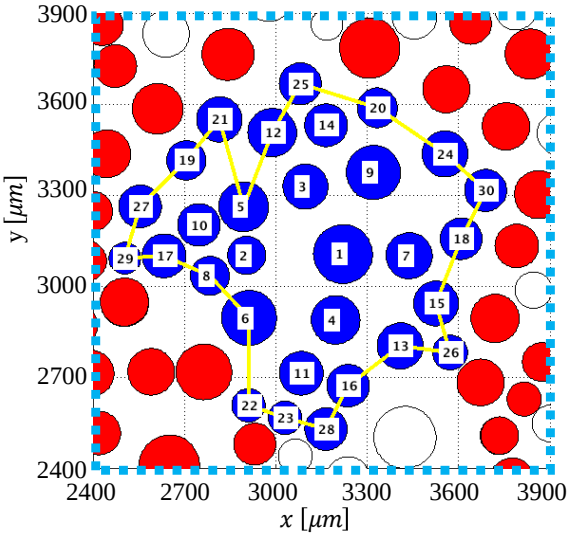

(a)

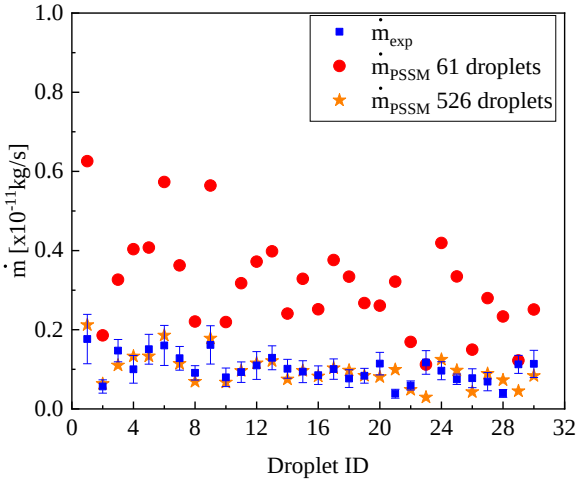

(b)

Figure 4.5. Prediction of individual condensation rate of a group of 30 droplets within a system of many droplets. Magnified view of Figure 4.4 showing the field of view and including tags on the droplets of interest. (b) Measured and predicted individual condensation rates for each tagged droplet of interest.

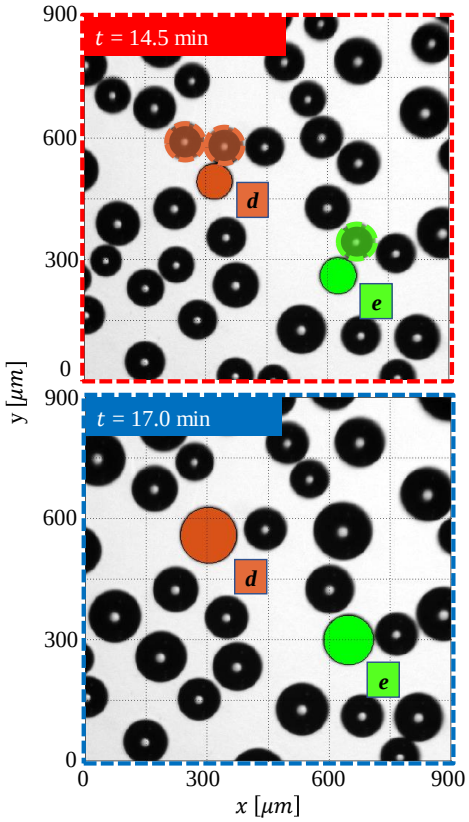

(a)

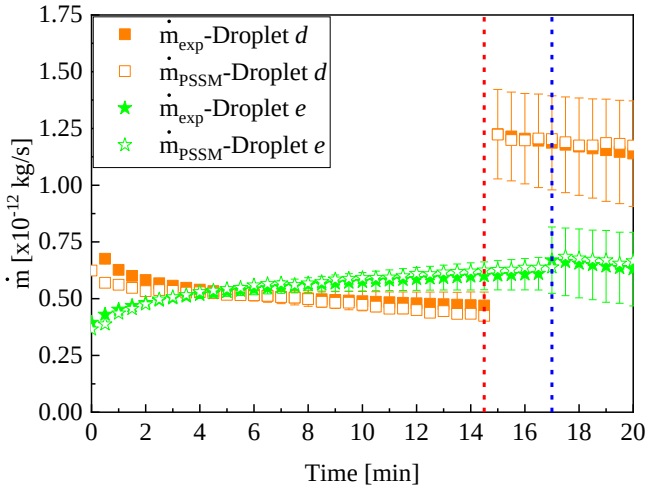

(b)

Figure 4.6. (a) Snapshot images of droplets condensing during condensation experiments at T_{sub} = 10 °C, RH = 70%, T_{∞} = 20.5 °C. The sequence of images shows droplets d and e before (t = 14.5 min) and after (and t = 17.0 min) their respective first coalescence events with neighboring droplets. (b) Temporal evolution of the condensation rates of droplets d and e with vertical lines indicating times that corresponds with the image sequence in (a)

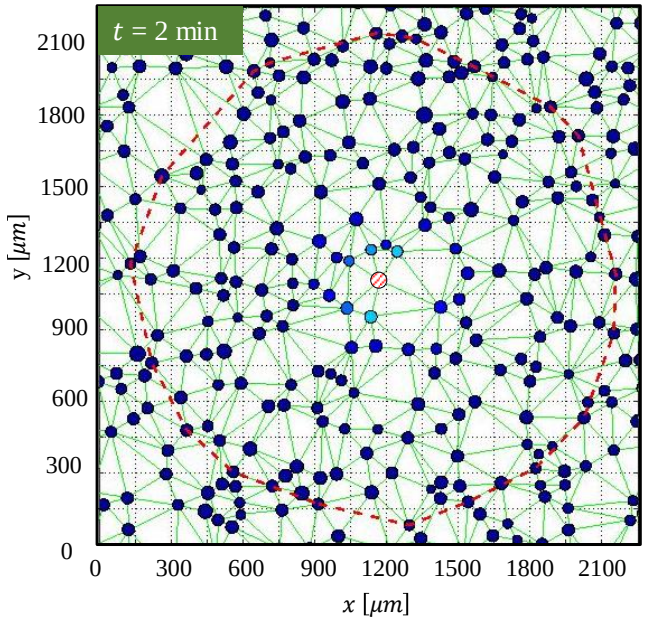

(a)

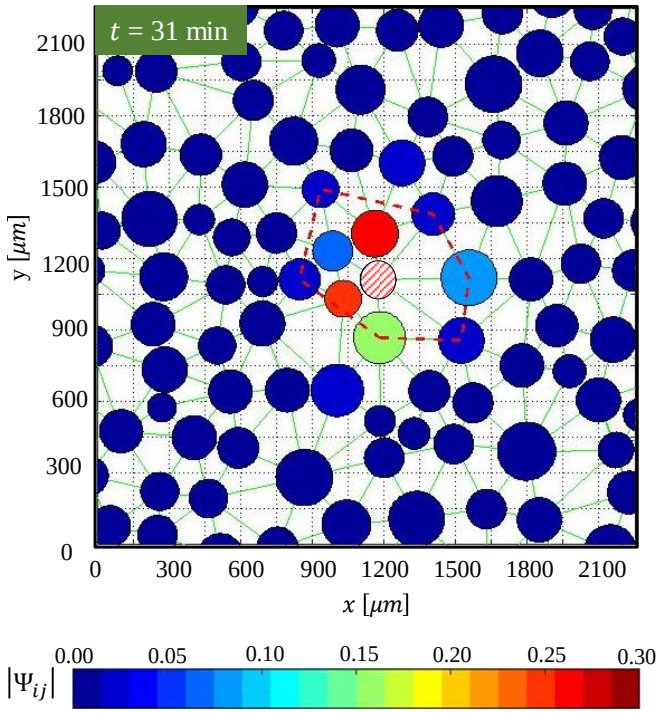

(b)

Figure 4.7. Absolute value of the intensity of interaction between the droplet of interest (dashed circle near the center) with all other droplets in the domain, calculated based on the images taken at (a) t = 2 min and (b) t = 31 min. The fill color of the droplets corresponds to the interaction intensity contour scale (T_{sub} = 10 °C, RH = 70%, T_{∞} = 20.5 °C).

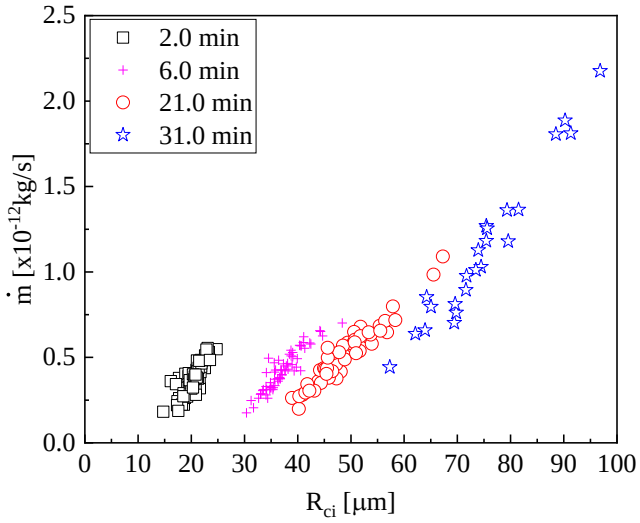

(a)

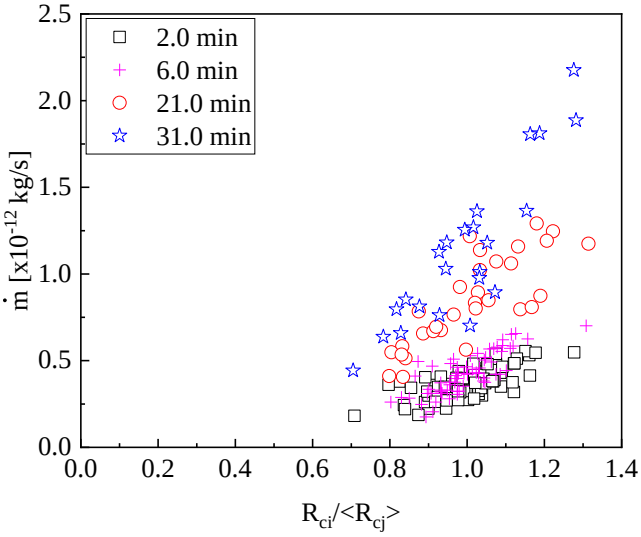

(b)

Figure 4.8. Condensation rate of each droplet versus (a) their respective contact radius. and versus (b) the ratio between the contact radius of each droplet and the average contact radius of its nearest neighbors during experimental conditions T_{sub} = 10 °C, RH = 70%, and T_{∞} = 20.5 °C at t = 2, 6, 21 and 31 min.

Figure 4.9. Condensation rates and Voronoi polygons for droplets in the model domain corresponding to images at (a) t = 2 and (b) t = 31 min (T_{sub} = 10 °C, RH = 70%, and T_{∞} = 20.5 °C). The color filling each circle indicates the predicted condensation rate of the droplet, while the color of the Voronoi polygons around each droplet represents the magnitude of the polygon area.

Figure 4.9 continued

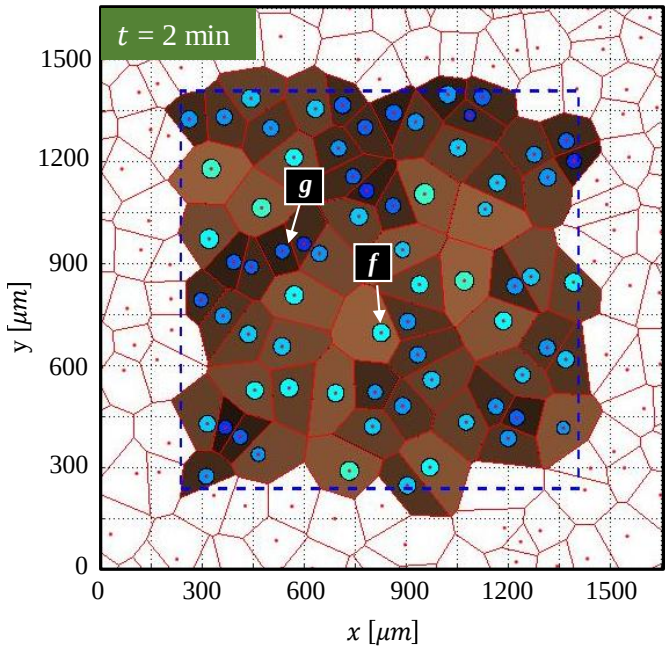

(a)

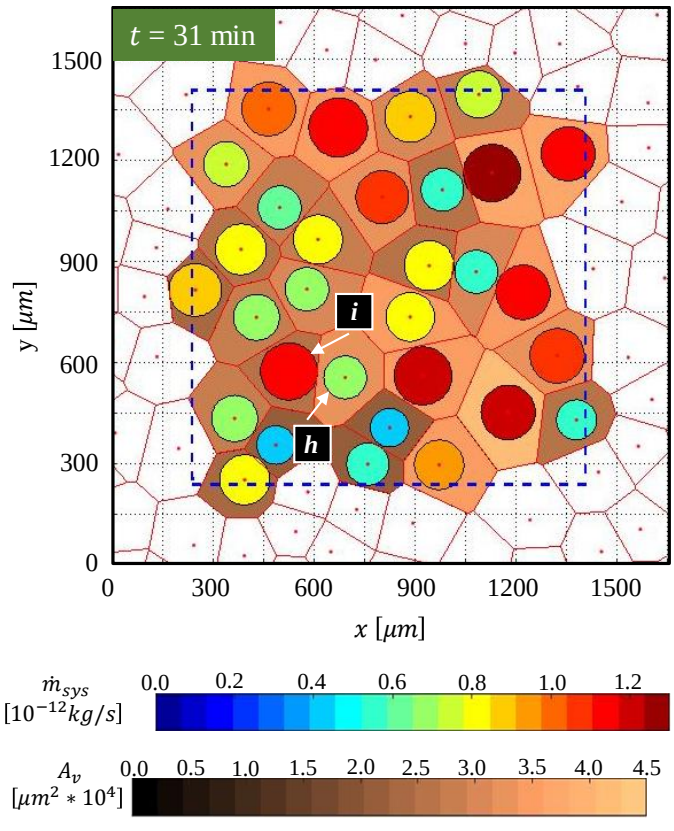

(b)

5. QUANTIFYING THE PATHWAYS OF LATENT HEAT DISSIPATION DURING DROPLET FREEZING ON COOLED SUBSTRATES

A tool for calculating the local vapor distribution around a group of condensing droplets was developed in the previous chapters. This model can also be leveraged to describe the distribution of local vapor during condensation freezing. The main goal of the work presented in the remaining chapters of this document is to characterize mass and heat transfer processes occurring during condensation frosting. The first step towards that goal is to develop a model for heat transfer from a freezing to droplet to its environment that describes changes in the temperature and vapor concentration field around the droplet. This chapter investigates the pathways for dissipation of the latent heat released during single droplet freezing on a cooled substrate. Specifically, side-view IR thermography measurements are employed to calculate the fraction of heat dissipated to the substrate relative to the ambient air surrounding the droplet. High-spatial-resolution temperature measurements are performed inside a cold enclosure to control and reduce spurious thermal radiation from the ambient. Numerical simulations of the solidification process during droplet freezing, which account for the thermal coupling between the droplet and its environment via conduction, evaporative cooling, and natural convection, are benchmarked against experiments. The simulation results are used to quantify the fraction of latent heat released to the substrate and the surrounding air the droplet, as well as to understand the role that each transport mechanism has in altering the water vapor, temperature, and velocity fields in the air surrounding the droplet. The material presented in this chapter has been submitted to a journal and is in review for publication.

5.1 Experimental Description

An experimental facility is built to capture infrared thermography video recordings from a side view during droplet freezing. The test section (schematic diagram shown in Figure 5.1) is capable of cooling the substrate below freezing cooling while maintaining uniform background radiation. To minimize the influence of the background radiation and reduce spurious reflections from the environment, the test section is surrounded by a black-painted (ColorMasterTM Flat Black, Krylon; emissivity of 0.97) aluminum enclosure that is maintained at a constant below-ambient temperature using two temperature-controlled thermoelectric stages (CP-031, TE

Technology, Inc.). The sample substrates are mounted to a stackup comprising an aluminum block (sample holder in Figure 5.1), a thermoelectric plate (ZT8, Laird Technologies), and another aluminum block attached to the outer thermoelectric stage located at the bottom of the facility.

Smooth silicon substrate samples were cleaned and then silanized following the procedure described in Section 4.1.1. The sample surface had a measured average roughness of 0.001 μm (NewView 6000, Zygo) and a contact angle of 91.5 deg using a 5 μl water droplet (ramé-hart, 290-F1). The temperature of the sample is measured with a two-wire Pt RTD (PRTF-10-2-100-1/4-12-E-GG, Omega) placed in a hole located 2.5 mm from the top surface of the aluminum sample holder. This temperature signal closes a control loop that modulates the cooling power delivered by the thermoelectric plate using a temperature controller (MTTC-1410, Laird Technologies). The entire facility is mounted on micrometer stages to allow easy focusing during the IR imaging.

After a liquid water droplet is gently deposited on the substrate, the top lid of the enclosure is bolted to the lower base. Subsequently, the two cooling stages are turned on and after ~15 min the entire test section cools down to -1.5 °C. Then, the thermoelectric controller is turned on with a set-point of -9.0 °C. After ~4 min, the temperature measured by the RTD reaches a constant value within ± 2% of the set-point. The substrate gradually cools down to the setpoint temperature and after ~10 min ice nucleation occurs within the droplet.

The transient temperature of the surface of the droplet is recorded at 50 fps using an infrared camera (SC7650, FLIR). A 50 mm lens (Nyctea, Janos) is connected to the camera with 38 mm extensions that provide a spatial resolution of 0.038 ± 0.004 mm/pixel, where the uncertainty is take as the standard deviation over 8 calibration measurements. A custom-made black body radiator was used to calibrate the infrared camera over a range of set-point temperatures from -8.5 °C to 22.5 °C in 1.0 °C increments. At each setpoint temperature, the IR camera is used to record the digital level averaged over 100 frames. The digital level is fitted as a function of the setpoint temperature with a fourth-order polynomial for each sensor pixel. This pixel-by-pixel calibration is applied to the experimental data. The temperature distribution on the surface of the droplets after completion of recalescence is used to correct for systemic errors caused by background radiation and nonuniform emissivity. The IR thermography data is cropped around the droplets to remove the immaterial background data. Further details on the calibration procedure applied to the IR thermography measurements are provided in Appendix B. IR

thermography recordings on the surface of 10.1 μL and 19.8 μL water droplets during droplet recalescence and subsequent solidification are presented in this chapter.

5.2 Numerical Model Description

Numerical simulations of the transient solidification of a droplet resting on a cooled subtract are implemented in ANSYS Fluent [89]. A 2D axisymmetric model with a fixed grid is used to simulate thermal conduction in the solid substrate, solidification at the freezing front within the droplet, heat transfer and fluid flow in the droplet domain, heat and mass transfer in the surrounding gas domain, phase change, and coupled heat and mass transfer at the droplet interface. Computational domains with droplet geometry and boundary conditions matching the two freezing experiments described in Section 5.1 were implemented. The mesh and geometry (to scale) of the computational domain used for the simulation of the solidification of the 10.1 μL droplet, indicating the key phases, interfaces, and boundaries, used in the numerical simulations is illustrated in Figure 5.2. All the material properties used in the numerical are summarized in Table 5.1. To reduce the level of complexity without sacrificing fidelity, the numerical simulations neglect the volume change due to water expansion during freezing, and therefore the volume and shape of the droplet are assumed equal to that of the droplet prior to recalescence. A maximum increase in droplet volume of ~9% as a result of complete solidification would lead to a ~3% increase in the height of the droplet and have negligible effect on the thermal resistance to heat flow through the frozen portion of the droplet. The following sections provide detailed descriptions of the governing equations and boundary conditions implemented in the numerical simulations.

5.2.1 Droplet Domain

Solidification within the droplet domain is modeled using the enthalpy-porosity formulation [94,95] implemented using the solidification/melting model of ANSYS Fluent [89]. In this formulation, each computational cell is modeled with properties that are determined by a linear relationship between the cell temperature (T)and the fraction of liquid in the cell (β). The latter is defined as:

$$\beta = \begin{cases} 0 & T < T_{sol} \\ \dfrac{T - T_{sol}}{T_{liq} - T_{sol}} & T_{sol} < T < T_{liq} \\ 1 & T > T_{liq} \end{cases} \tag{4.7}$$

where T_{sol} and T_{liq} are the liquidus and solidus temperatures for water, and β decreases from 1 to 0 as the material solidifies (i.e., zero liquid fraction). The narrow region between the solid and liquid phases where β decreases from 1 to 0 is commonly referred to as the mushy zone. Therefore, any thermophysical property ξ (*i.e.* specific heat or thermal conductivity) within the liquid, mushy, and solid regions can be expressed in terms of the liquid fraction as:

$$\xi = \begin{cases} \xi_s & T < T_{sol} \\ (1-\beta)\xi_s + \beta\xi_l & T_{sol} < T < T_{liq} \\ \xi_l & T > T_{lid} \end{cases} \tag{4.8}$$

Considering the small length scale of the droplet and that the maximum velocity of the liquid is limited by the rate of propagation of the freezing front, laminar flow is assumed for the fluid in the liquid and porous-medium-like solid/liquid mushy zone. Under those assumptions, fluid flow within the droplet domain is modeled using the continuity and momentum equations which are expressed as:

$$\rho_l \nabla \vec{V}_l = S_{m,l} \tag{4.9}$$

$$\rho_l \vec{V}_l \cdot \nabla \vec{V}_l = -\nabla p_l + \mu_l \nabla^2 \vec{V}_l + S_p \tag{4.10}$$

where μ_l is the viscosity of water (μ_l = 1.003 x 10 $^{-3}$ kg/m s), $\vec{V}_l$ is the fluid velocity, $S_{m,l}$ is a source term that pertains to mass transport across the interface, which is later discussed in Section 5.2.3, and S_p is the momentum sink due to the reduced porosity in the mushy zone. By further assuming that the flow within the mushy region is governed by Darcy's law, S_p is defined as:

$$S_p = \frac{(1-\beta)^2}{\beta^3 + \varepsilon} E_{mushy} \vec{V}_l \tag{4.11}$$

where ε is set equal to 0.001 to prevent division by zero when $\beta \to 0$, and E_{mushy} is a constant that depends on the morphology of the porous media. The value of this constant determines how

fast the velocity of the material tends to zero as it solidifies, and it is set equal to 1×10^5 in these simulations.

At each cell, the total enthalpy H is computed as the sum of the sensible enthalpy h and latent heat $\Delta H = \beta L$ of the fraction of liquid in the cell, where L is the latent heat of solidification (L = 335000 J/kg for water). Therefore, the latent heat can vary between 0 for a solid cell and L for a liquid cell. Using this definition for the total latent heat, the energy transport within the droplet domain is modeled using the energy equation which is expressed as:

$$\frac{\partial}{\partial t}\left(\rho h\right)+\nabla\cdot\left(\rho\vec{V}h\right)=\nabla\cdot\left(\alpha\nabla h\right)+S_h+S_{h,l} \tag{4.12}$$

where the energy source term S_h in this equation is derived from the enthalpy formulation of convection-diffusion phase change and is expressed as [96]:

$$S_h=\frac{\partial\left(\rho\Delta H\right)}{\partial t}+\nabla\cdot\left(\rho\vec{V}\Delta H\right) \tag{4.13}$$

and the source term $S_{h,l}$ is related to the energy transfer across the interface and is further described in Section 5.2.3

5.2.2 Solid Substrate and Surrounding Gas Domains

Heat transport within the solid substrate domain is modeled assuming that the thermophysical properties of silicon do not vary within the range of temperatures considered. Under this assumption, the energy equation can be expressed as:

$$\frac{\partial T}{\partial t}=\alpha_s\nabla^2T \tag{4.14}$$

To calculate fluid flow velocity, temperature, and water vapor concentration in the gas domain, it is assumed that fluid flow is laminar and Newtonian. The continuity, momentum, and energy equations are respectively:

$$\nabla\left(\rho_g \vec{V}_g\right) = S_{m,g} \tag{4.15}$$

$$\rho_g \vec{V}_g \cdot \nabla \vec{V}_g = -\nabla p_g + \mu_g \nabla^2 \vec{V}_g + \rho_g \vec{g} \tag{4.16}$$

$$\rho_g c_{p,g} \vec{V}_g \cdot \nabla T = k \nabla^2 T + S_{h,g} \tag{4.17}$$

where $S_{m,g}$ and $S_{h,g}$ are mass and energy terms later described in Section 5.2.3 and μ_g is the viscosity of air (μ_g = 1.789 x 10^{-5} kg/m s). By further assuming that the air-vapor mixture in the gas domain follows the ideal gas law, the density of the vapor-air mixture ρ_g can be is expressed as:

$$\rho_g = C_v M_{water} + \left(\frac{p_{atm}}{RT} - C_v \right) M_{air} \tag{4.18}$$

where M_{water} is the molecular weight of water (M_{water} = 0.018 kg/mol), M_{air} is the molecular weight of dry air (M_{air} = 0.029 kg/mol), and the mole concentration of water vapor in the mixture C_v is solved with the following governing equation for diffusive and convective transport in the gas domain:

$$\vec{V}_g \cdot \nabla C_v - \nabla \cdot \left(D \cdot \nabla C_v \right) = 0 \tag{4.19}$$

In equation (4.19) the temperature-dependent diffusion coefficient D is given by:

$$D(T) = D_{ref} \left(\frac{T}{T_{ref}} \right)^{1.5} \tag{4.20}$$

Further details on the implementation of equation (4.19) using user-defined scalar (UDS) functions in Fluent is provided in the Appendix C.

5.2.3 Droplet-Gas Interface

Heat and mass transport across the interface between the droplet and gas domains is modeled by neglecting the effects of capillary pressure and interfacial phase-change resistances across the droplet-gas interface. The effects of a capillary pressure difference across the interface during droplet condensation and freezing are known to be negligible for droplets with radius larger than ~1 μm [67] . In the presence of non-condensable gases (i.e., for an air-water mixture), the interfacial resistances to condensation and evaporation are significantly smaller than the resistance to diffusion of vapor. Therefore, the saturation vapor pressure is calculated based on the local temperature of the droplet-gas interface. Because the saturation vapor pressure above an ice surface is smaller than above a supercooled liquid water surface at the same temperature [97], the saturation vapor pressure also depends on the local fraction of ice on the surface of the droplet. To simplify implementation in the numerical simulations, cells on the face of the droplet-air interface above 0 °C are treated as liquid, whereas cells that are below 0 °C are treated as ice. Expressions for the saturation vapor pressure above ice and supercooled liquid surface, as well as further details on the implementation of user-defined functions to calculate the content of water inside the air domain are provided in Appendix C.

At the liquid-gas interface, shear stress along both sides of the interface are set as zero and the vapor flux across the interface, which can be induced by condensation or evaporation depending on the local vapor saturation pressure at the surface, is expressed as:

$$m'' = M_v \left(-D\vec{n} \cdot \nabla C_v + v_n C_v \right) \tag{4.21}$$

where the first term inside the parentheses on the right-hand side is the vapor transport due to mass diffusion, and the second term represents mass convection by Stefan flow. Because dry air does not pass through the droplet-gas interface, the flux of air is set to zero at the interface:

$$0 = M_g \left(-D\vec{n} \cdot \nabla \left(C_g - C_v \right) + v_n \left(C_g - C_v \right) \right) \tag{4.22}$$

Therefore, the velocity of the vapor crossing the interface can be expressed as:

$$v_n = -\frac{1}{C_g - C_v} D\left(\vec{n} \cdot \nabla C_v\right) \tag{4.23}$$

By coupling equations (4.21) and (4.23), the mass flux at the interface can be written as:

$$m'' = -\frac{M_v D}{1 - C_v / C_g}\left(\vec{n} \cdot \nabla C_v\right) \tag{4.24}$$

where the vapor molar concentration in the gas and the vapor at the interface are respectively calculated as $C_g = p_{atm} / RT_{lv}$ and $C_v = p_{atm}\left(T_{lv}\right) / RT_{lv}$.

The mass transport across the interface is modeled by adding mass sources and sinks to the mesh cells adjacent to either side of the interface, following an analogous procedure as explained in Refs. [98,99]:

$$S_{m,g} = \frac{m'' A_{cell}}{V_{cell,g}} \tag{4.25}$$

$$S_{m,l} = -\frac{m'' A_{cell}}{V_{cell,l}} \tag{4.26}$$

where A_{cell} is the interface area of the specified cell adjacent to the interface and V_{cell} is the cell volume. Energy transport induced by evaporation and condensation processes are modeled by adding energy sources in the mesh cells adjacent to the interface on either side:

$$S_{h,g} = S_{m,g} h_s\left(T\right) \tag{4.27}$$

$$S_{h,l} = S_{m,l} h_s\left(T\right) + S_{m,l} h_{f,g} \tag{4.28}$$

$$h_s\left(T\right) = c_p\left(T - T_{ref}\right) \tag{4.29}$$

The first terms on the right-hand sides of equations (4.27) and (4.28) represent the sensible heat contributed by the mass source, while the additional term in equation (4.28) accounts for the latent heat adsorbed/released during evaporation/condensation, where $h_{f,g}$ is the latent heat of

evaporation ($h_{f,g}$ = 2.497 x10^6 J/kg). The temperature T_{ref} in equation (4.29) is an arbitrary reference temperature implemented in the simulation set equal to 0 °C.

5.2.4 Other Boundary Conditions

At the outer boundary of the gas domain, 100 times larger than the droplet radius, the concentration of vapor is calculated using:

$$C_v = \frac{RH\, p_{sat}(T_\infty)}{RT_\infty} \tag{4.30}$$

where RH is the relative humidity of the air and T_∞ is the temperature of the air in the far field. For all the simulations presented in this paper, the relative humidity and ambient temperature were set respectively equal to 30 % and -1.5 °C.

The average of the contact line temperature measured from the experiments is used as a time-dependent boundary condition at each cell in the bottom of the droplet domain employing UDFs. The temperature at the bottom of the substrate is set constant and equal to the set-point temperature of the thermoelectric controller. To ensure thermal coupling between all the interior boundaries in the domain, the temperature across these boundary was assumed to be continuous $T_1 = T_2$ and any contact thermal resistances are neglected $k_1\left(n_1 \cdot \nabla T_1\right) = k_2\left(n_2 \cdot \nabla T_2\right)$.

5.2.5 Initial Conditions

Prior to formation of the freezing front, i.e., the solid ice that progresses from the bottom to the top of the droplet, some fraction of the liquid is frozen as dendrites during the recalescence process (as described alongside discussion of Figure 2.1). The fraction of this ice formed it is often calculated by equating all the latent heat it releases to the sensible heat required to increase the supercooled droplet temperature up to 0 °C via an adiabatic process. In this work, the initial fraction of ice is estimated considering energy losses to the surroundings of the droplet. Therefore, the latent heat released during recalescence is equated to the heat loss to the surroundings in addition to the sensible heating of the formed ice and the remaining liquid up to 0 °C:

$$\frac{\rho_l v x \Delta H}{\Delta t_{rec}} = \frac{\rho_l v x c_{p,s} \Delta T}{\Delta t_{rec}} + \frac{\rho_l v (1-x) c_{p,l} \Delta T}{\Delta t_{rec}} + q_{rec,loss} \tag{4.31}$$

where $x = 1 - \beta$ is the fraction of ice, Δt_{rec} is the duration of recalescence, v is the volume of the droplet before recalescence, and $q_{rec,loss}$ is the total heat transferred to the ambient air and to the substrate during recalescence. The heat loss, $q_{rec,loss}$, is estimated by numerically solving the rate of heat transfer between the droplet at 0 °C and its surroundings (i.e., the substrate and gas domains with boundary conditions described above) under quasi-steady conditions. The temperature distributions in the in the gas and solid domains obtained from these quasi-steady simulations are also used as the initial conditions in the transient simulation of solidification. The initial fraction of liquid calculated using equation (4.31) is used in equation (4.7) to calculate T_{sol} and T_{liq}, which are then input as initial conditions to the solidification/melting model to set the corresponding initial fraction of liquid. Heat losses during recalescence of the10.1 μL and 19.8 μL droplets were estimated to be 25 W and 42 W, which correspond to initial fractions of ice equal to 0.17 and 0.21, respectively.

5.2.6 Numerical Simulation Settings

After calculating the initial fraction of ice and the initial temperature fields within all the computational domains using the method described in Section 5.2.5, the numerical solution of the transient solidification is set to use the SIMPLE algorithm for pressure-velocity coupling and the first-order implicit scheme for time-discretization, with a time step of 0.01 s. To confirm that the results are independent of the geometrical characteristics of the computational domain such as mesh and domain dimensions. A mesh size independence check was performed to confirm that the results are insensitive to further mesh refinement a mesh with twice as many cells resulted in less than a 1% change in the freezing time. To confirm the results are independent of the size of the domain, simulations were performed to show that the freezing time changed less than 1% when the size of the domain were increased from 20 to 100 times the droplet radius. The mesh used (shown in Figure 5.2), for the case of a 10.1 μL droplet, has a total of 119,450 quadrilateral cells. Similar mesh and domain sizes were employed for the 19.8 μL droplet case.

5.3 Results

This section presents the transient infrared (IR) surface temperature data acquired during the recalescence and solidification processes of individual droplets having two different volumes of 10.1 μL and 19.8 μL. These measurements are used to reveal details of the crystallization dynamics during recalescence in Section 5.3.1 and to benchmark the model for droplet solidification in Section 5.3.2. In section 5.3.3, the temperature, water vapor concentration, and velocity fields obtained from the numerical simulations are used to qualitatively assess the different transport mechanism that participate in the dissipation of latent heat from a solidifying droplet to its environment. A quantitative description of each pathway for latent heat dissipation is provided in Section 5.3.4.

5.3.1 Crystallization Dynamics During Recalescence

Side-view infrared surface temperature maps of the droplet during recalescence reveal details of the relationship between the crystallization dynamics and heat transfer. A sequence of snapshots showing the evolution of the temperature distribution on the surface of 10.1 μL and 19.8 μL droplets undergoing recalescence are shown in Figure 5.3. Immediately prior recalescence at t = 0 s, both droplets are in the liquid state and have been supercooled to an average surface temperature of approximately -8.3 °C. At this stage, there is a slight vertical temperature gradient in the liquid due to heat conduction from the droplet to the substrate, with a total temperature differential across the droplet height on the order of ~ 1 °C. Subsequently at t = 0.02 s, ice crystals heterogeneously nucleate at the base of the droplet in contact with the substrate and begin to propagate towards the top of the droplet. The temperature maps indicate two well-defined regions, each with a near-uniform temperature distribution, that are separated by a sharp temperature gradient which defines the crystallization front. Regions ahead of the crystallization front remain in the supercooled liquid state at -8.3 °C whereas the temperature of the water ice-mixture, in the region where crystallization has occurred, becomes close to the equilibrium freezing temperature of 0.0 °C. At later times, throughout propagation of the crystallization front, additional crystallization maintains the temperature of this water-ice mixture close to 0.0 °C.

The crystal growth dynamics during recalescence are known to be related to the degree of supercooling of the liquid phase [100–102], droplet size, contact angle [103,104], and thermal properties of the substrate [105]. The sequence of images shown in Figure 5.3 provide evidence

that the crystallization front propagates at a slightly lower velocity in the droplet of a larger size. For the 10.1 μL and 19.8 μL droplets with heights of 1.72 mm and 2.10 mm, the total times to complete recalescence are 0.10 s and 0.14 s, respectively. This corresponds to average crystallization front velocities of 17.2 mm/s and 15.0 mm/s, which are in accordance with a typical crystallization speed of ~10 mm/s measured for films on substrates with thermal conductivities similar to silicon [105]. Further, a decelerating rate of crystal growth shown in the sequence of images in Figure 5.3 indicates a spatial dependence of the crystallization dynamic. In the first few hundredths of seconds during recalescence, between 0.00 s < t < 0.06 s, the crystallization front proceeds much faster (~34 mm/s) than at later times t > 0.06 s, when the crystallization front advances at ~8 mm/s. As the front progresses, and the mass of liquid water in the water-ice mixture available to absorb the latent heat released reduces, this reduces the rate at which crystallization occurs. Similar results have been reported by Jung *et al*. [103] while tracking the evolution of the crystallization front using high-speed side-view optical visualization.

5.3.2 Temperature Distribution on the Surface of Solidifying Droplets

The droplet surface temperature maps measured from IR thermography during droplet solidification (after recalescence) are used to benchmark the numerical simulations by direct comparison. Figure 5.4 presents a sequence of side-view surface temperature contours at several time steps during the solidification of 10.1 μL and 19.8 μL droplets. The temperature plots obtained from the simulations are shown for a full droplet by revolving the droplet-gas interface temperature around the axis of symmetry of the computational domain. Overall, the numerical simulation qualitatively matches the measured temperature distribution and time to complete solidification, with further discussion below.

The sequence of side-view surface temperature contours presented in Figure 5.4 shows that, at each time interval between droplet recalescence and complete solidification, the portion of the droplet above the solidification front remains at a temperature close to the freezing equilibrium temperature of 0 °C, with any variations on the order of the temperature resolution. Meanwhile, a well-defined temperature gradient develops within the growing ice layer below the solidification front. As the solidification front pushes the water-ice mixture upward, the tip of the droplet forms a conical apex in the experiments, which is not present in the simulation results because volume changes during the solidification process are neglected. These results confirm that this does not

lead to significant deviations in the temperature or freezing times when compared with the experiments. Once solidification has occurred throughout the droplet volume, the frozen droplet cools down to a temperature near the temperature of the substrate (-9.0 °C).

A more quantitative comparison between the IR thermography and simulation data is presented in the plots of the temperature along the interface shown in Figure 5.5, where the length along the arc (s) is normalized by the radius (R) such that $s/R = 0$ represents the contact line of the droplet and $s/R = 1$ corresponds the tip of the droplet. For example, at t =5.10 s in Figure 6 (a), the temperature of the droplet at the contact line of the droplet ($s/R = 0$) is -4.82 °C and increases with s/R up to T_{eq}, which corresponds to the location of the solidification front at $s/R = 0.27$. Along the section of the interface that has not yet solidified, $0.27 < s/R < 1.0$ the temperature remains close to T_{eq}. At subsequent times, as the solidification front advances towards the tip of the droplet, the temperature at the contact line of the droplet decreases. When the solidification process completes at t = 21.70 s, the temperature difference between the contact line and tip of the droplet is due to conduction through the solid droplet. At each location on the surface of the droplet, throughout the solidification process for both the 10.1 μL and 19.8 μL droplets, the average relative error between the measured and simulated temperatures is below 4.1%, indicating that the numerical simulation approach accurately captures the governing mechanisms that drive heat transfer during droplet solidification.

Overall, the surface temperature plots along the normalized arc length during solidification of the 19.8 μL droplet present similar trends as for the 10.1 μL droplet, except for one subtle difference worth noting. At any given time after recalescence, for example after approximately 5 s, 10 s and 15 s, the temperature at the contact line of the 10.1 μL droplet is slightly lower when compared to the temperature at the contact line of the 19.8 μL droplet. This is because the 10.1 μL droplet is at a later stage of the solidification process for which a larger percentage of the water has solidified. This strong dependence of the substrate temperature with time clearly indicates that a time-dependent boundary condition at the base of the droplets must be considered.

5.3.3 Mechanisms of Heat and Mass Exchange Between the Droplet and Surroundings

In this section, the temperature and liquid fraction distributions within the 10.1 μL droplet, as well as the water vapor mass fraction and the velocity vector field in the gas domain (near the

gas-droplet interface), are used to identity the mechanisms that drive heat and mass transport from a freezing droplet to its environment. A time sequence of the temperature distribution contours in the simulation domain near the droplet are shown in Figure 5.6 (a). The temperature gradients in the contours suggest two primary paths of heat transfer: (1) from the droplet to the solid substrate and (2) from the droplet to the surrounding ambient gas. Different mechanisms drive heat transfer through each of these pathways. Within the solid substrate domain, heat conduction is driven by the temperature difference between the base contact area of the droplet and the lower wall of the substrate. Whereas in the gas domain, the temperature and concentration differences between the droplet-gas interface and its surroundings drives combined diffusion and convection, as well as phase change at the droplet-air interface, with characteristics that depend on the stage of the solidification process. The influence of each one of these transport mechanisms on the solidification process is assessed in Sections 5.3.3.1, 5.3.3.2, and 5.3.3.3.

5.3.3.1 Heat Diffusion in the Solid Substrate

Just after the recalescence process, at t = 0.10 s in Figure 5.6 (a), the temperature distribution within the substrate shows that a portion of the heat released during recalescence locally heats the substrate below the droplet and the air near the droplet-gas interface. The temperature difference between the droplet-substrate interface and the lower wall of the substrate drives heat away from the droplet and spreads laterally within the substrate and into the ambient air. As the solidification process advances (e.g., t = 10.10 s), the latent heat released at the solidification front is conducted through the solidified part of the droplet to the substrate and the air around the droplet. This results in a temperature field inside the droplet with isotherms that increase in the direction from the the location of the freezing front to the base. The thermal resistance of the solid part of the droplet increases as the solidification front advances, which causes a decrease in the temperature at droplet-substrate interface. As a result, heat diffusion within the substrate reduces as solidification proceeds. At t = 21.70 s, when the droplet has completely solidified, the temperature difference between the droplet base and the lower wall of the substrate reduces significantly.

5.3.3.2 Heat Transport in the Gas Domain

The temperature difference between the droplet-gas interface and its surroundings (both the far-field air temperature and the substrate temperature) not only drives heat diffusion away

from the droplet through the air domain, but it also creates density gradients that drive flow in the air domain. Figure 5.6 (b) shows a time sequence of velocity vector fields in the gas domain along with the liquid fraction in the droplet during the solidification of the 10.1 μL droplet. At the onset of the solidification (t = 0.10 s in Figure 5.6 (b)), cold air flows from regions of the gas domain located on the sides of the droplet toward hotter regions of the gas domain above the droplet. At subsequent times, when the solidification front has progressed within the droplet, heat exchange via diffusion and convection are localized to within the section of the interface above the solidification front, which remains close to 0 °C. At t = 10.10 s in Figure 5.6 (b), the additional cooling produced by the combined effect of the heat diffusion, natural convection, and evaporation drives additional solidification within the region of the droplet near the droplet-gas interface. Meanwhile, due to a decreasing interface temperature in the region behind the solidification front, the mean velocity of air flow decreases, which reduces the cooling induced by natural convection. Once the solidification process is completed, water vapor is driven away from the droplet due to a small concentration difference from the surface of the droplet to the far field.

5.3.3.3 Mass Transport in the Gas Domain and Evaporative Cooling at the Gas-Droplet Interface

A time sequence of mass vapor fraction contour plots in the gas domain around the 10.1 μL droplet is shown in Figure 5.6 (c). The concentration gradients indicate that evaporated water vapor is transported away from the droplet-gas interface to the ambient via both vapor diffusion and convection. At the onset of the formation of the solidification front (t = 0.10 s), the mass fraction of water vapor in the air near the droplet-gas interface is uniform and about four times larger than the fraction of water vapor far away from the interface. This water vapor gradient drives diffusion of water vapor into the ambient air. However, in contrast to the hemispherically uniform water vapor fraction field produced by an evaporating droplet driven by vapor diffusion alone, convection alters the iso-concentration contours (as shown at t = 0.10 s in Figure 5.6 (c)). Dry air flowing in from the sides of the droplet induces stronger evaporation near the contact line of the droplet than near the top of droplet. Differences in temperature along the interface induced by evaporative cooling are not appreciable in the temperature contours because there are suppressed by the additional solidification process occurring within the droplet after recalescence. At t = 10.10 s, the concentration of water reduced in the air near the droplet surface below the solidification front, which localizes evaporation to the region above the solidification front. When

the droplet has solidified, the saturation pressure above the surface of the frozen droplet is smaller than the concentration of vapor far away from the droplet, driving vapor diffusion away from the droplet-gas interface. This prediction of the complete temperature and vapor concentration field around the droplet can be used for understanding the interaction of a freezing droplet with its environment. For example, these temperature and concentration fields along the substrate near the droplets could be used as a tool to study the formation of condensation halos with higher fidelity than previous literature.

5.3.4 Pathways for Heat Dissipation During Droplet Solidification

The solidification modeling results are used to calculate the fraction of latent heat that is transferred to the substrate versus the ambient air. The total heat transfer rate through the substrate contact area, as well as separately integrated over the droplet-gas interface, at each time step during the solidification process is shown in Figure 5.7 (a) for the 10.1 μL and 19.8 μL droplets. The heat transfer through the droplet-gas interface is separately delineated in Figure 5.7 (b) between the mechanism of evaporative cooling and the combined contributions of heat diffusion and natural convection cooling. At early stages of the solidification process, the latent heat released rapidly increases to its maximum value; as the solidification front progresses, the heat transfer rates through the substrate and the droplet interface decrease. As it was described in Sections 5.3.2 and 5.3.3, heat diffusion transfer to the solid substrate is limited by the thermal resistance of the solid part of the droplet behind of the solidification front, which increases as the solidification front advances. Meanwhile, heat transfer across the droplet interface reduces due to the combined effect of: (1) heat and mass diffusion becomes confined to the upper section of the droplet surface ahead of the solidification front; and (2) a reduction of the convective heat and mass transport that results from a decreases in the velocity of the dry air drawn in from the sides of the droplet. In general, the heat transferred through the interfaces of the droplet depends on the area, and therefore the heat transfer rates are lower for the 10.1 μL compared to the 19.8 μL droplet.

Throughout the entire duration of the solidification process, the fraction of latent heat that is transferred to the substrate is at least one order of magnitude larger than the heat transferred to the ambient air. For the 10.1 μL droplet, the maximum heat transfer rate crossing the droplet-gas interface is 5.9×10^{-3} W, while the maximum heat transfer rate across the contact area is about 68 times larger at 4.0×10^{-1} W (the ratios are similar for the 19.8 μL droplet). Therefore, conditions

that alter the diffusion of heat to the substrate (e.g., substrate thermal conductivity, droplet contact angle) would have a more severe impact on the dynamics of solidification than changes in ambient conditions (e.g., ambient temperature and relative humidity). However, considering the effects of the ambient conditions is nevertheless essential for a complete description of the interactions of a freezing droplet with its environment. Because droplet freezing rarely occurs in isolation, prediction of the interaction between a droplet and its environment presented in this paper provide a framework for understanding the propagation of frost, which depends on the evaporation of supercooled liquid neighbors and ice bridging with other liquid droplets.

5.4 Conclusion

This work uses infrared (IR) temperature measurements on the surface of a freezing droplet, as well as a numerical simulation benchmarked with a direct comparison of the temperature maps, to quantitatively describe the transport mechanism that determine the pathways for latent heat dissipation from a droplet freezing on a cooled substrate to its surroundings. The experimental technique used in this work demonstrates that, by reducing ambient radiation during sub-freezing infrared (IR) measurements, temperature maps with high spatial resolution can be used to track the evolution of the crystallization front during droplet recalescence, as well as to resolve the temperature gradients at the surface of solidifying microliter droplets. Contrary to highly simplified models for the describing the interaction between a freezing droplet and its surroundings that are available in the literature (e.g., adiabatic recalescence, constant droplet base temperature, adiabatic droplet-gas interface), the modeling approach presented in this paper uses the IR temperature data at the contact line of the droplet as boundary condition and provides a full description of the driving mechanism for heat and mass exchange between a freezing droplet, the substrate, and the ambient air. These combined advances enable the experimental and modeling approach presented in this paper to not only track the dynamic of the solidification front, but to directly compare the temperature maps (with average error below 4.1%).

The simulation results indicate that heat transfer rate to the substrate of the droplet is at least one order of magnitude greater than the heat transferred to the ambient air. Most of the latent heat released during the solidification process spreads within the substrate, whereas the small portion of the latent heat that is lost the ambient air is concentrated in the region of the droplet surface above the solidification front. Heat exchange via heat conduction, natural convection, and

evaporative cooling at the droplet-gas interface lead to corresponding changes in the ambient temperature, velocity, and vapor concentration fields around the droplet. Evaporative cooling only accounted for a small percentage of the total heat exchange at the droplet-gas interface, whereas the combined heat diffusion and natural convection accounted for most of the cooling at the droplet-gas interface.

In spite of the seemingly small role of the heat and mass transport through the droplet-gas interface in the solidification of a single droplet, in terms of the total heat exchange, it nevertheless has a critical influence on the mechanisms that govern frost propagation. Droplet freezing rarely occurs in isolation, but rather, during condensation freezing, individual droplets freeze while exchanging heat and mass with neighboring supercooled and frozen droplets. The methodology presented in this paper, which accurately describes the heat and mass transfer process between a freezing droplet and its environment, may be a powerful tool for understanding the interactions between a freezing droplet and its neighbors during the propagation of frost on a cooled substrate, as well as the evaporation of neighboring droplets during condensation halo formation.

Table 5.1. Thermophysical properties used in the simulations.

Properties	Water	Ice	Gas	Substrate
density, ρ (kg/m^3)	999.8 at 0.1 $^{\circ}C$	917.5 at -5 $^{\circ}C$	1.298 at -1.5 $^{\circ}C$	2329
thermal conductivity, k (W/mK)	0.58	2.25	0.0242	148
thermal capacity, c_p (J/kg K)	4191	2027	1006.43	711.61

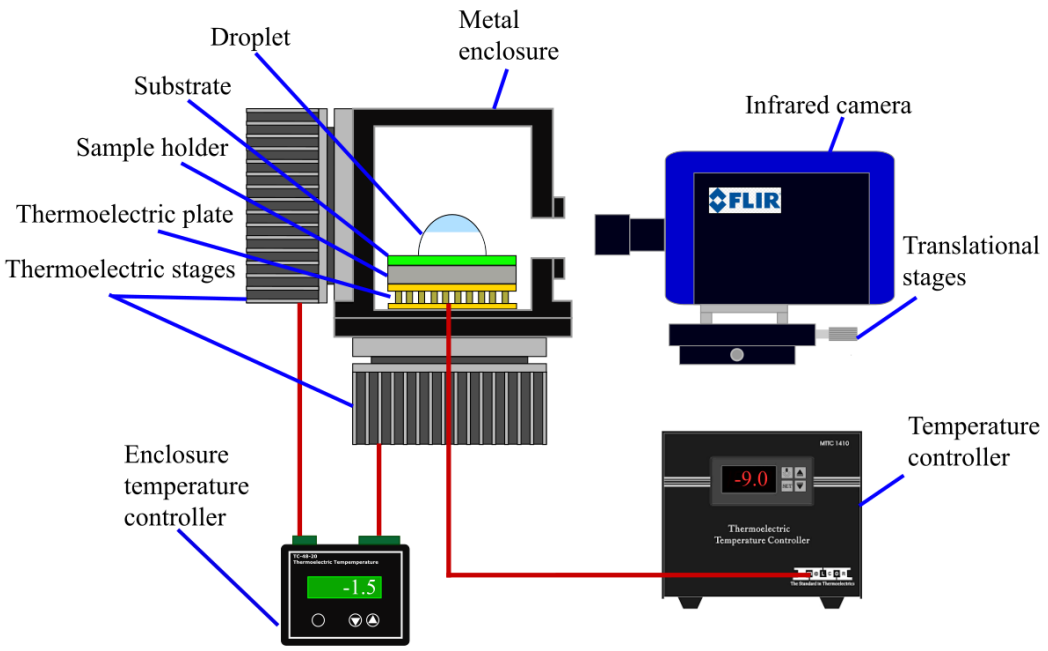

Figure 5.1. Schematic diagram of the experimental facility used for droplet freezing characterization (not to scale).

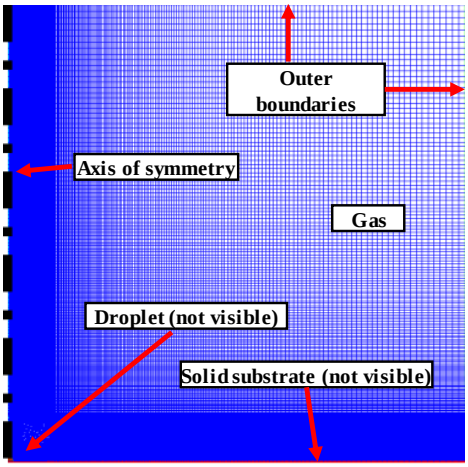

(a)

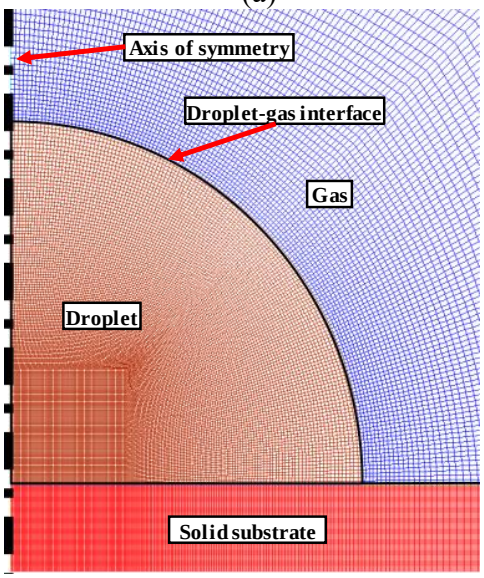

(b)

Figure 5.2. Key phases, interfaces, and boundaries of the numerical simulation domain used for the simulation of the solidification of the 10.1 μL droplet(with mesh overlay), with views of (a) the full domain and (b) a zoomed view to reveal the details near the droplet resting on the substrate.

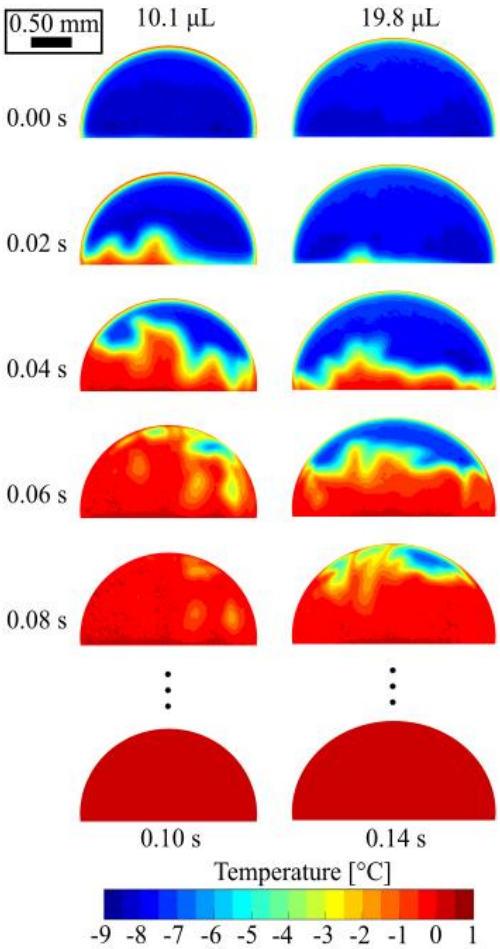

Figure 5.3. Time sequence of the surface temperature maps for 10.1 µL and 19.8 µL droplets during solidification after recalescence. The experimental images are obtained from the IR thermography measurements and the simulation images are generated by revolving the predicted temperature at the droplet interface around the axis of symmetry.

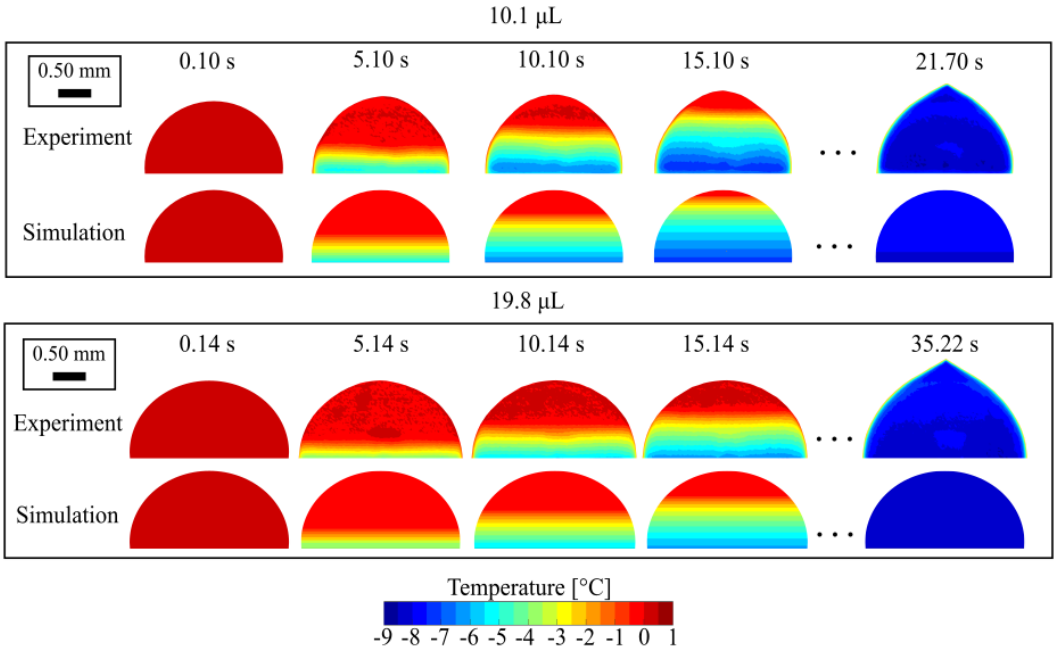

Figure 5.4. Time sequence of the surface temperature maps for 10.1 µL and 19.8 µL droplets during solidification after recalescence. The experimental images are obtained from the IR thermography measurements and the simulation images are generated by revolving the predicted temperature at the droplet interface around the axis of symmetry.

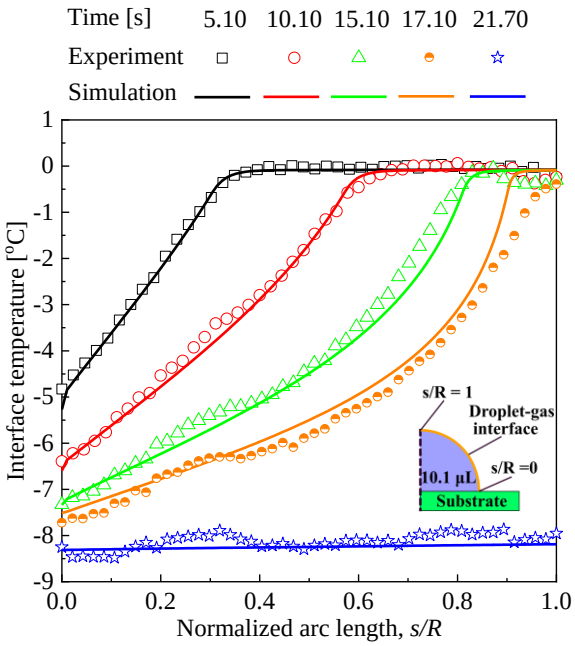

(a)

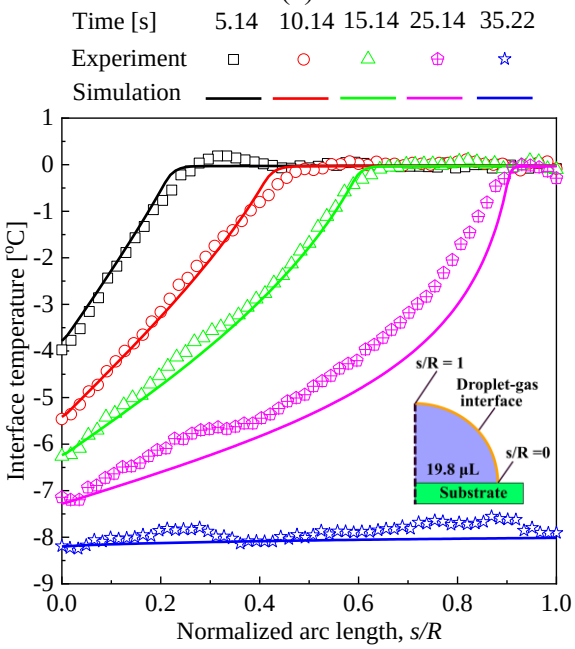

(b)

Figure 5.5. Temperature profiles along the droplet interfaces for (a) 10.1 µL and (b) 19.8 µL droplets at multiple different times throughout solidification after recalescence. Infrared thermography experiments (symbols) are compared to the numerical simulations (solid lines). The location along the arc of the interface (s) is normalized by the droplet radius (R).

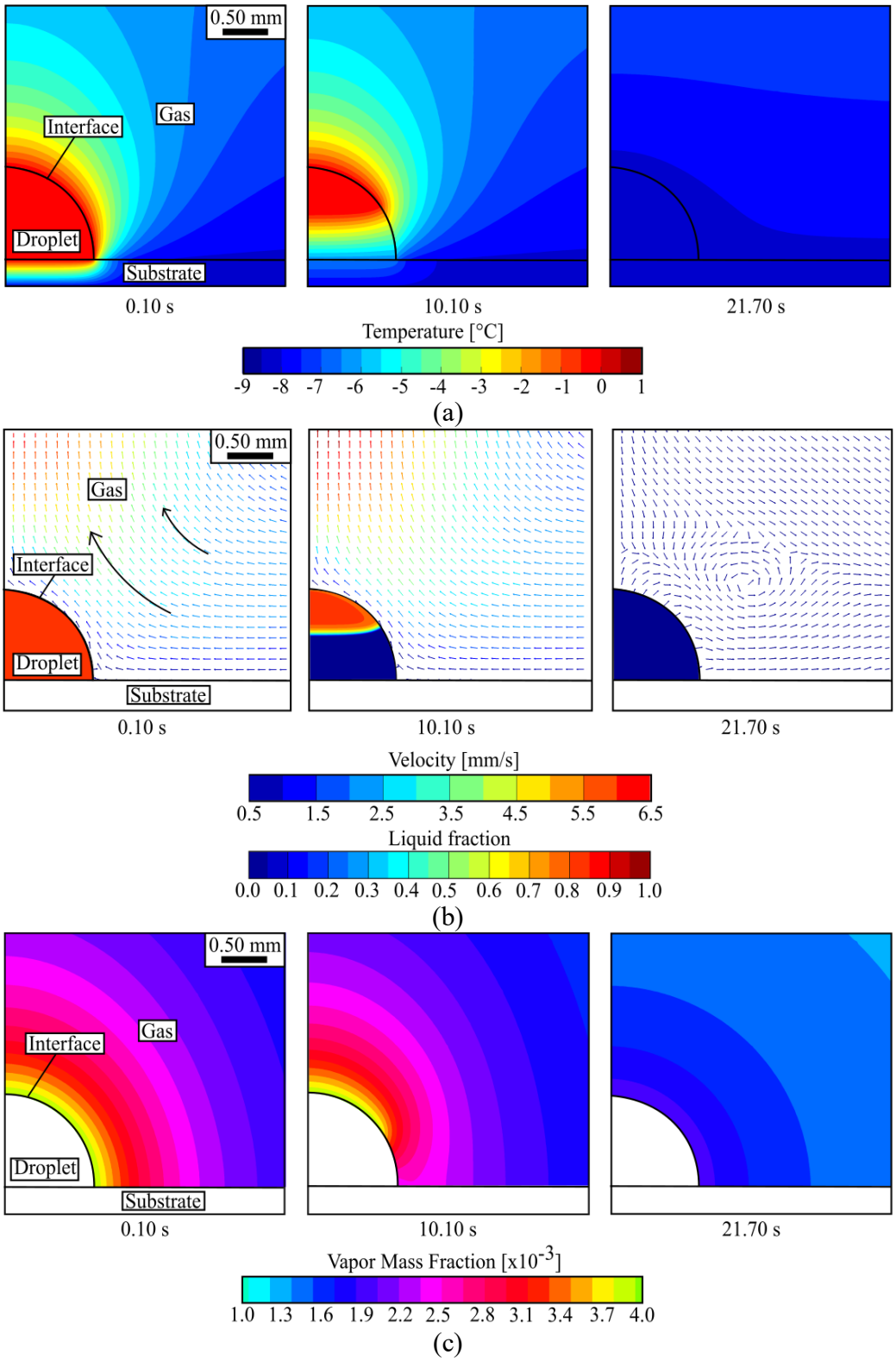

Figure 5.6. Time sequence of (a) temperature contour plots, (b) liquid fraction contour plots (within the droplet) and velocity field (in the gas domain), and (c) mass vapor fraction contour plots (in the gas domain) from the numerical simulations for the 10.1 μL droplet.

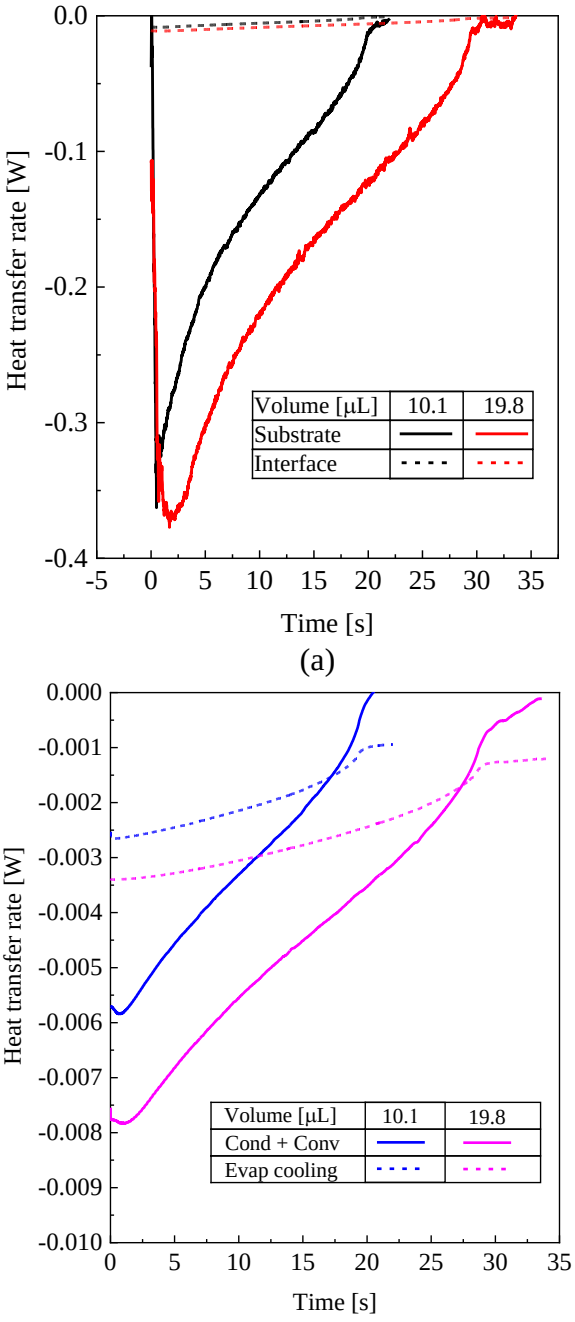

Figure 5.7. Heat transfer rate across (a) the contact area of the droplet (solid lines) and the droplet-gas interface (dashed lines). (b) Heat transfer rate across the droplet-gas interface via diffusion (solid lines) and natural convection (dashed lines) integrated over the droplet-gas interface and during solidification of a 10.1 μL and a 19.8 μL droplet

6. ASYMMETRIC SOLIDIFICATION DURING DROPLET FREEZING IN THE PRESENCE OF A NEIGHBORING DROPLET

By quantitatively describing the transport mechanism that determine the pathways for latent heat dissipation from a droplet freezing on a cooled substrate to its surroundings, the previous chapter showed that a standalone droplet freezing in still air transfers heat to the substrate at a rate that is at least one order of magnitude greater than the heat transferred to the ambient air. These interactions between a standalone freezing droplet and its surroundings can lead to the formation of condensation halos and asymmetric solidification induced by external flows. Furthermore, in a group of many droplets, these interactions are believed to be responsible for inter-droplet frost propagation and the evaporation of supercooled neighboring droplets. This chapter investigates droplet-to-droplet interactions via heat and mass exchange between a freezing droplet and a neighboring droplet, for which asymmetries are observed in the final shape of the frozen droplet. Side-view infrared (IR) thermography measurements of the surface temperature for a pair of freezing droplets, along with three-dimensional numerical simulations of the solidification process, are used to quantify the intensity and nature of these interactions. Two droplet-to-droplet interaction mechanisms causing asymmetric freezing are identified: (1) non-uniform evaporative cooling on the surface of the freezing droplet caused by vapor starvation in the air between the droplets; and (2) a non-uniform thermal resistance at the contact area of the freezing droplet caused by the heat conduction within the neighboring droplet. The combined experimental and numerical results show that the size of the freezing droplet relative to its neighbor can significantly impact the intensity of the interaction between the droplets and, therefore, the degree of asymmetry. A small droplet freezing in the presence of a large droplet, which blocks vapor from freely diffusing to the surface of the small droplet, causes substantial asymmetry in the solidification process. The droplet-to-droplet interactions investigated in this Chapter provide insights into the role of latent heat dissipation during condensation frosting and are a step forward in the development of system-level descriptions of the interactions of many freezing droplets. The material presented in this chapter has been submitted to a journal and is in review for publication.

6.1 Experimental Description

Temperature measurements on the surfaces of a pair of adjacent freezing droplets were acquired using IR thermography in a custom-made experimental facility previously detailed in Section 5.1 for characterization of single-droplet freezing. This section provides a brief description of the test facility and the changes in procedure to enable simultaneous infrared temperature measurements on the surface of pairs of droplets. A schematic diagram of the test facility, which is capable of cooling a substrate below freezing while maintaining uniform background radiation, is provided in Figure 5.1. The experimental facility consists of a black painted (ColorMasterTM Flat Black, Krylon; emissivity of 0.97) aluminum enclosure cooled to sub-ambient temperature using two temperature-controlled thermoelectric stages (CP-031, TE Technology, Inc.). The substrate, which is positioned inside the metallic enclosure, is attached to a sample holder positioned on top of a third cooling device (ZT8, Laird Technologies) which allows cooling the substrate to sub-freezing temperatures. The thermoelectric plate maintains the substrate at a setpoint temperature measured using a 2-wire Pt1000 RTD (PRTF-10-2-100-1/4-12-E-GG, Omega) inserted in the sample holder. The test section is mounted on micrometer stages to allow easy focusing during the infrared measurements.

Smooth hydrophobic silicon substrates prepared as described in Section 4.1.1 were attached to the sample holder using carbon conductive double-sided tape (PELCO Image Tabs). Subsequently, two adjacent droplets were deposited using a pipette. The thermoelectric stages are set to maintain the enclosure at -1.5 °C. After ~15 min, once the entire test section has cooled down, the sample thermoelectric controller is turned on and set to -9.0 °C. After ~4 min, the temperature measured by the RTD reaches a constant value within ± 2% of the setpoint. After ~10 min, ice nucleation occurs within the droplets sequentially.

An IR camera (SC7650, FLIR) is used to record the transient temperature of the surfaces of the droplets at a frame rate of 100 fps. Frames are captured at a spatial resolution of 0.038 ± 0.004 mm/pixel (uncertainty taken as the standard deviation over 8 measurements) using a 50 mm lens (Nyctea, Janos) connected to the camera body with a 38 mm extension tube. The IR camera was calibrated pixel-by-pixel over a range of temperatures from -10 °C to 4.0 °C using a custom-made black body radiator, where the signal intensity of each pixel is fitted as function of the set-point temperature with a fourth-order polynomial equation. Errors in the surface temperature of the droplets caused by background radiation and non-uniform emissivity of the surface were corrected

using the difference between the temperature of the droplet after recalescence and the equilibrium temperature for freezing (0 °C). Further details on the calibration procedure are described in Appendix B.

Simultaneous surface temperature recordings on the surfaces of two droplets are reported in this paper for two cases. A schematic representation of the two cases considered is provided in Figure 6.1. The first case (S) considers a pair of droplets similar in size, with volumes of 2.88 μL (droplet S1) and 2.52 μL (droplet S2), and a center-to-center distance of 2.38 mm. Droplet S1 solidifies while droplet S2 remains supercooled liquid, followed by the solidification of droplet S2. The second case (D) considers a larger 8.98 μL droplet (D1) with a smaller 0.76 μL neighboring droplet (D2) located 2.40 mm away that solidify in the same sequence.

6.2 Numerical Model Description

Numerical simulations of the sequential solidification of a droplet and its neighbor are performed using ANSYS Fluent [89]. with the boundary conditions and droplet volumes the same as the two freezing experiments described in Section 6.1. Figure 6.1 illustrates the two cases that are simulated. Matching the experiments, case S considers the solidification of droplet S1 while droplet S2 remains in liquid state (left panel) followed by the solidification of droplet S2 (right panel). Case D similarly simulates the sequential solidification of droplets D1 and D2. For each case, a three-dimensional model with fixed grid is used to simulate: solidification at the freezing front; heat transfer and fluid flow within the domain of the solidifying droplet; coupled heat and mass transfer at the interface of the solidifying droplet with the gas domain; heat conduction within the solid substrate; and heat and mass transfer in the surrounding gas domain. For the neighboring (solid or liquid) droplet, heat conduction within the droplets as well as coupled heat and mass transfer at the interface with the gas domain are also considered. The computational domain shown with a mesh overlay and key phases, interfaces, and boundaries indicated, is illustrated in Figure 6.2. All the material properties used in the simulation are summarized in Table 5.1. A few assumptions in the implementation of the model were used to reduce the level of complexity of the simulations. The numerical simulations neglect the volume change due to water expansion during freezing, which is known to have negligible influence on the thermal resistance to heat flow in the frozen droplet (as it was demonstrated in Chapter 5). Changes in the volume of the neighboring droplet due to evaporation/condensation are also neglected as they are negligible

compared to the total droplet volumes. Therefore, all the cases use a fixed-grid computational domain, where the shape of the droplets remain unchanged with time. The model description provided in the following sections is modified from Section 6.2 to accommodate for a third spatial dimension and to include the neighboring droplet.

6.2.1 Droplet Domain during Solidification

The enthalpy-porosity formulation [94,95] implemented in the ANSYS Fluent [89]. Solidification/Melting model is used to simulate phase change within the domain of the solidifying droplet. In this formulation for solidification, the liquid of fraction (β) within each cell in the computational domain follows a linear relationship with the temperature (T):

$$\beta = \begin{cases} 0 & T < T_{sol} \\ \dfrac{T - T_{sol}}{T_{liq} - T_{sol}} & T_{lid} < T < T_{sol} \\ 1 & T > T_{lid} \end{cases} \tag{5.1}$$

where T_{sol} and T_{liq} are the liquidus and solidus temperatures for water, and β varies between 0 $\leq \beta \leq$ 1 depending on the fraction of liquid within the cell, with β = 1 indicating that all the water within the cell is in liquid state and β = 0 indicating that the cell is entirely frozen. Any thermophysical property ξ, such as specific heat or thermal conductivity, is expressed in the terms of the liquid fraction as:

$$\xi = \begin{cases} \xi_s & T < T_{sol} \\ (1-\beta)\xi_s + \beta\xi_l & T_{sol} < T < T_{liq} \\ \xi_l & T > T_{lid} \end{cases} \tag{5.2}$$

where ξ_l and ξ_s are the values of the property in the liquid and solid states, respectively. The mass and momentum equations are simplified by assuming that the fluid flow is laminar in the regions where β = 1 and the fluid flow is assumed to be a porous-like fluid flow within the regions of the droplet that are solidified partially (0 < β < 1). Under these assumptions, the continuity and momentum equations are expressed as:

$$\rho_l \nabla \vec{V}_l = S_{m,l} \tag{5.3}$$

$$\rho_l \vec{V}_l \cdot \nabla \vec{V}_l = -\nabla p_l + \mu_l \nabla^2 \vec{V}_l + S_p \tag{5.4}$$

where $\vec{V}$ is fluid velocity, μ_l is the viscosity of water (μ_l = 1.003 x 10 $^{-3}$ kg/m s), $S_{m,l}$ is a mass source term related to the transport across the interface, which is discussed in Section 6.2.3, and S_p is a momentum sink term that pertains to forces created by the displacement of the solidification front. By further assuming that the flow within the mushy region is governed by Darcy's law, S_p is defined as:

$$S_p = \frac{(1-\beta)^2}{\beta^3 + \varepsilon} E_{mushy} \vec{V}_l \tag{5.5}$$

where ε is set equal to 0.001 to prevent division by zero when $\beta \to 0$ and E_{mushy} is a constant that depends on the morphology of the porous media; in this simulation E_{mushy} is set equal to 1×10^5 to control the rate at which the velocity in front of the mushy zone transitions to zero as the solidification front advances.

Using the definition of sensible enthalpy h, the energy transport within the droplet domain is modeled using the energy equation expressed as:

$$\frac{\partial}{\partial t}(\rho h) + \nabla \cdot \left(\rho \vec{V} h\right) = \nabla \cdot (\alpha \nabla h) + S_h + S_{h,l} \tag{5.6}$$

where the energy source term S_h in this equation is derived from the enthalpy formulation of convection-diffusion phase change and is expressed as [96]:

$$S_h = \frac{\partial(\rho \Delta H)}{\partial t} + \nabla \cdot \left(\rho \vec{V} \Delta H\right) \tag{5.7}$$

where the total enthalpy H associated with each cell is calculated as the sum of the sensible enthalpy h and latent heat of the fraction of liquid remaining in the cell ($\Delta H = \beta h_{fs}$), with h_{fs}

being the latent heat of solidification (h_{fs} = 335000 J/kg for water), and the source term $S_{h,l}$ is related to the energy transfer across the interface as described in Section 6.2.3.

6.2.2 Neighboring Droplet, Substrate, and Surrounding Gas Domains

Transient heat transport within the neighboring droplet is modeled assuming that thermophysical properties do not vary within the range of temperatures considered. Under this assumption the energy equation can be expressed as:

$$\frac{\partial T}{\partial t} = \alpha \nabla^2 T \tag{5.8}$$

where α is the thermal diffusivity of water or ice depending on the case considered (i.e., supercooled liquid or frozen solid neighbor). Equation (5.8) is also used to simulate heat transfer within the solid substrate domain, with the thermal diffusivity of silicon given in Table 5.1.

The continuity, momentum, and energy equations for fluid flow in the gas domain are respectively:

$$\nabla\left(\rho_g \vec{V}_g\right) = S_{m,g} \tag{5.9}$$

$$\rho_g \vec{V}_g \cdot \nabla \vec{V}_g = -\nabla p_g + \mu_g \nabla^2 \vec{V}_g + \rho_g \vec{g} \tag{5.10}$$

$$\rho_g c_{p,g} \vec{V}_g \cdot \nabla T = k \nabla^2 T + S_{h,g} \tag{5.11}$$

where $S_{m,g}$ and $S_{h,g}$ are mass and energy terms later described in Section 6.2.3, and μ_g is the viscosity of air (μ_g = 1.789 x 10^{-5} kg/m s). Additionally, it is assumed that the air-vapor mixture in the gas domain follows the ideal gas law; with these simplifications the density of the vapor-air mixture ρ_g can be is expressed as:

$$\rho_g = C_v M_{water} + \left(\frac{p_{atm}}{RT} - C_v\right) M_{air} \tag{5.12}$$

where M_{water} is the molecular weight of water (M_{water} = 0.018 kg/mol), M_{air} is the molecular weight of dry air (M_{water} = 0.029 kg/mol), and the mole concentration of water vapor in the mixture

C_v is solved with the following governing equation for diffusive and convective transport in the gas domain:

$$\vec{V}_g \cdot \nabla C_v - \nabla \cdot \left(D \cdot \nabla C_v \right) = 0 \tag{5.13}$$

In equation (5.13) the temperature-dependent diffusion coefficient D is given by:

$$D(T) = D_{ref} \left(\frac{T}{T_{ref}} \right)^{1.5} \tag{5.14}$$

Additional details on the implementation of equation (5.13) using user-defined scalar (UDS) functions in ANSYS Fluent are described in the Appendix C.

6.2.3 Droplet-Gas Interfaces

Heat and mass transfer through the droplet-gas interfaces of both the solidifying droplet and its neighbor are modeled. The effects of capillary pressure for the millimeter scale droplets can be neglected [67]. The interfacial resistances to condensation and evaporation along the surfaces of the droplets are also neglected because, in presence of non-condensable gases, the resistance to water vapor diffusion dominates over interfacial resistance. Thus, the local saturation pressure of vapor is calculated using the temperature of the droplet-gas interface. At a given interface temperature, the saturation pressure will also depend on the local fraction of ice, as the saturation pressure above of an ice surface is smaller than that above a supercooled liquid surface [97]. To account for the effect of the local fraction of ice on the local saturation pressure, cells on the surface of the droplet-air interface of the solidifying droplet above 0 °C are treated as liquid, whereas cells below 0 °C are treated as solid ice. Expressions for the saturated vapor pressure above ice and supercooled liquid surfaces, as well as further details on the calculation of the content of water inside the air domain, are provided in Appendix C.

Shear stress along both sides of the liquid-gas interface is set as zero, and the vapor flux across the interface, which can be caused by condensation or evaporation, is expressed as:

$$m'' = M_v \left(-D\vec{n} \cdot \nabla C_v + v_n C_v \right) \tag{5.15}$$

where the first term on the right-hand side of the equation is the vapor transport due to mass diffusion, and the second term represents mass convection by Stefan flow. The transport of air across droplet-air interface is set to zero:

$$0 = M_g\left(-D\vec{n}\cdot\nabla\left(C_g - C_v\right) + v_n\left(C_g - C_v\right)\right) \tag{5.16}$$

The velocity of the vapor crossing the interface can therefore be written as:

$$v_n = -\frac{1}{C_g - C_v} D\left(\vec{n}\cdot\nabla C_v\right) \tag{5.17}$$

Equations (5.15) and (5.17), are coupled to find an expression for the mass flux at the interface:

$$m'' = -\frac{M_v D}{1 - C_v/C_g}\left(\vec{n}\cdot\nabla C_v\right) \tag{5.18}$$

where the vapor molar concentration in the gas and the vapor at the interface are respectively calculated as $C_g = p_{atm}/RT_{lv}$ and $C_v = p_{atm}\left(T_{lv}\right)/RT_{lv}$.

The mass transport across the interface is modeled by adding mass sources and sinks to the mesh cells adjacent to either side of the interface, following an analogous procedure as explained in Refs. [98,99]:

$$S_{m,g} = \frac{m''A_{cell}}{V_{cell,g}} \tag{5.19}$$

$$S_{m,l} = -\frac{m''A_{cell}}{V_{cell,l}} \tag{5.20}$$

where A_{cell} is the interface area of the specified cell adjacent to the interface and V_{cell} is the cell volume. Energy transport induced by evaporation and condensation processes are modeled by adding energy sources in the mesh cells adjacent to the interface on either side:

$$S_{h,g} = S_{m,g} h_s \left(T \right) \tag{5.21}$$

$$S_{h,l} = S_{m,l} h_s \left(T \right) + S_{m,l} h_{f,g} \tag{5.22}$$

$$h_s \left(T \right) = c_p \left(T - T_{ref} \right) \tag{5.23}$$

The first terms on the right-hand sides of equations (5.21) and (5.22) represent the sensible heat contributed by the mass source, while the additional term in equation (5.22) accounts for the latent heat adsorbed/released during evaporation/condensation, where $h_{f,g}$ is the latent heat of evaporation ($h_{f,g}$ = 2.497 x10^6 J/kg). The temperature T_{ref} in equation (5.23) is an arbitrary reference temperature implemented in the simulation set equal to 0 °C.

6.2.4 Other Boundary Conditions

The upper boundary of the gas domain is 15 times larger than the droplet radius and the concentration of vapor at this boundary is calculated as:

$$C_v = \frac{RH \, p_{sat}(T_\infty)}{RT_\infty} \tag{5.24}$$

where RH is the relative humidity of the air (RH = 30 %) and T_∞ is the temperature of the air in the far-field (T_∞ = -1.5 °C). The contact line temperature measured from the infrared (IR) experiments is used as a time-dependent boundary condition at each cell in the contact line of the droplet domain. At each time step, a user-defined function (UDFs) is used to update the temperature of each cell in the computational domain with its corresponding infrared temperatures from the experiments. To simulate the cooling power provided by the thermoelectric cooling system, a heat transfer coefficient at the bottom wall of the domain is used as a boundary condition; this heat transfer coefficient is estimated such that the temperature drop across the droplets matches with the experiments. Temperature is continuous across all interior boundaries in the domain, thereby assuming that any contact thermal resistances are negligible.

6.2.5 Initial Conditions

Prior to formation of the freezing front, i.e., the solid ice that progresses from the bottom to the top of the droplet, some fraction of the liquid is frozen as dendrites during the recalescence process (as described alongside discussion of Figure 2.1). The fraction of this ice formed it is often calculated by equating all the latent heat it releases to the sensible heat required to increase the supercooled droplet temperature up to 0 °C via an adiabatic process. In this work, the initial fraction of ice is estimated considering energy losses to the surroundings of the droplet. Therefore, the latent heat released during recalescence is equated to the heat loss to the surroundings in addition to the sensible heating of the formed ice and the remaining liquid up to 0 °C:

$$\frac{\rho_l v x \Delta H}{\Delta t_{rec}} = \frac{\rho_l v x c_{p,s} \Delta T}{\Delta t_{rec}} + \frac{\rho_l v (1-x) c_{p,l} \Delta T}{\Delta t_{rec}} + q_{rec,loss} \tag{5.25}$$

where $x = 1-\beta$ is the fraction of ice, v is the volume of the droplet before recalescence, Δt_{rec} is the duration of recalescence, and $q_{rec,loss}$ is the total heat transferred to the ambient air and to the substrate during recalescence. This expression requires knowledge of Δt_{rec} and $q_{rec,loss}$; the former is determined from the infrared (IR) temperature measurements during recalescence and the latter is estimated by numerically solving the rate of heat transfer between the droplet at 0 °C and its surroundings under transient conditions. The total recalescence time and the results of the numerical simulations performed to quantify the heat losses during recalescence are presented in Section 6.3.1. . The initial fraction of ice calculated using equation (5.25) is used as the initial condition in the transient simulation of solidification. To set the initial fraction of ice in the numerical simulations, the T_{sol} and T_{liq} estimated by using equation (5.1) are inputted as initial conditions to the solidification/melting model.

6.2.6 Numerical Solution Settings

The numerical simulations of the transient heat and mass transfer use the SIMPLE algorithm for pressure-velocity coupling and the first order implicit scheme for time discretization, with a time-step of 0.01 s. The mesh used for the case S (shown in Figure 6.1) has a total of 1,360,000 tetrahedral cells. Similar mesh and domain sizes were employed for case D. The results

of the simulations are checked for mesh and domain size independence. Refinement to a mesh with twice as many cells resulted in less than 2% change in the freezing time. Simulations with a domain size increasing from 15 to 30 times the droplet radius show that the freezing time changed within 1%.

6.3 Results

The infrared (IR) surface temperature recordings during the sequential solidification of a pair of adjacent droplets are used to investigate the pathways for heat transfer between the droplets. In Section 6.3.1, these measurements are used to track the evolution of the crystallization process and to determine the fraction of ice formed during recalescence. In Section 6.3.2, the model is benchmarked against these measurements, such that in Section 6.3.3, the simulated temperature, vapor mass fraction, and velocity fields can be used to qualitatively asses the different transport mechanisms at play. Lastly, a quantitative description of each heat transport pathway between a solidifying droplet and its neighbor is provided in Section 6.3.4.

6.3.1 Droplet-To-Droplet Interactions During Recalescence

A sequence of side-view temperature maps on the surfaces of droplets S1 and S2 are shown in Figure 6.3 during the recalescence of droplet S1. Prior recalescence at t = 0 s, both droplets are supercooled liquid with an average surface temperature of ~-8.5 °C and have a slight temperature drop (~ 0.5 °C) across the droplet height due to conduction to the substrate. At the onset of the recalescence, at observed at t ~ 0.01 s, ice crystals heterogeneously nucleate near the base of droplet S1 and begin to propagate upward. By t = 0.02 s, a front of ice crystals can clearly be identified as the boundary between the two well-defined temperature regions with uniform temperature; in front of the crystallization front the temperature of the droplet remains at ~-8.5 °C , whereas the temperature within the regions where crystallization has already occurred is close to the equilibrium freezing temperature of 0.0 °C . Subsequently, at t = 0.03 s, the crystallization front has propagated throughout the entire surface of droplet S1, marking the completion of recalescence. The dynamics of the crystallization process observed in the sequence of images in Figure 6.3 agrees with the decelerating propagation of the crystallization front previously reported in the literature [103] and demonstrated in Section 5.3.1; the crystallization front advances faster

at the beginning of the recalescence process and then reduces as it progresses toward the top of the droplet.

After droplet S1 has completed recalescence, latent heat released due to crystallization (the portion that is not invested into increasing the sensible temperature of droplet S1) locally heats the environment causing a slight increase of ~0.2 °C in the average surface temperature of droplet S2. Although it is often assumed that there is not enough time for heat to dissipate to the environment during the rapid crystallization process, and therefore recalescence occurs adiabatically, comparing to the timescale for heat diffusion from the droplet to its surroundings reveals that some of the heat released should dissipate to the environment. For the experiments considered in this paper, some heat can still diffuse to the substrate even though the maximum recalescence time observed (~ 0.06 s for droplet D1) is slightly smaller than the timescale for heat diffusion in the substrate given by $\tau_\alpha = l^2/\alpha_s \approx 0.12$ s , where α_s = 8.93 × 10^{-5} m^2/s is the thermal diffusivity of the silicon substrate and $l = 2R_{D1}$ = 3.15 × 10^{-3} m is the length scale for heat diffusion in the substrate, and R_{D1} is the radius of droplet D1. Therefore, recalescence cannot be assumed to occur adiabatically and a fraction of the latent heat released to the substrate should manifest as an increase in the temperature of the neighboring droplet.

The numerical model described in Section 6.2.5 is used to estimate the heat transferred from a droplet with uniform temperature equal to 0 °C to its environment. The total heat lost to the substrate through the base of the droplet and to the ambient air through the droplet-gas interface is summarized for all of the droplet recalescence events in Table 6.1, along with their respective time to complete recalescence and fraction of ice crystalized calculated from equation (5.25). The results indicate that ~75% of the heat released during recalescence is lost to the ambient (substrate and air), whereas only 25% sensibly heats the droplet up to 0 °C. Because recalescence occurs much faster than the time-scale for heat diffusion to the neighboring, only ~0.1% of the heat released by the droplet undergoing recalescence increases the temperature of the neighboring droplet. The amount of heat lost to the ambient, the fraction of ice formed, and the duration of the recalescence process all increase with the size of the droplet; the smallest droplet D2 released 10 times less heat than droplet D1.

6.3.2 Droplet Surface Temperature Distributions during Solidification

The measured temperature maps on the surfaces of a solidifying droplet and its neighbor are used to benchmark the numerical simulations. A sequence of side-view surface temperature maps during the sequential solidification of droplets S1 and S2 with similar volume are shown in Figure 6.4. In the experimental results shown on the left, a vertical line is drawn passing through the centerline of the droplets (based on their shape prior to recalescence) as a reference from which any asymmetry in the final shape of the droplet can be detected. Overall, the numerical predictions shown on the right qualitatively capture all key characteristics of the experimental temperature distributions, with a few differences discussed in detail below.

At the onset of the solidification of droplet S1 (just after recalescence), droplet S2 is in a supercooled liquid state at an average temperature slightly above that of the substrate, while the temperature of droplet S1 is uniform and close to 0 °C. At intermediate times between recalescence and complete solidification, as at t = 3.03 s in Figure 6.4, the temperature distribution in the solidifying droplet has two well-defined regions separated by the solidification front. A region above the solidification front remains near T_{eq} and a solid region behind the solidification front has temperature isotherms that decreases in the direction towards the substrate. As this solidification front progresses, the water-ice mixture above the front is pushed upward, increasing the height of the droplet and leading to a frozen droplet with a conically-shaped apex (which is not present in the simulation results because volume changes during solidification are neglected). Although, the numerical simulations reproduce the temperature distributions observed in the experiments, the location of solidification front obtained in the numerical simulations lags behind the experimental results at any given time. This results in slightly longer prediction solidification time of t = 6.22 s in the numerical simulations compared to t = 6.03 s during the experiment. The relative error in the freezing time estimated for all the cases considered in the numerical simulations was below 5%.

In contrast to the symmetrical solidification of individual droplets in Chapter 5, , the presence of a neighboring droplet results in an asymmetric progression of the solidification front with respect to the centerline of the droplet. Close inspection of the temperature contours in Figure 6.4 reveals that the temperature gradient is steeper in the solid region on the side of the solidifying droplet nearer to its neighbor. The freezing front advances more quickly on this side of the droplet as the latent heat released at the solidification front can be dissipated at a higher rate, which results

in the asymmetric progression of the front. This asymmetric propagation of the freezing front shifts the conical tip of the frozen droplet in a direction away from its neighbor. This shift is very smaller in the solidification of droplet S1, only 0.05 mm to the left of its initial centerline, whereas the asymmetrical progression of the freezing front is slightly more prominent during the solidification of droplet S2, leading to a 0.09 mm shift in its tip to the right.

The thermography data for the solidification of the differing sized droplets D1 and D2, shown in Figure 6.5, provide clearer evidence of the asymmetrical freezing that occurs in the presence of a neighboring droplet. The interactions between differing sized droplets leads to more asymmetric freezing behavior compared to the similarly sized droplets. From the sequence of temperature maps shown during the solidification of droplet D1 in Figure 6.5, it can be observed that the freezing front progresses more rapidly on the side closer to the neighboring droplet D2, which results in asymmetrical solidification of droplet D1 with a top shifted 0.14 mm from the centerline. Subsequent solidification of droplet D2 also occurs asymmetrically, with an event more pronounced shift of 0.18 mm away from the centerline. In comparison with case S (droplets with similar size), the asymmetry in the freezing front propagation is more severe for case D. This suggests that the relative size of droplet pairs can have a strong effect on the interactions between the solidifying droplet and its neighbor.

6.3.3 Droplet-To-Droplet Interaction Mechanisms

This section considers the simulated temperature and liquid fraction distributions within the droplets during their sequential solidification, along with the water vapor mass fraction and the velocity vector field in the surrounding gas domain, to identify the heat and mass transport mechanisms that cause asymmetrical. Case D is presented in detail because the interactions are more apparent. Figure 6.6 shows the time-sequence of simulated contour plots during the solidification of the larger droplet (droplet D1), whereas Figure 6.7 shows the same set of contour plots during solidification of the smaller droplet (droplet D2). For both droplets, the temperature contours suggest two primary paths for heat exchange between the droplets; (1) heat conduction through the substrate and (2) heat transfer through the air domain. For each these two pathways, there are several mechanisms driving heat exchange between the droplets. Heat conduction in the substrate occurs due to the high local temperature at the base of the solidifying droplet, from which heat can either flow directly through the bottom of the substrate or to the base area of the

neighboring droplet at a lower temperature. Heat transfer between the droplets through the air domain occurs due to the temperature and concentration differences between interfaces of the droplets and the far field boundary, which drive coupled heat diffusion, natural convection, and evaporative cooling at the interfaces of the droplets. The influence of each of these transport mechanisms on the on the thermal coupling between the neighboring droplets during solidification is assessed in the following sections.

6.3.3.1 Heat Diffusion

After recalescence of droplet D1 at t = 0.06 s in Figure 6.6 (a) , the latent heat released increases the temperature of the substrate and the air near the droplet. The temperature difference between the droplet and the lower wall of the substrate drives heat away to the cooling system and spreads the heat laterally. Although the temperature gradient formed within the substrate reaches the region of the substrate below the neighboring droplet, the temperature rise within the neighboring droplet D2 is barely appreciable from the contour plots. At t = 8.06 s, the horizontal temperature isotherms within droplet D1 indicate that the latent heat released at the solidification front is conducted through the part of the droplet that has solidified to the substrate; there is also a significant increase in the temperature of the air around the droplet. Some of this heat is transferred to the neighboring droplet through the air and substrate domains, which leads to a slight increase in the temperature (~1.5 °C) of droplet D2 on its side closer to droplet D1. The liquid-ice mixture region of the droplet ahead of the solidification front that remains near T_{eq} is primarily responsible for increasing the temperature of the air above the droplet by diffusion. As the freezing front advances towards the top of droplet D1, the thermal resistance of the solid part of the droplet increases, reducing the temperature at its base and consequently the heat transfer from droplet D1 to the substrate. After complete solidification, the only a small temperature gradient remains in the droplet due to the temperature difference between the far field and lower wall of the substrate.

During droplet D2 solidification, the sequence of temperature contour plots in Figure 6.7 (a) show the same mechanisms for heat diffusion observed during the solidification of droplet D1. In this case, the latent heat released by droplet D2 increases the temperature of droplet D1 at t = 1.52 s by ~ 0.7 °C in the regions that are closer to D2.

6.3.3.2 Heat Transport in the Gas Domain

Natural convection in the air domain is driven by the temperature difference between the droplet-gas interface of the solidifying droplet and its surroundings. Differences in air density caused by the temperature field induce flow above the freezing droplet, with characteristics that depend on the stage of the solidification process. At t =0.06 s, just after recalescence, the velocity vector field shown in Figure 6.6 (b) corresponds to the airflow expected for natural convection above a *finite* cooled substrate (air flowing downwards from far field toward the substrate to replace cold air that moves laterally), with an average velocity of 0.3 mm/s in the region above the droplet. At later times between recalescence and complete solidification (e.g., t = 8.06 s in Figure 6.6 (b)) , a density gradient created by heating of the air above the droplet D1 drives and upward flow with an average velocity of about 3.0 mm/s that draws in cooler air flow from the sides of the droplet . This natural convection current provides additional cooling at the interface of droplet D1, which results in additional phase change in the liquid-ice mixture region at the top of droplet above the solidification front (as can be observed from the liquid fraction contours plotted within the droplet in Figure 6.6 (b)) On the surface of droplet D2, natural convection cooling competes with heat diffusing from droplet D1. After droplet D1 has solidified at t = 15.06 s, the air flows from the far field towards the substrate at an average velocity of 0.6 mm/s.

Relative to the natural convection-induced cooling caused by the solidification of droplet D1, the solidification of droplet D2 has a smaller effect on the surrounding velocity field. The velocity vectors are shown in Figure 6.7 (b) during the solidification of droplet D2. At the start and the end of the solidification process, the velocity fields resemble typical natural convection profile over a finite cooled substrate, just as during the solidification of droplet D1. At an intermediate step during the solidification of droplet D2, such as at t = 1.52 s, heating of the air above the droplet induces a small recirculation zone, but only on the right side of droplet D2; the additional cooling by this convection causes additional solidification in the top of the droplet.

6.3.3.3 Mass Transport in the Gas Domain and Evaporative Cooling at the Gas-Droplet Interface

A time-sequence of mass vapor fraction contour plots in the gas domain is shown in Figure 6.6 (c) for the solidification of droplet D1. The difference between the water vapor concentration in the ambient and droplet-gas interfaces of the droplets drives vapor transport via combined

diffusion and natural convection. At the onset of the solidification process, the concentration of water vapor on the surface of the droplet D1 is uniform and equal to 3.7×10^{-3}. This relatively high concentration of water vapor in the vicinity of droplet D1 also increases the concentration of vapor around droplet D2. The gradients of vapor mass fraction indicate that most of the surface area of the droplets lose vapor to the ambient, but a small section of droplet D1 loses vapor to droplet D2 through the region between the droplets. After the solidification process is complete, the interfaces of both droplets are cooled down to a temperature close to the temperature of the substrate. A small evaporative flux from droplet D2 to droplet D1 is caused by the difference in the saturation pressure above ice (droplet D1) being smaller than the saturation pressure above a liquid surface (droplet D2) at the same temperature.

During the solidification of droplet D2 (Figure 6.7 (b)), droplet D1 enhances evaporation on regions of the surface of droplet D2 that are closer to droplet D2e Throughout droplet D2 solidification, in the region above the solidification front that is facing droplet D2, the concentration of water vapor decreases from 3.7×10^{-3} to the mass fraction of water above droplet D1, 1.8×10^{-3}. Whereas in regions around droplet D2 that are away from droplet D1, the water vapor concentration reduces gradually to the far-field water vapor concentration. The additional cooling created by this non-uniform evaporation, contributes to additional solidification on the regions of droplet D2 that are closer to D1, as can be observed from the liquid fraction contours at $t = 1.52$ s shown in Figure 6.7 (b). These differences in the behavior of droplet D1 and D2 reveal how the relative droplet size can affect the contribution of evaporative cooling to the asymmetrical solidification observed during the experiments. Namely, even though droplet D1 solidification is accompanied by stronger evaporative cooling than droplet D2 solidification, the non-uniform solidification induced by evaporative cooling is stronger for droplet D2.

6.3.4 Quantifying the Interactions Between a Freezing Droplet and its Neighbor

The results of the numerical simulations are used to quantitatively determine the fraction of latent heat released during droplet freezing that is transferred to its neighboring droplet, as well as the relative strength of the mechanisms that contribute to the asymmetrical solidification in adjacent droplets. Figure 6.8 plots the total heat transfer rates integrated across the base contact area with the substrate and separately across the droplet-gas interfaces of droplets D1 and D2 at each time-step during the solidification of droplet D1(case D). The total heat transfer rate across

the droplet-gas interfaces of each droplet includes combined heat diffusion and natural convection, as well as evaporation cooling. As shown in Figure 6.8 (a), at the onset of the solidification of droplet D1, the rate at which latent heat is transferred to the substrate and gas is maximum and decreases as the solidification front progresses. As it was discussed in Sections 6.3.3, heat diffusion to the solid substrate during the solidification of droplet D1 is limited by the thermal resistance of the solid part of the droplet behind the solidification front, which increases as the solidification front progresses towards the top of the droplet. Meanwhile, heat transfer across the droplet interface reduces (not visible in Figure 6.8 due to the scale of vertical axis) due to the combined effects of: (1) heat and mass diffusion becoming confined to the upper section of the droplet surface ahead of the solidification front where the temperature is higher and (2) a reduction of the convective heat and mass transport that results from the decreases in the velocity of the dry air drawn in from the sides of the droplet. Throughout the solidification process of droplet D1, the heat transfer lost to the substrate is at least an order of magnitude greater than the heat transfer through the interface of the droplet. A very small fraction of ~0.02% of the heat lost from droplet D1 is ultimately transferred to droplet D2. As shown in Figure 6.8 (b), the maximum rate of heat transfer to droplet D2 through the substrate (~0.5 mW) occurs at the onset of droplet D1 solidification and decreases the solidification process in droplet D1 progresses. At t = 2 s, the latent heat transferred from droplet D1 is smaller than the heat lost from the base of droplet D2 to the cooling system, leading to a negative heat transfer rate (i.e., net outflow from droplet D2) and decreasing the temperature at the base of droplet D2. Similarly, the interface of D2 is heated at the onset of solidification with about 0.1 mW of power, and rapidly decreases as the solidification front of droplet D2 advances.

The same integrated heat transfer rates through the droplet bases and interfaces during the solidification of droplet D2 are shown in Figure 6.9. Generally, all of the trends and mechanisms are similar to those shown in Figure 6.8, so they are not repeated here. Because droplet D2 is ~11 times smaller than droplet D1, the latent heat of solidification released by droplet D2 is much smaller than droplet D1. Consequently, the rate of heat transfer at the base of droplet D2 is 5 times smaller than during the solidification of D1 shown in Figure 6.8 (a). However, the fraction of heat lost from droplet D2 to the neighboring droplet D1 is larger; approximately 6.6% of the latent heat released by droplet D2 is transferred to droplet D1. This demonstrates that a larger droplet has a greater impact on the solidification of smaller neighboring droplet and vice versa.

The heat transfer rates presented in Figure 6.8 and Figure 6.9 allow determination of the amounts of heat transferred to the neighboring droplet through each pathway. For solidification of droplets D1 and D2, the Sankey diagram in Figure 6.10 summarize the percentages of the total latent heat released during recalescence through each of the heat transfer pathways to the neighboring droplet. During the recalescence of both droplets D1 and D2, ~9% of the latent available is invested into sensible heating of the droplets up to T_{eq}. Meanwhile, ~20-30 % of the heat is lost to the substrate and a very small fraction to the ambient air. During the solidification process of droplet D1, a total of 2.6% of the latent heat available is lost to the ambient air (1.4% via combined heat diffusion and natural convection, and 1.2 % via evaporative cooling); the remaining 68.6% of the heat conducts away through the substrate. Ultimately, only 0.7% of the total latent heat is transferred to the neighboring droplet, with most of that heat being transferred through the substrate (0.5%) versus through the air (0.2%). In comparison with droplet D1, during the freezing of droplet D2, a larger percentage of the heat is transfer to its neighbor. A total 6.6% of the latent heat released by droplet D2 is transferred to droplet D1, with close to a 1:1 split between the amount transferred through the substrate and air domains. As it was shown in Section 6.3.3, asymmetric heat exchange through the substrate and ambient air leads to non-uniform rates of solidification within a freezing droplet, with smaller droplets freezing in the neighborhood of a larger droplet having a more drastic asymmetry. Here, the quantitative delineation between the heat transport pathways confirms how smaller droplets have stronger interactions with their large neighbors.

6.4 Conclusion

This Chapter illustrates the pathways of heat and mass exchange between a freezing droplet and an adjacent neighboring droplet, which lead to asymmetrical solidification. Infrared (IR) thermography measurements of the surface temperature of the freezing droplet and its neighbor, along with high-fidelity numerical simulations, are used to calculate the amount of heat transferred to the neighboring droplet through the substrate and ambient air. The modeling approach presented in this paper uses the IR temperature data at the contact line of the droplet as a boundary condition and provides a full description of the driving mechanisms for heat and mass exchange between the freezing droplet, substrate, ambient air, and neighboring droplet. The results of the numerical

simulations are benchmarked against the experiments, showing good agreement in the evolution of the surface temperature maps of the droplets.

The infrared temperature maps on the surfaces of the droplets indicate that non-uniform heat transfer at the solidification front of a freezing droplet leads to an asymmetrical solidification with the conical tip of the final frozen droplet shape shifted away from its neighbor. The impact of droplet size on the relative severity of the asymmetry was evaluated by solidifying pairs of droplets that were similar in size (~1:1 ratio) and dissimilar in size (~10:1 ratio). The results show that asymmetries in the solidification process intensify when the size of one droplet is small relative to its neighbor.

The heat transfer rates through the base and interface of the droplets were numerically integrated from the simulations to quantify the amount of heat exchange between the droplets. The simulation results indicate that less than 1% of the latent heat released by a large droplet is transferred to a smaller neighbor, whereas the smaller neighbor will transfer ~6% of the latent heat released to the larger droplet. The transient evolution of temperature and liquid fraction within the droplets obtained from the numerical simulations, as well as the vapor mass fraction and velocity fields in the ambient air, reveal that the presence of a neighboring droplet causes non-uniform cooling at the droplet-gas interface and non-uniform heat spreading into the substrate, which are the mechanisms responsible for the asymmetrical solidification.

Table 6.1. Summary of test results for the interactions between neighboring droplets during recalescence of droplets S1, S2, D1 and D2.

	S1	**S2**	**D1**	**D2**
Droplet volume, v (μL)	2.88	2.52	8.8	0.8
Recalescence time, Δt_{rec} (s)	0.03	0.03	0.06	0.02
Latent heat released during recalescence (J)	0.35	0.3	0.85	0.1
Sensible heat (J)	0.09	0.08	0.27	0.02
Heat loss to the ambient(J)	0.27	0.23	0.61	0.08
Initial fraction of ice, x	0.36	0.35	0.28	0.39
Heat transferred to neighboring droplet ($x10^{-3}$ J)	0.36	0.25	0.46	0.28

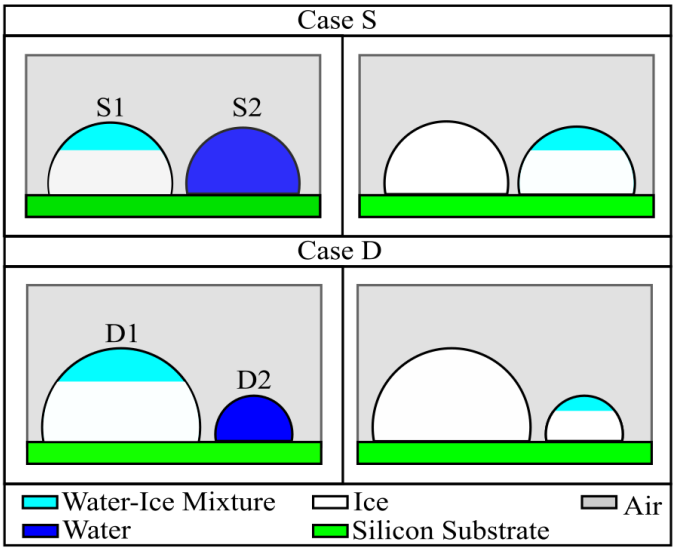

Figure 6.1. Schematic representation of the two-droplet sequential solidification cases examined in this paper. Case (S) considers a pair of droplets that are similar in size, with volumes 2.88 μL (droplet S1) and 2.52 μL (droplet S2). The panel on the left illustrates the solidification of droplet S1 while droplet S2 remains supercooled liquid, followed by the solidification of droplet S2 illustrated in the right panel. Case (D) considers a larger 8.98 μL droplet (D1) with a smaller 0.76 μL neighboring droplet (D2) that solidify in the same sequence.

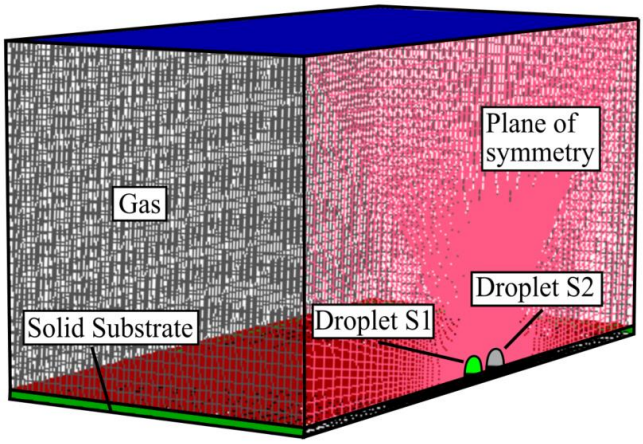

(a)

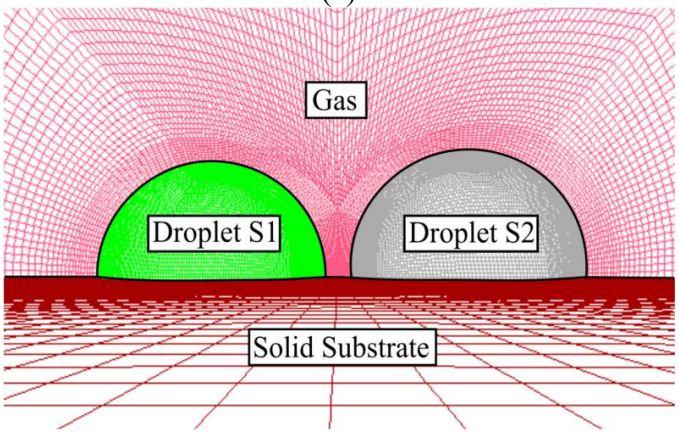

(b)

Figure 6.2. Numerical solution domain with mesh overlay showing the (a) half symmetric domain along with (b) details near the droplets resting on the surface from a perspective view along the substrate.

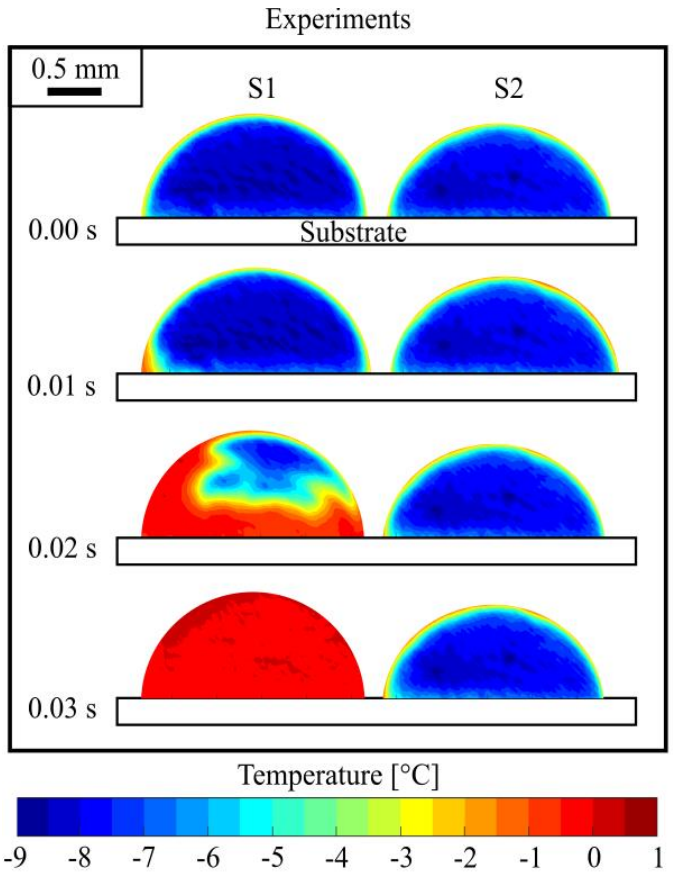

Figure 6.3. Sequence of experimentally measured side-view infrared temperature distributions on the surfaces of droplet S1 and its neighboring droplet S2. In this sequence of images, droplet S1 is undergoing recalescence while droplet S2 remains in a supercooled liquid state. The silicon substrate size and thickness is not drawn to scale.

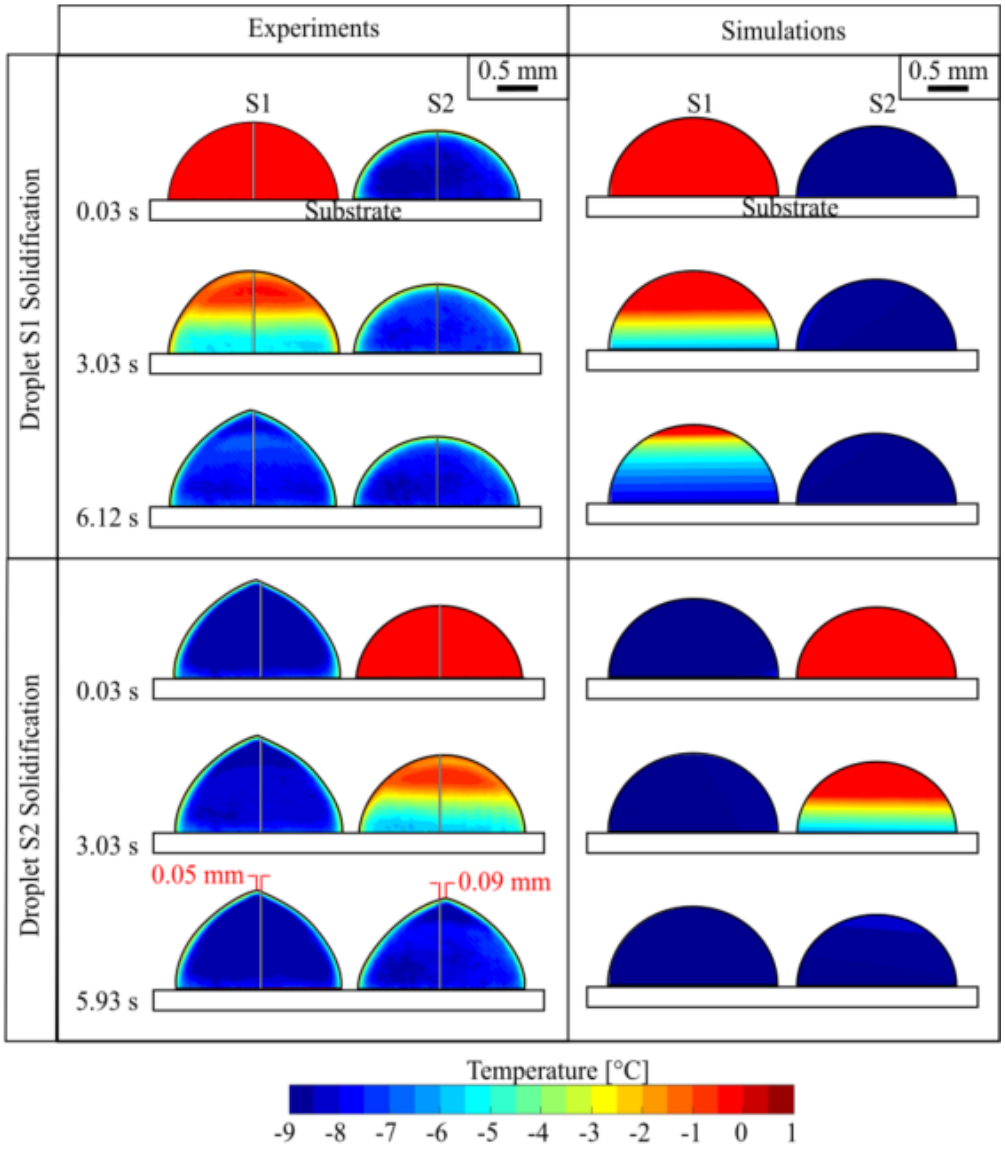

Figure 6.4. Time sequence of the surface temperature maps during the sequential solidification of similarly sized droplets S1 and S2. The experimental data are shown in the left column and the simulation predictions in the right column. The top row shows the solidification of droplet S1 (where droplet S2 is subcooled liquid) and the bottom row the subsequent solidification of droplet S2 (where droplet S1 is frozen). The experimental IR thermography data is cropped around the droplets to remove the immaterial background data. The vertical lines overlapping the experimental images pass through the centerline of each droplet based on their pre-recalescence shape.

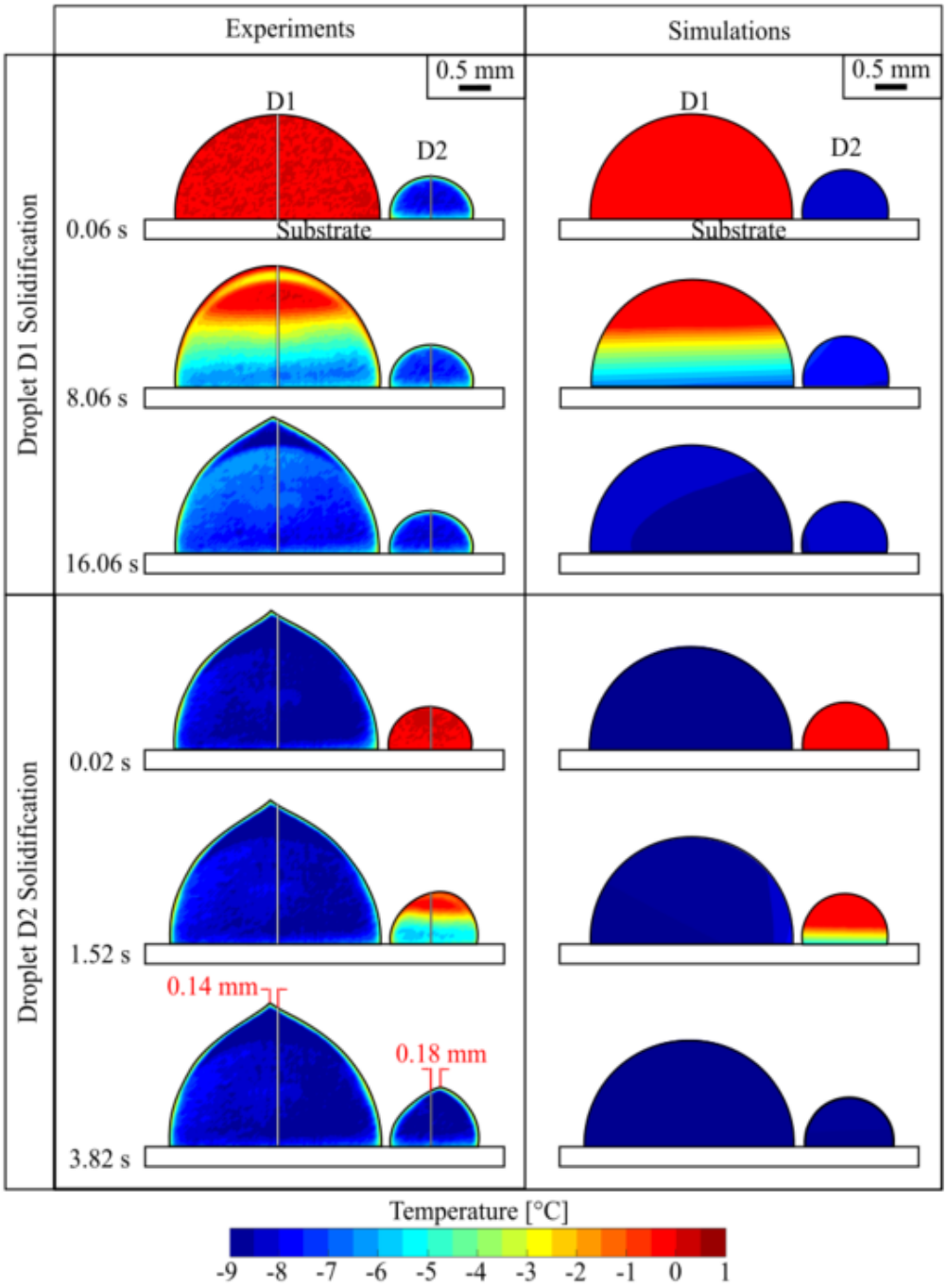

Figure 6.5. Time sequence of the surface temperature maps during the sequential solidification of differently sized dropletsD1 and D2. The experimental data are shown in the left column and the simulation predictions in the right column. The top row shows the solidification of droplet D1 (where droplet D2 is subcooled liquid) and the bottom row the subsequent solidification of droplet D2 (where droplet D1 is frozen). The experimental IR thermography data is cropped around the droplets to remove the immaterial background data. The vertical lines overlapping the experimental images pass through the centerline of each droplet based on their pre-recalescence shape.

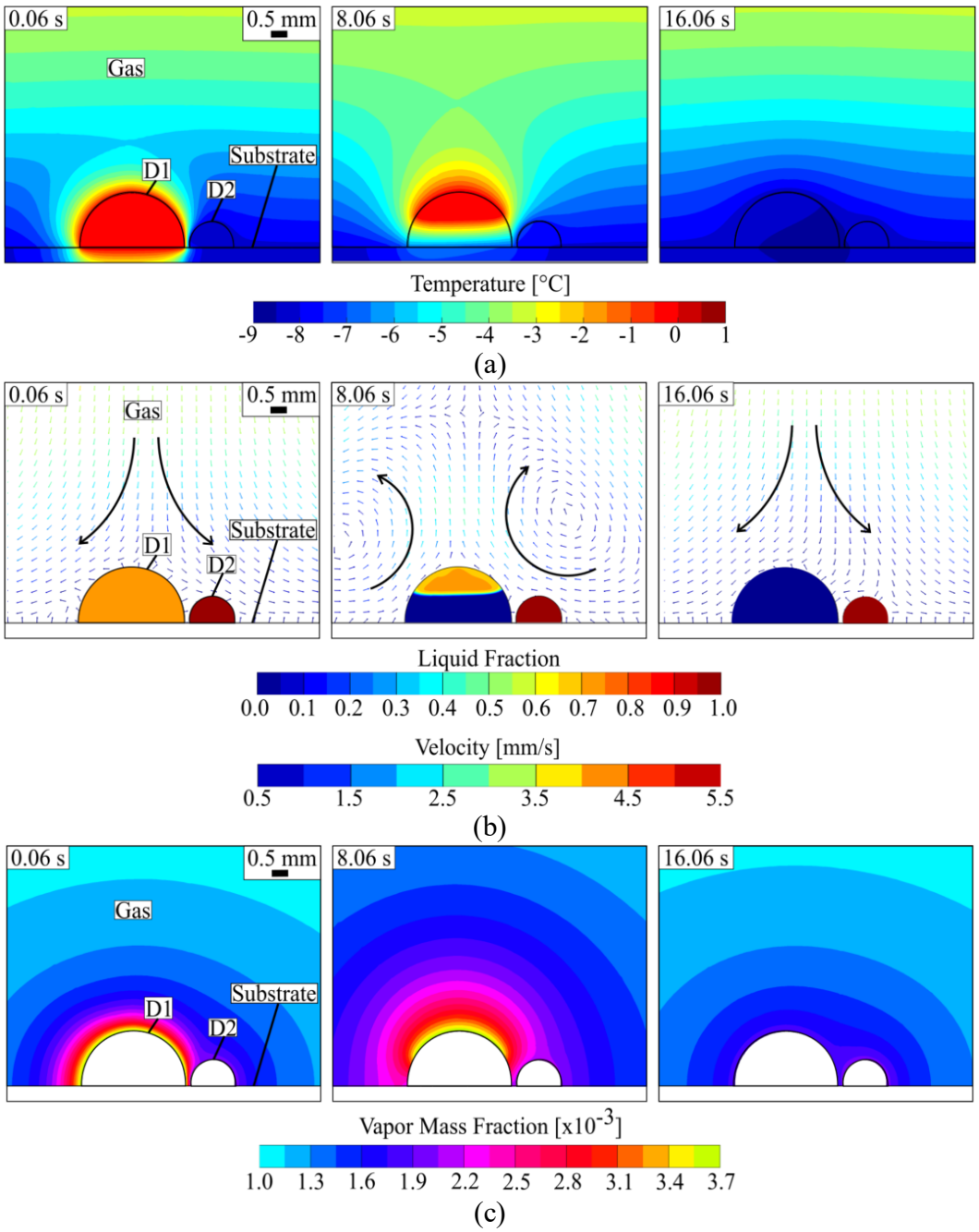

Figure 6.6. Simulated time sequence of (a) temperature contour plots, (b) liquid fraction contour plots (within the droplets) and velocity vectors (in the gas domain), and (c) vapor mass fraction contour plots (in the gas domain) for the solidification of droplet D1.

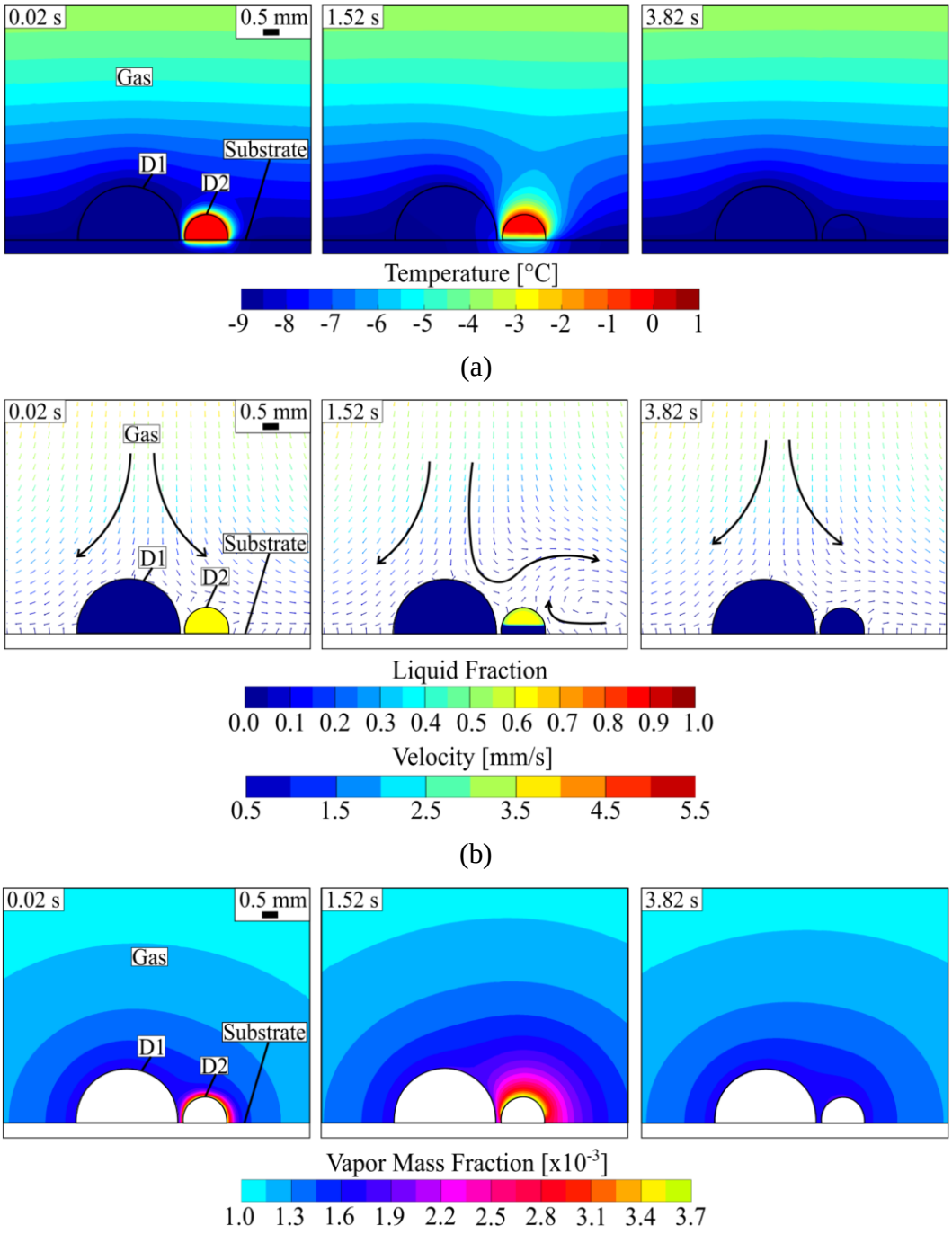

Figure 6.7. Simulated time sequence of (a) temperature contour plots, (b) liquid fraction contour plots (within the droplets) and velocity vectors (in the gas domain), and (c) vapor mass fraction contour plots (in the gas domain) for the solidification of droplet D2.

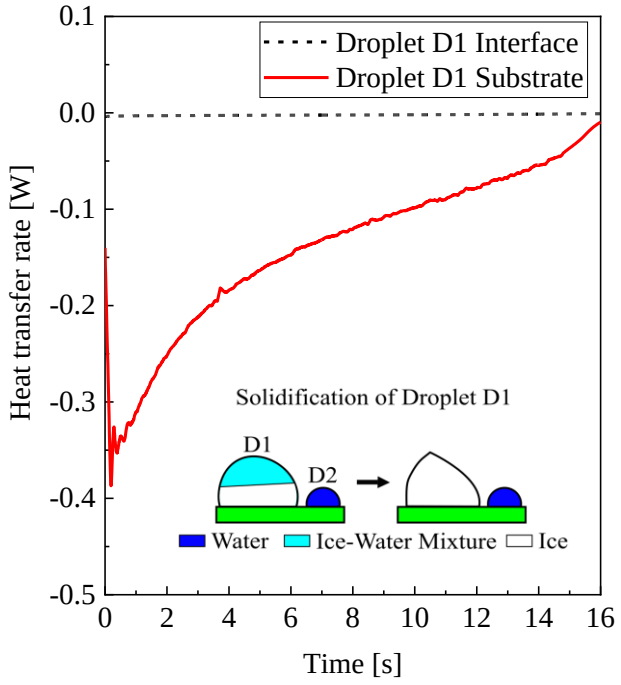

(a)

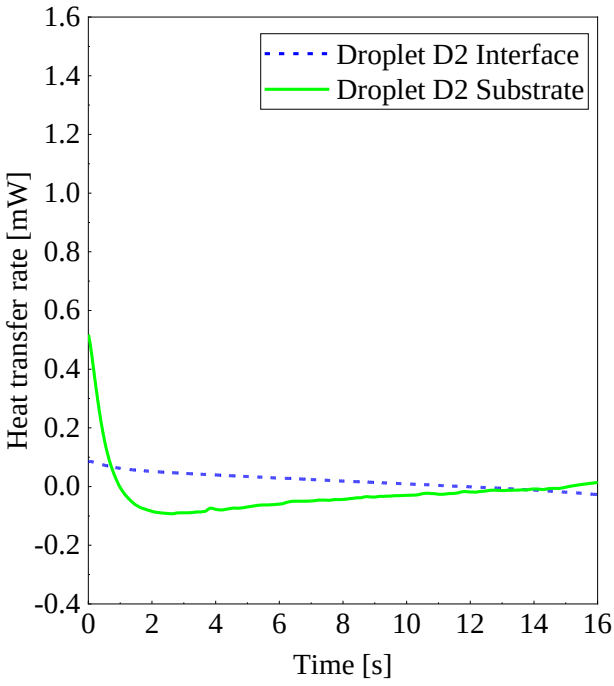

(b)

Figure 6.8. Heat transfer rate across the droplet base contact area with the substrate (solid lines) and through the droplet-gas interface (dashed lines) of droplets (a) D1 and (b) D2, during the solidification of droplet D1.

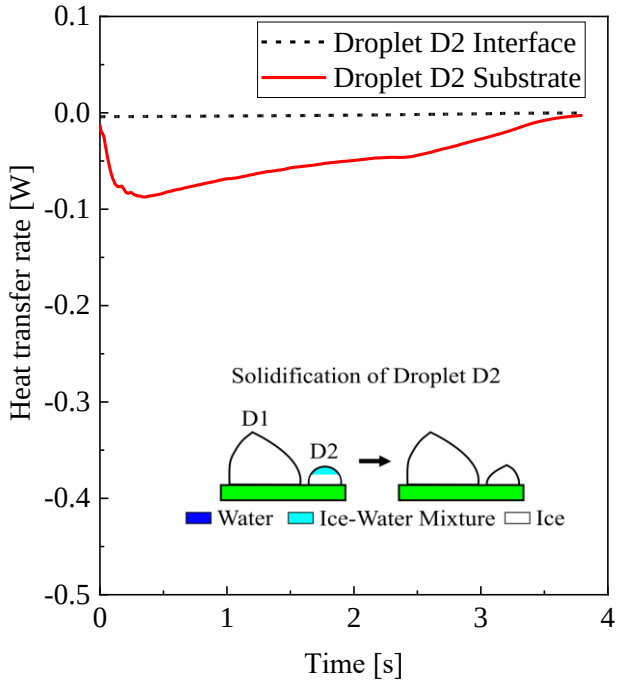

(a)

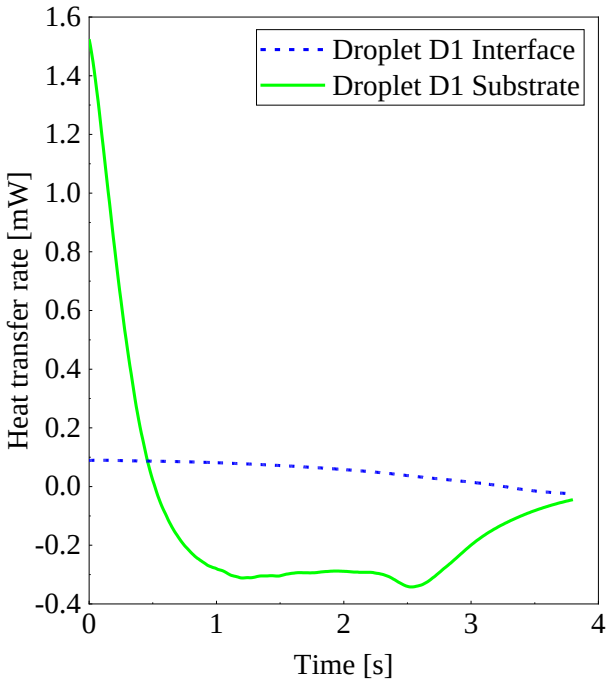

(b)

Figure 6.9. Heat transfer rate across the droplet contact area with the substrate (solid lines) and through the droplet-gas interface (dashed lines) of droplet (a) D2 and (b) D1, during the solidification of droplet D2.

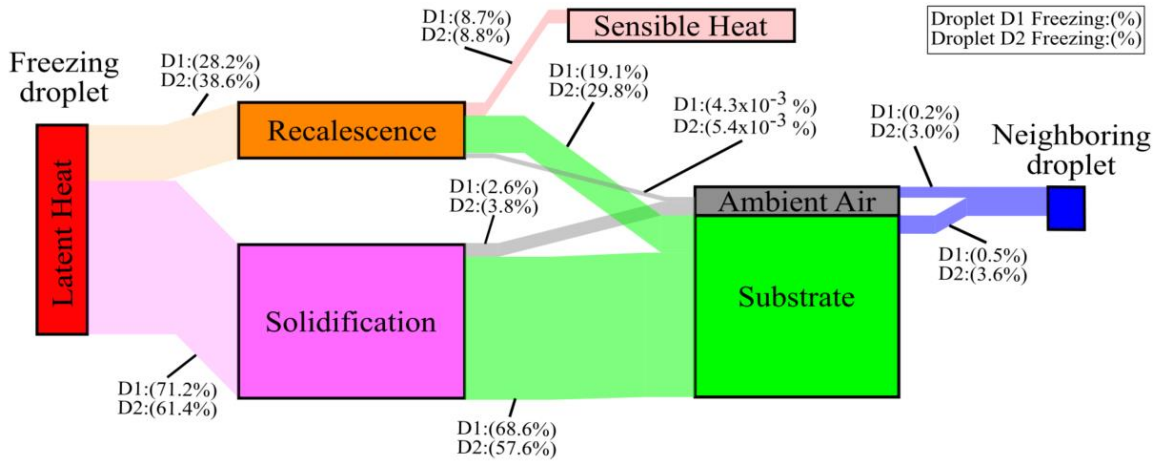

Figure 6.10. Heat transfer rate across the droplet contact area with the substrate (solid lines) and through the droplet-gas interface (dashed lines) of droplet (a) D2 and (b) D1, during the solidification of droplet D2.

7. CONCLUSIONS AND FUTURE WORK

The main outcome of this dissertation is a better understanding of the of the heat and mass transfer mechanism that govern dropwise condensation and freezing, in particular the droplet-to-droplet interactions that are critical to the prediction of behavior in practical scenarios having many droplets on the surface. The research developed a system-level description of the local interactions between a condensing droplet and its neighbors, as well as a detailed description of the interactions between a freezing droplet, its environment, and its neighboring droplet. This chapter summarizes the key research outcomes of the present document, and subsequently a few paths for future research are proposed.

7.1 Conclusions

In Chapter 3, a methodology to calculate the instantaneous condensation rates of individual droplets during diffusion-driven dropwise condensation from a controlled environment is benchmarked against three-dimensional simulations of the diffusion equation. This methodology uses the location and size of each droplet, along with few ambient conditions (e.g., substrate temperature, ambient air temperature and relative humidity) to compute the water vapor distribution in the ambient air and the corresponding condensation rate at the surface of each droplet. The modeling approach was used to demonstrate:

- A closed-form solution for the condensation rate of an individual droplet can be derived by superposing the solution to the diffusion equation for each individual droplet treated as a point sink
- This point sink superposition method (PSSM) accurately predicts condensation rates for system of several droplets obtained from numerical simulations
- The modeling approach captures the interactions between all the droplets on the surface, accounting for the spacing between the droplets and their relative size
- For a simplified scenario containing two neighboring condensing droplets, the rates of growth are studied as a function of the inter-droplet distance and the relative droplet size.

- For representative systems of condensing droplets on a surface, the total condensation rates predicted by the reduced-order model match numerical simulations to within 15%. The results show that assuming droplets grow as an equivalent film or in a completely isolated manner can severely overpredict condensation rates.

In Chapter 4, the PSSM is benchmarked against experimental condensation rates of individual droplets, within a system of many droplets on a substrate during vapor-diffusion-driven dropwise condensation from humid air. The PSSM is also compared with previous models reported in the literature. The results of Chapter 4 showed that:

- The PSSM accurately predicts the experimental growth rates of individual droplets, and the total condensation rate of groups of droplets.
- Assuming that droplets grow completely isolated from one another severely overpredicts the measured condensation rates.
- A large number of interacting droplets, over a length scale of the substrate much larger than the separation distance between droplets, must be considered to accurately predict the experiments.
- Even though the interaction between nearest neighboring droplets is the strongest, only including the such neighboring droplets in the close vicinity still severely overpredicts condensation rate of an individual within the system.
- Relative droplet size effects on condensation rates are more prominent at later stages of the growth, when the size distribution of droplet is broader.

Chapters 5 and 6 addressed key questions regarding the mechanisms during droplet freezing, that are instrumental to developing a system-level description of condensation freezing, such as the modeling approach for dropwise condensation validated in Chapters 3 and 4. A complete description of the mechanism driving the heat and mass exchange between a freezing droplet and its environment is presented in Chapter 5. Infrared (IR) temperature measurements on the surface of a freezing droplet, as well as a numerical simulation benchmarked with a direct comparison of the temperature maps, are used to quantitatively describe the transport mechanisms that determine the pathways for latent heat dissipation from a droplet freezing on a cooled substrate to its surroundings. From the results of infrared (IR) thermography freezing experiments and the 2D axisymmetric simulations of the solidification process it was concluded that:

- By reducing ambient radiation during sub-freezing infrared (IR) measurements, temperature maps with high spatial resolution can be used to track the evolution of the crystallization front during droplet recalescence, as well as to resolve the temperature gradients at the surface of solidifying microliter droplets.
- Good agreement with the IR temperature maps of the surface of a solidifying droplet can be achieved through numerical simulations of the solidification process that considers heat losses during recalescence and a time-dependent contact line temperature as boundary condition.
- The heat transfer rate to the substrate of the droplet is at least one order of magnitude greater than the heat transferred to the ambient air.
- Evaporative cooling only accounts for a small percentage of the total heat exchange at the droplet-gas interface, whereas the combined heat diffusion and natural convection accounts for most of the cooling at the droplet-gas interface.

In Chapter 6, the inter-droplet heat and mass exchange that leads to the asymmetrical solidification of a droplet and its adjacent neighbor on a cooled substrate are quantified. Simultaneous recordings of the IR temperature maps on the surfaces of a freezing droplet and its neighbor, as well as three-dimensional simulations of the coupled heat and mass transfer between the droplets are used to determine the fraction of heat transfer through the substrate and ambient air around the droplets. From the results contained in Chapter 6 it is concluded that:

- Non-uniform heat transfer at the solidification front of a freezing droplet leads to an asymmetrical solidification with the end tip of the droplet shifted away from its neighbor.
- This asymmetrical solidification is caused by non-uniform heat loss on the surface of the freezing droplet and non-uniform heat spreading via diffusion in the substrate caused by the presence of a neighboring droplet.
- Less than 1% of the latent heat released by a large droplet is transferred to a small neighbor, whereas its neighbor will freeze transferring about 6% of the latent heat released to the large droplet, with most of the heat transferred through the substrate.

7.2 Suggested Future Work

This section proposes a few avenues for future research on dropwise condensation and condensation freezing that result from the work presented in this dissertation

7.2.1 Including Other Mechanisms for Heat Transport into the PSSM

The point sink superposition model (PSSM) developed in this thesis accurately predicts the condensation rate of individual droplet during dropwise condensation from ambient air. In these conditions, the temperature drop across the droplet can be neglected without sacrificing accuracy in the prediction of the condensation process. Contrary to dropwise condensation from water vapor, where the condensation process is dominated by the thermal resistance across the droplet, in the presence of large amounts of non-condensable gases (e.g. condensation from ambient air) the condensation process is governed by mass diffusion in the air. In an intermediate condition between condensation from humid air (large concentration of non-condensable gases) and condensation from pure water vapor, the thermal resistance across the droplet is comparable to the thermal resistance at the interface of the droplet and the temperature drop across the droplet must be considered to estimate mass transport at the interface of each droplet. Heat transfer across each droplet can be considered by including an expression for heat diffusion within the droplet in the model for single droplet used in the PSSM and by approximating the interfacial temperature of each droplet when implementing the superposition of the water vapor distribution around the droplets.

Another possible extension for the PSSM, which results from considering the thermal resistance across the droplet, is to include the droplet heating via forced convection. In several applications, forced convection can hamper the condensation process by increasing the temperature of the droplets. A possible avenue for adding force convection effects into the PSSM is to include a term that introduce mass transport in the air domain by advection. Water vapor transport due to advection can be linearized using the thin layer approximation for the velocity terms of the governing equations for vapor transport, and then adding this contribution to the governing equation of the PSSM.

7.2.2 Improved Understand of Breath Figures Using the PSSM

Droplets condense on a surface forming a pattern know as breath figures; the spatial distribution of the droplets and the distribution of droplet size is often used for modeling for modeling dropwise condensation from water vapor. In addition to fundamental interest in understanding the self-assembled structures formed during condensation, a practical interest in controlling the patterns formed during the dropwise condensation has emerge from the potential of using breath figures formed condensing solvents on polymer films to manufacture porous membranes, microliter wells for cell culture, and other structures. Classical scaling theory describes the number of droplets per unit volume in terms of the isolated model and the film-like model for droplet growth, which fails to predict condensation experiments. As it was shown in this dissertation, droplets grow following power laws that depend on the interactions between all the droplets in the substrate. Simulations that account for droplet nucleation, coalescence, and droplet growth using the PSSM could provide new insights on the study of breath figures. A more comprehensive theory for breath figures that considers the growth of individual droplets can provide new tools for the control breath figures for tailored design of self-assembled layers.

7.2.3 Surface Design for Optimized Condensation Rates

Surfaces can be engineered to maximize condensate yield by controlling droplet nucleation, growth, and departure. Increasing the number of nucleation sites, triggering early droplet departure, and controlling droplet spatial distribution has been shown to increase the heat transfer coefficient during dropwise condensation. Superhydrophobic surfaces have been shown to promote early droplet departure by coalescence-induced droplet jumping out of the surface. Chemically patterned surfaces (e.g., hydrophilic regions on a hydrophobic background) have been used to control droplet location and facilitate early droplet roll-off. In comparison with the PSSM, previous models for dropwise condensation available in the literature cannot capture the influence of droplet size and spatial distribution that results from engineering surfaces to improve dropwise condensation. The PSSM can be used to evaluate the condensation rates produced by diverse surface designs while considering these effects.

7.2.4 Role of Substrate Properties on Droplet-To-Droplet Interactions During Freezing

Chapters 5 and 6 provide a detailed description of the pathways for latent heat dissipation from a freezing droplet to its environment and an adjacent droplet. The results consistently show that heat diffusion though the substrate is the main avenue for latent heat dissipation from the solidification front. Substrate thermal properties, as well as droplet effective contact area with the substrate significant affect the rate of solidification observed in the literature. For example, reductions in the effective contact area caused by high contact angle or air pockets in the contact region (in the case of a droplet resting on a structured surface) can limit the rate for latent heat dissipation, which results in longer freezing times. Substrate thermal properties can also impact freezing dynamics, with droplets on substrate with low thermal conductivity freezing at lower rates than in highly conducting substrates. The combined experimental and modeling methodologies developed in Chapters 5 and 6 can be leveraged to perform parametric characterization of the freezing process while varying substrate thermal properties (e.g., low and high thermal conductivity substrates), as well as freezing on substrates engineered with various surface morphologies (e.g., flat and structured) and chemical affinity with water (e.g., high and low surface wettability).

7.2.5 Non-Invasive Thermal Characterization of Inter-Droplet Freezing

As discussed in Section 2.2.2, frost propagation occurs via ice bridges that growth at the expense of the supercooled liquid droplets surrounding a freezing droplet. Two governing mechanisms for the propagation of frost have been proposed: (1) water vapor gradients caused by the difference between the saturation pressure above ice and surfaces, and (2) heating of neighboring droplets caused by the release of latent heat from a freezing droplet to the substrate. The relative significance of the role that each one of these two mechanism plays in ice bridging phenomena and the evaporation of neighboring is not well understood. This dissertation developed a methodology suitable to quantify the pathways for droplet-to-droplet interactions while highlighting that heat transfer through the substrate plays an important role in the interactions during freezing of microliter droplets. With the aim of quantifying the heat exchange occurring during condensation freezing, this section proposes the use of non-invasive temperature sampling techniques (e.g., microscopic infrared thermography, high frequency thin-thermocouple (TFT) integrated into the substrate itself) to quantify local heating produced by the propagation of frost.

Measurements of substrate temperature and droplet surface temperature using top-view infrared (IR) thermography during freezing of droplet arrays are proposed. Chemically patterned surfaces with hydrophilic dots in a hydrophobic background could be used to control the location of the droplets in the substrate. The size of the hydrophilic spots and spacemen will be engineered to control droplet location and growth in constant contact angle mode (CCA). Top-view video recordings of the condensation freezing process can be used to track the evolution of the size of each droplet. The evaporation rates of supercooled liquid droplets will be balanced with the ice generated by ice bridging and ice accretion on the surface of the droplets. The velocity and direction of the growth of ice bridges can be analyzed in terms the distribution of the supercooled liquid droplets in the neighborhood.

To prove the feasibility of the proposed experiments, preliminary infrared (IR) thermography measurements taken from a top-down view during inter-droplet frost propagation in a bed of sub-millimeter supercooled liquid droplets condensed on a silicon substrate are provided in Appendix D. The results indicate that the experimental approach to reduce spurious radiation from the environment developed in this dissertation can enable infrared temperature measurements of on the surface of sub-milliliter droplets during condensation freezing. Furthermore, temperature measurements on the surface of freezing droplets and its neighbors demonstrates that latent heat of solidification released to the substrate by freezing droplets increases the temperature of the group of nearest neighboring droplets.

7.2.6 Reduced-order modeling of frost propagation

The point superposition method developed in this dissertation, along with the understanding of droplet interactions during freezing, can be leveraged to predict the propagation of frost. As it was demonstrated in Appendix D.2, the latent heat released by a freezing droplet can increases the temperature of its neighboring droplets, with this temperature increment depending on the distance between the freezing droplet and its neighbor (e.g., closer droplets increasing their temperature more than droplets far away). By developing a model for heat transfer from a freezing droplet to its neighbors, the average temperature at the surface of the neighboring droplets can be estimated, and a point/sink model for vapor pressure above the droplets can be integrated into the system-level model described by equation (3.15). This model will account for the interactions of all the

liquid, freezing, and frozen droplets occurring during the propagation of frost. To complete a system-level description of the propagation of frost, a point sink model for ice bridging is required.

APPENDIX A. ADDITIONAL CASES FOR THE VALIDATION OF THE PSSM

This appendix presents supplementary validations for the point sink superposition method and figures of the domains used in the predictions with the PSSM consigned in Table 4.1. The first validation case corresponds to comparisons against numerical simulations using the domain and boundary conditions described in section 3.2.2. The condensation rate and normalized concentration of vapor is predicted for a system of droplets that resembles a regime of condensation when droplets have similar sizes and are closely spaced. Figure A-1 (a) and (b) show the normalized vapor concentration field for the numerical simulation and for the point sink superposition method, respectively. The vapor distribution around the droplets are similar, corroborating the applicability of the point sink superposition method. The condensation rates of individual droplets shown in Figure A-1 are shown in Table A-1. Because the droplets have similar sizes, the variation in the condensation rates predicted from the models is small. The point sink superposition method accurately predicts the condensation rates obtained from the numerical simulation. The total condensation rate error was found to be ~10%, and the error for individual droplets was generally lower than ~14%.

The second validation case corresponds to comparison of condensation rates measured during condensation experiments at substrate temperature of T_{sub} = 10.0 °C, constant air temperature of T_{∞} = 20.5 °C, and relative humidity of RH = 60%, 50%. Figure A-2 (a) shows a group of 30 droplets of interest within a domain generated using the droplets in field of view at t =31 min during experiment at RH = 60%. All the droplets in the group of interest are filled with blue inside the boundary defined by the yellow line and have been assigned an identification number. The droplets inside the field of view of the optical system are filled with red whereas the droplets filled with white lie outside the field of view. Figure A-2 (b) shows the condensation rate for each droplet within the group measured during the experiments and for two number of droplets considered in the PSSM prediction (N_{PSSM}). For this case the 391 droplets must be included to minimize the relative error between the total condensation rate of the 30 droplets measured and the PSSM prediction. Except droplet 13, the condensation rate predicted by the PSSM lies between the error bounds of the experimental condensation rates. Similar results are obtained when using

the PSSM to predict the condensation rates of a group of 30 droplets at t = 31 min during experiments at RH = 50% shown in Figure A-3 (a) and (b).

Additionally, this also section presents supplementary figures depicting the maximum cord length regions that enclose the number of droplets required to predict the condensation rate of a group of 30 droplets at different times during condensation experiments performed at T_{sub} = 10.0 °C, T_{∞} = 20.5 °C, RH = 70% which are consigned in Table 4.1. Figure A-4 shows top-down view of the model domain at t = 11, 16, 21, and 26 min. All droplets in the group of interest are filled blue inside the boundary defined by the yellow line; droplets in the experimental field of view are filled red and the droplets outside the camera field of view are filled with white. As time progresses, the number of droplets per unit area increases, thus for region with nearly constant area like the one defined by the maximum cord length (orange line), the number of droplets increases over time.

Table A-1. Condensation rate of individual droplets, as well as the overall condensation rate, for the system of droplets shown in Figure A-1. The error compares condensation rates from the numerical simulations to those obtained using the point sink superposition method.

Drop Tag	$\dot{m}$ **[x10^{-12} kg/s]**		**Error [%]**
	Numerical	**Model**	
1	6.8	7.6	12.3
2	7.5	8.5	12.6
3	11.9	12.8	7.4
4	7.4	8.4	13.0
5	9.2	10.1	9.8
6	9.0	9.8	8.6
7	10.1	10.9	9.1
8	6.1	7.0	14.3
9	10.3	10.9	5.6
10	9.1	9.7	6.2
11	5.2	6.0	13.6
12	4.4	5.0	14.0
13	6.0	6.6	9.6
14	5.7	6.5	13.8
15	8.6	9.2	7.0
16	9.8	10.3	5.4
17	10.7	11.4	6.3
18	5.4	6.0	11.0
19	8.9	9.6	7.8
Total	**151.9**	**165.9**	**9.2**

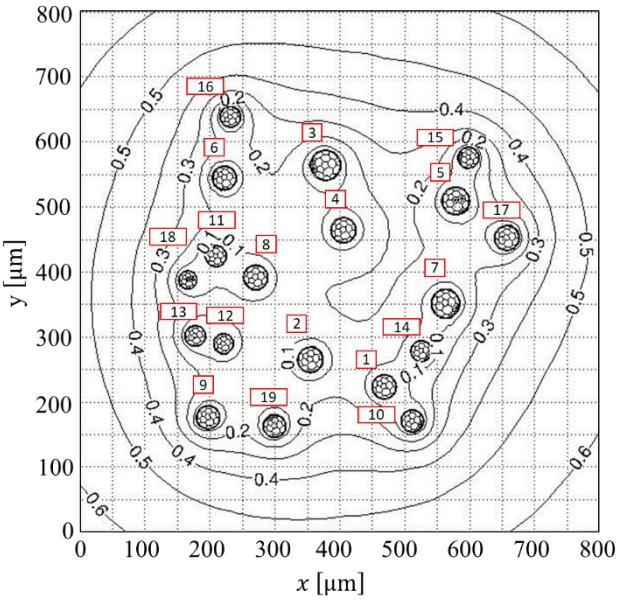

(a)

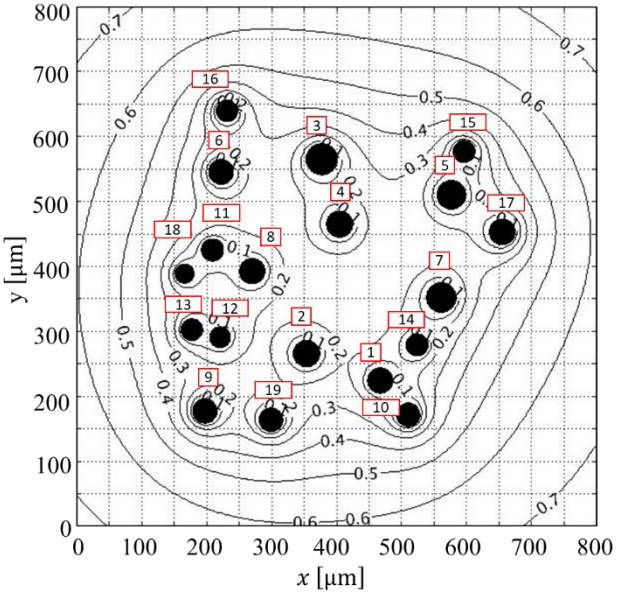

(b)

Figure A-1. Normalized vapor concentration field $\upsilon(\vec{r})$ at the substrate plane for a system of 19 condensing droplets obtained using (a) the numerical solution of the vapor diffusion equation and (b) the point sink superposition method modeling approach.

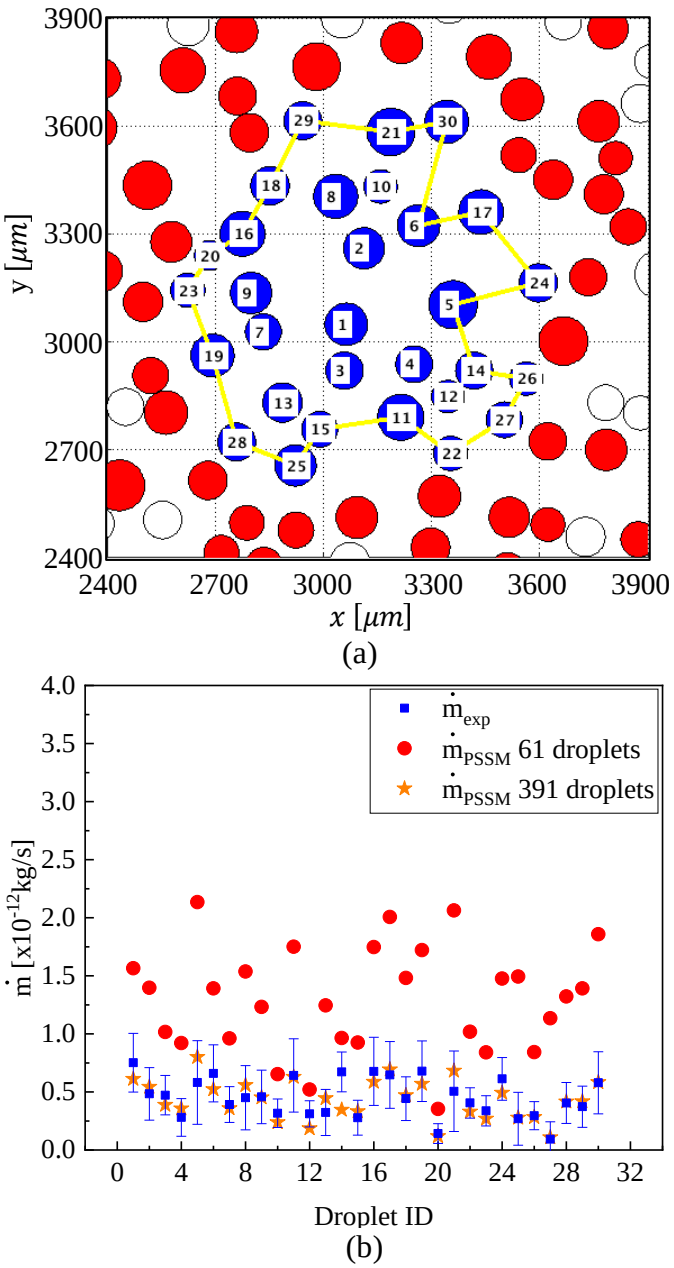

Figure A-2. Prediction of individual condensation rate of a group of 30 droplets of interest within a system of many droplets at T_{sub} = 10 °C, RH = 60%, and T_{∞} = 20.5 °C. (a) Top-down view and droplets of interest at t = 31 min. All the droplets in the group of interest are filled with blue inside the boundary defined by the yellow line and have been assigned an identification number. The droplets inside the field of view of the optical system are filled with red whereas the droplets filled with white lie outside the field of view. (b) Measured and predicted individual condensation rates for each tagged droplet of interest for differing numbers of droplets considered in the PSSM prediction. For this case, 391 droplets must be included to minimize the relative error between the measured and predicted total condensation rate

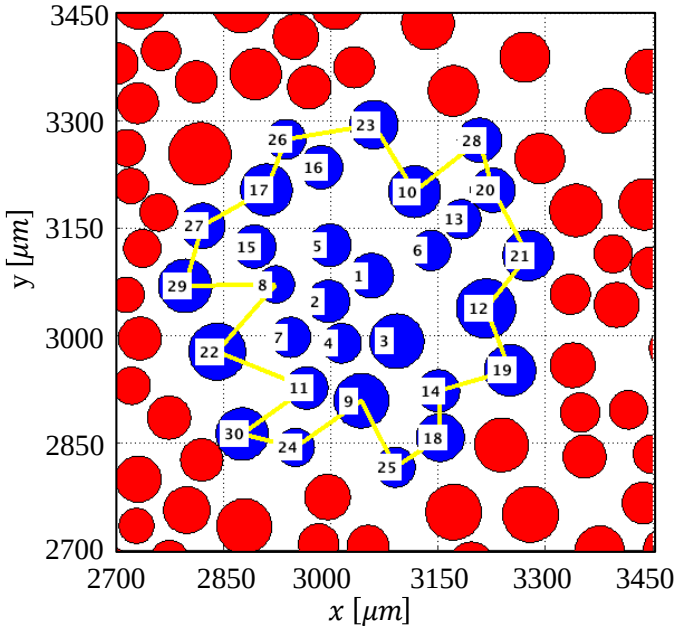

Figure A-3. Prediction of individual condensation rate of a group of 30 droplets of interest within a system of many droplets at T_{sub} = 10 °C, RH = 50%, and T_{∞} = 20.5 °C. (a) Top-down and tags on the droplets of interest at t = 31 min. All the droplets in the group of interest are filled with blue inside the boundary defined by the yellow line and have been assigned an identification number. The droplets inside the field of view of the optical system are filled with red. (b) Measured and predicted individual condensation rates for each tagged droplet of interest for differing numbers of droplets considered in the PSSM prediction. For this case, 205 droplets must be included to minimize the relative error between the measured and predicted total condensation rate

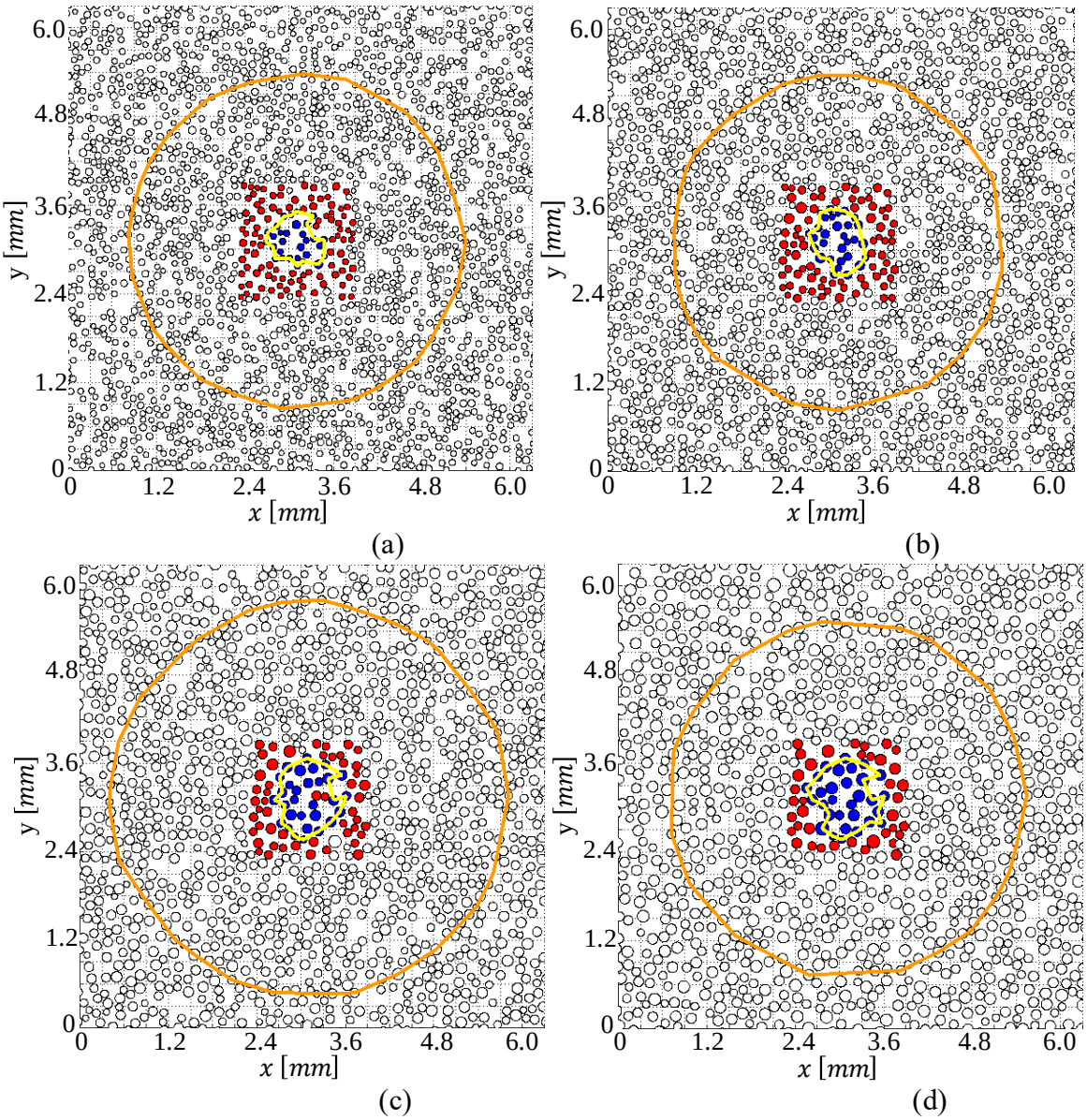

Figure A-4. Top-down view of the domain used in the PSSM prediction during experimental conditions at T_{sub} = 10 °C, RH = 70%, and T_{∞} = 20.5 °C depicting of a group of 30 droplets of interest (filled blue inside the boundary defined by the yellow line) at (a) t = 11, (b) 16, (c) 21, and (d) 26 min. Droplets inside the field of view are filled red and artificial droplets generated outside the field of view are filled white. The orange rings encompass all droplets necessary to predict the condensation rate of the droplets of interest with relative error 0.15 %. As time progresses, the number of droplets per unit area increases; thus, for a region with nearly constant area, the number of droplets increases over time

APPENDIX B. CALIBRATION OF THE INFRARED (IR) THERMOGRAPHY MEASUREMENTS

This appendix provides further details on the calibration of the infrared (IR) thermography measurements presented in Chapters 5 and 6. A custom-made black body radiator was built by mounting a 5 cm ×5 cm black-painted (ColorMasterTM Flat Black, Krylon; emissivity of 0.97) hand-sanded Aluminum surface on the sample holder of the experimental facility described in Section 5.1. The black body calibrator was employed to calibrate the infrared camera over a range of set-point temperatures from -8.5 °C to 22.5 °C in 1.0 °C increments. The camera integration time was set to 2000 μs to maximize the acquired signal amplitude and the recording frequency was set to 50 Hz (1 frame recorded every 0.02 s). The recording frequency was selected to capture the rapid changes in temperature during recalescence process, which occurs over the order of tens of milliseconds. At each setpoint temperature, the IR camera is used to record the digital level (DL) averaged over 100 frames (2 sec); these averaged calibration images are used to perform pixel-by-pixel calibration and non-uniformity correction of the experimental images. A calibration algorithm fits the DL to a unique fourth-order polynomial for each sensor pixel. A sample calibration curve for a single pixel is provided in Figure B-1.

Additional calibrations are performed to improve the accuracy of the infrared temperature measurements. Specifically, corrections are made to reduce errors caused by background radiation that is reflected off the surface of the droplet, as well as to account for nonuniform emissivity of the surface due to its curvature. Due to the low range of temperatures in the experiment and the geometry of the experimental facility, the infrared thermography measurements are especially sensitive to background radiation. These two effects can be examined by comparing the temperature distribution immediately after recalescence (uniform and equal to 0 °C) and the infrared temperature measurements. The temperature map of the surface of the 10.1 μL droplet after recalescence that is presented in Figure B-2 shows that the temperature measurements deviate from the freezing equilibrium temperature. Near the center of the droplet, background radiation coming from the environment through the view window of the cold enclosure is reflected by the droplet causing temperature measurements ~0.8 °C above the equilibrium freezing temperature. Nonuniform emissivity due to the curvature of the droplet causes apparent sub-freezing temperatures measurements near the droplet-interface. Infrared temperature measurements must

be corrected at each location of the surface of the droplet to account for this effect. For example, one previous approach by Chandramohan *et al.* [106] used the shape of the droplet to map the emissivity changes on the surface of the droplets, and used this correction map to estimate the temperature. In the case of a freezing droplet, for which the droplet shape slight changes due to expansion of the water during solidification, implementation such a spatially dependent correction is challenging. Assuming that the changes in temperature due to the nonuniform emissivity are negligible in comparison with the changes in temperature due to constant background radiation, we adopt a simple approach to correct for the background radiation by calculating the difference between the measured infrared temperature of the droplet after recalescence and the equilibrium freezing temperature. This difference is then applied as an in-situ correction to all the temperature contours in the frames that follow throughout the experiment. Figure B-3 (a) and (b) present infrared temperatures before and after application of this in-situ correction at t = 10.10 s during the solidification of the 10.1 μL droplet.

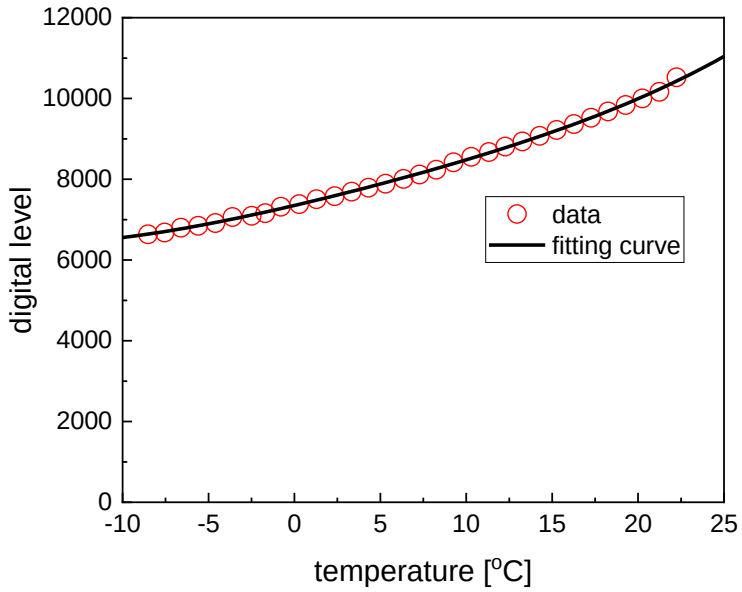

Figure B-1. Representative calibration curve for a single pixel in the infrared camera frame with the corresponding calibration points.

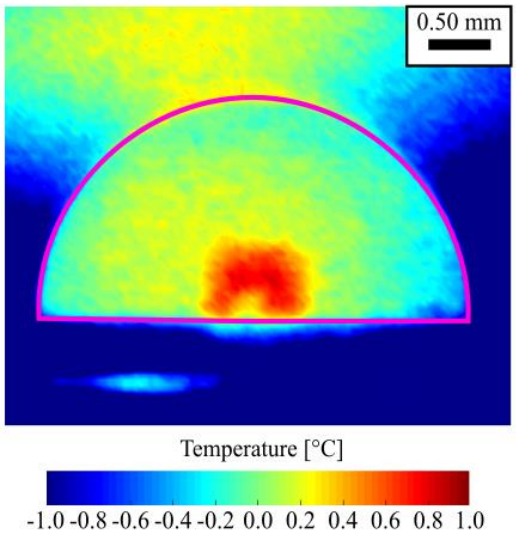

Figure B-2. Experimental image of the infrared temperature measurement captured for the 10.1 µL droplet. Note that this image includes data in the background outside the droplet interface and outside the focal plane; only data on the droplet interface (magenta line) should be interpreted as calibrated temperatures.

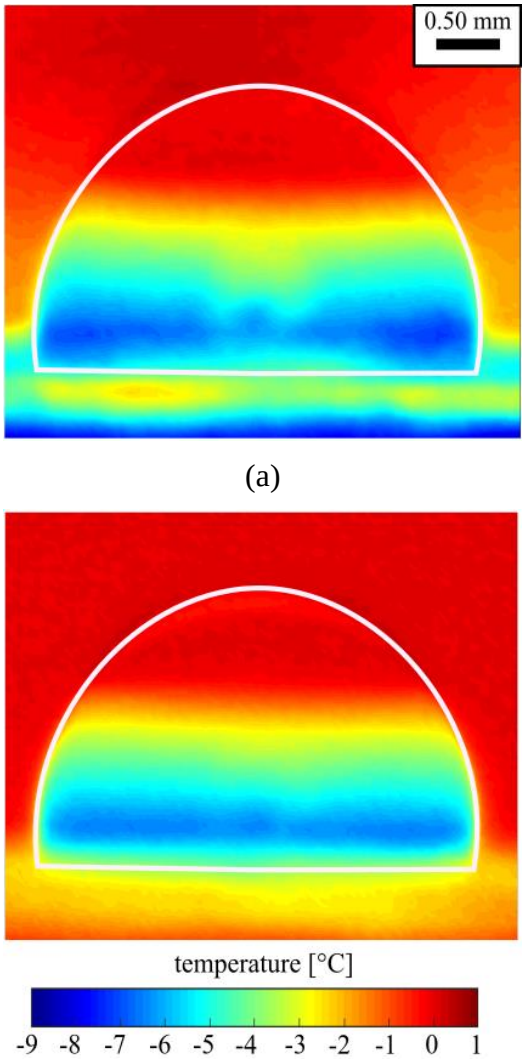

Figure B-3. Infrared temperature measurement at t = 10.10 sec during the solidification of the 10.1 µL droplet (a) before and (b) after the in-situ correction using the post-recalescence temperature of the droplet. Note that these images include data in the background outside the droplet interface (white line) and outside the focal plane; only the data on the droplet interface should be interpreted as calibrated temperatures.

APPENDIX C. CALCULATING THE WATER VAPOR CONTENT IN THE AIR DOMAIN

This appendix provides additional details on the implementation of user defined scalar functions (UDS) used Section 5.2 to solve for to solve for the diffusive and convective transport of water vapor within the air domain given in equation (4.19). To implement equation (4.19) in the Fluent solver, the mole concentration must be expressed in terms of the mass fraction of water vapor in the vapor-air mixture ω as:

$$C_v = \frac{\rho_g \omega}{M_{water}} \tag{C.1}$$

where ρ_g is the density of vapor-air mixture, C_v is the vapor molar concentration, and M_{water} is the molecular weight of water. Equation (C.1) is substituted in equation (4.19) to obtain the governing equation in terms of the mass fraction of water vapor as:

$$\vec{V} \cdot \nabla \rho_s \omega - \nabla \cdot \left(\Gamma \cdot \nabla \omega \right) = 0 \tag{C.2}$$

where the diffusivity coefficient Γ is defined as:

$$\Gamma = \rho_g D \tag{C.3}$$

The vapor mass fraction at the droplet-gas interface and the far-field boundaries of domain are set as boundary conditions to solve equation (C.2). At the droplet-gas interface, the vapor mass fraction is set based on the temperature at the interface. Because the partial pressure of water vapor is different above ice versus liquid water at the same temperature, two independent polynomial correlations for the saturation vapor pressure above ice [107] and water [108], are used to calculate the partial pressure above the droplet-gas interface. For face cells on the droplet-gas interface above ice, for temperatures between -100 °C and below 0 °C, the correlation used to calculate the partial pressure is:

$$\ln(p) = \sum_{i=0}^{4} d_i T^{i-1} + d_5 \ln(T) \tag{C.4}$$

where p is the partial pressure water vapor, T is the temperature within the cell, and the constants d_i with i = 1, 2, 3, 4, and 5 are fitting parameters with values listed in Table C-1. For any cell in the domain and between 0◦C and 100 ℃, the saturation vapor pressure is calculated using the polynomial correlation [108]:

$$\ln(p) = \sum_{i=0}^{3} e_i T^{i-1} + e_4 \ln(T) \tag{C.5}$$

where the constants e_i with i = 1, 2, 3, and 4 are fitting parameters listed in Table C-1.

In any cell within the gas domain, the local partial pressure of water vapor is set as the saturation pressure. Therefore, the mass fraction ω defined as the ratio between the actual mass of vapor and the mass of the vapor-air mixture is calculated using the following equation:

$$\omega = p_v * M_{water} / ((p_{atm} - p_v) * M_{air} + p_v * M_{water}) \tag{C.6}$$

where p_v is the partial pressure of water vapor, p_{atm} is set equal to the atmospheric pressure (101.325 kPa), and M_{air} is the molecular mass of air. At the top and lateral walls of the gas domain, the vapor mass fraction is calculated from the far-field temperature and relative humidity using equation (4.30).

Table C-1. Fitting constants used for the vapor pressure polynomial correlations.

i	d_i	e_i
0	-0.5865×10^{4}	-0.6044×10^{4}
1	0.2224×10^{2}	0.1893×10^{2}
2	0.1375×10^{-1}	-0.2825×10^{-1}
3	-0.3403×10^{-4}	0.1725×10^{-4}
4	0.2697×10^{-7}	0.2858×10^{1}
5	0.6919	

APPENDIX D. PRELIMINARY INFRARED (IR) THERMOGRAPHY MEASUREMENTS DURING CONDENSATION FREEZING

This appendix presents preliminary top-down view infrared (IR) thermography and video recording the propagation of frost on a smooth hydrophilic cooled substrate.

D.1. Experimental Description

The experimental facility described Section 5.1 is modified for capturing infrared thermography video recordings from a top-down view during condensation freezing. A schematic diagram of the renovated test section is shown in Figure D-1. Similar to the experimental facility presented in Section 5.1, the test section used in this section is surrounded by a black painted aluminum cold enclosure is used to reduce the influence of spurious reflections and to maintain uniform background radiation. In this section, a 12 cm x 12 cm square window is cut off from the top wall to allow access. All the cooling systems described in Section 5.1 were used in the experiments presented in this section. Smooth silicon samples were prepared with the procedure described in Section 4.1.1.

After placing a clean sample inside the test section, the top lid of the enclosure is bolted to the lower base. To set the background temperature, the two cooling stages are turned on at set temperature of a -1.5 °C, while the thermoelectric stage, which controls the temperature of the substrate, is set to a setpoint temperature of 5.0 °C. After ~5 min, liquid droplets nucleate on the substrate and subsequently grow by vapor diffusion and coalescence. Subsequently, after the droplets have grown to a desired size, the setpoint temperature of the thermoelectric stage controller is set to - 6.0 °C. After ~ 4 min frost nucleates near the edges of the substrates, and propagates towards the center, and after ~ 25 min frost has propagated throughout substrate.

Temperature recordings from the top down view of the substrate are shoot at 50 fps using an infrared camera (SC7650, FLIR). A 4.0x microscope objective lens (ASIO, Janos) provides a depth of focus of 55.5 μm and spatial resolution of 0.0102 ± 0.003 mm/pixel, where the uncertainty in the spatial resolution is taken as the standard deviation over 10 calibration measurements. A custom-made black body radiator was used to calibrate the infrared camera over a range of set-point temperatures from -10.0 °C to 22.0 °C in 1.0 °C increments. At each setpoint temperature, the IR camera is used to record the digital level averaged over 20 frames. The digital level is fitted

as a function of the setpoint temperature with a fourth-order polynomial for each sensor pixel. This pixel-by-pixel calibration is applied to the experimental data.

D.2. Droplet Freezing in a Population of Droplets

A sequence of top-down-viewed contour temperature maps on the surface of a group of supercooled liquid droplets on a cooled substrate while one of the droplets is freezing is shown in Figure D-2. Numeric labels are assigned to each droplet and their edges are delineated with white dashed circles. Within the droplets, small variations in the temperature are due to droplet curvature and lens reflections. At 0.02 s in Figure D-2, ice crystals that nucleate near the contact base of the droplet have propagated throughout most of the volume of droplet 0, which suddenly increases its temperature up to ~ 0.0 °C. After this recalescence process has been completed, droplet 0 cools down as it solidifies, and after 0.12 s the droplet has entirely frozen. As it was shown in Chapter 6, the latent heat dissipated by a freezing droplet heats a neighboring droplet. Throughout the freezing droplet 0, an increase in the average temperature of all the neighboring droplets (droplets 1 to 10) is measured. At 0.08 s, the neighboring droplets that are closer to droplet 0 (e.g. droplet 8 and 3) have an average temperature that is about ~0.5 °C from their initial value at 0.0 s, meanwhile the average temperature of droplets that are farther away (e.g., droplet 9 and 2) have increase by about 0.2 °C.

The preliminary top-view IR temperature video recordings presented in this Section show that by reducing ambient radiation during condensation freezing experiments, temperature maps with high spatial resolution can be used to track the evolution of the crystallization front during droplet recalescence and subsequent solidification, as well as temperature changes in a group of neighboring droplets. These IR temperature images have enough spatial resolution to track the evolution of the size of each droplet and the growth of ice bridges. The evaporation rates of supercooled liquid droplets can be balanced with the ice generated by ice bridging and ice accretion on the surface of the droplets. Temperature measurements on the surface of ice bridges could help in determining whether frost growth occurs at T_{eq} or if ice bridges are driven by frost accretion at a much lower temperature T_{eq}. Furthermore, the combined thermal characterization and growth dynamics can be later used to investigate the role of latent heat in the velocity and direction of the growth of ice bridges.

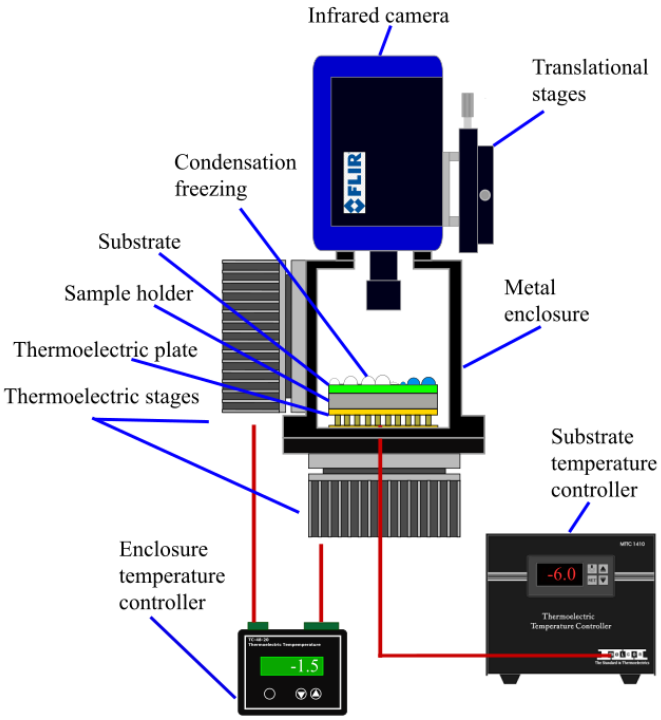

Figure D-1. Schematic diagram of the experimental facility used for infrared thermography (IR) measurements during condensation freezing.

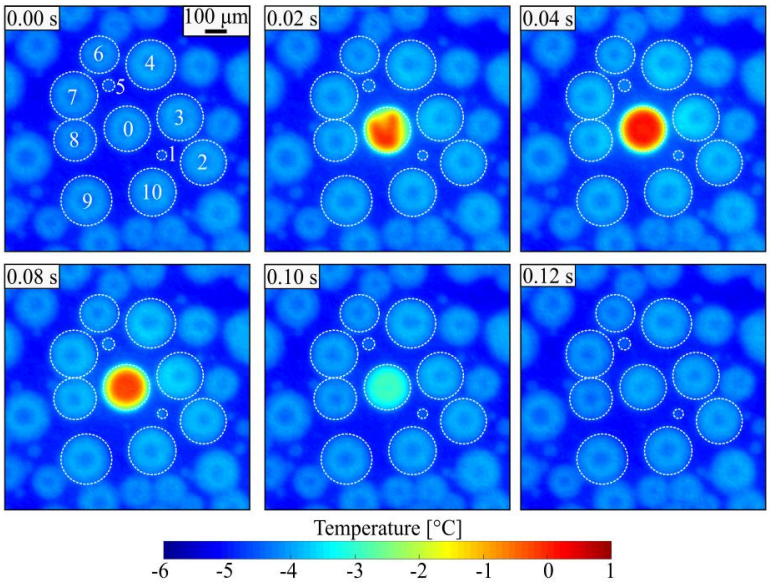

Figure D-2. Sequence of temperature contour plots from the top down view showing a group of supercooled liquid droplets while droplet 0 is freezing. The edge of the droplet is delineated with black (freezing droplet) and white (neighboring droplets) dashed circles.

APPENDIX E. A PRELIMINARY METHODOLOGY FOR DEVELOPING A POINT SUPERPOSITION METHOD FOR CONDENSATION FREEZING

This appendix proposes a reduced-order modeling approach for the propagation of condensation frost on hydrophobic surfaces. A series of incremental developments starting with modeling droplet freezing as a point/sink source, followed by a reduced-order model for the interaction of a pair of droplet, and ending with a formulation for the superposition of the vapor and temperature fields are described in Sections E.1, and E.2 of this appendix

E.1. Modeling Single Droplet Freezing as a Point Sink/Source

As shown in Chapter 5, single droplet freezing is accompanied by coupled heat and mass transfer processes that are time-dependent and vary with space (*i.e.* variation of temperature at the droplet-air interface). To provide a simplified model for single droplet freezing, a first approximation could be to assume that most of the heat transfer occurs between the droplet and the substrate. In this case, the diffusion of vapor in the air domain could be solved by introducing a time-dependent source that resembles the changes in the concentration of water vapor caused by a freezing droplet. One possible approach to model a freezing droplet as a point could be to develop a time-dependent sink/source intensity ($\Omega(t)$) model that captures the variations of vapor pressure above the surface of the droplet due to the evolution of droplet mean temperature during freezing (*i.e*. sudden increase in temperature during recalescence, temperature decrease during cooling and constant temperature prior recalescence and after solidification). Figure E-1 shows a schematic plot of the saturation vapor pressure changes above a freezing point from recalescence to complete solidification. At the onset of recalescence, the temperature of the droplet it is assumed uniform and equal to T_{sub}, the saturation pressure of the vapor over water at that temperature will be $P_{l,sub}$. Just after recalescence, the vapor pressure at the interface droplet is assumed to be equal to the saturation vapor pressure over ice at 0 °C; that is, $P_{ice,0}$ = 611.2 Pa. As the droplet solidifies and cools down toward the temperature of the substrate, the saturation vapor decreases to $P_{ice,sub}$, where $P_{ice,sub} < P_{l,sub}$. This approach will require further assuming that the water vapor pressure above the surface of the droplet is equal to the saturation pressure at the average temperature of

the interface of the droplet. If it is further assumed that the air above the droplet can be treated as an ideal gas, the concentration of vapor can be calculated from $\left(c_s(t) = MP_{sat@T_i} / RT_i(t)\right)$, where P_{sat} will depend on whether the droplet is in liquid state or solid [97]. In this case, the distribution of vapor in the air surrounding a freezing droplet can be approximated from the governing equation for transient diffusion with a time-dependent point source:

$$D\nabla^2 c(\vec{r}) - \left(\partial c/\partial t\right) = \delta(\vec{r} - \vec{r}_j)\Omega(t) \tag{E.7}$$

Closed-form solutions to equation (E.7) are available in the literature for cases where $\Omega(t)$ have a simple form or is independent from time [109]. The water vapor mass fraction contour plots presented in 5.3.3.3 can be used to benchmark a model for $\Omega(t)$ that accurately predict the vapor concentration changes that results from droplet freezing on a cooled substrate that can be later used to develop a system level model for the propagation of condensation freezing.

E.2. Extending the Point Sink Superposition Method (PSSM) for Freezing of a pair of Droplets

The potential future work described in this section is to develop a point sink/source model for the water vapor diffusion occurring between a pair of freezing droplets, which can be later extended to a system of many droplets. Once a solution for the transient evolution of the water vapor concentration around a single point representing a freezing droplet proposed in Section E.1 has been obtained, the next challenge in obtaining a system-level model is to simultaneously account for supercooled liquid and freezing droplets. The PSSM described in Section 3.1 is limited for system of droplets where the concentration of water vapor above the surface of all droplets is the same. As a preliminary result, this section modifies the PSSM to include sources and demonstrates its utility in visualizing water vapor fluxes between a frozen droplet and a supercooled neighbor. The procedure described in this section, can be applied to extend the model to a system of many droplets.

For a pair of freezing droplets on a substrate with contact angle $\theta_1 = \theta_2 = \theta$, located at $\vec{r}_1$ and $\vec{r}_2$, with contact radius $R_{c,1}$ and $R_{c,2}$ equation (3.11) can be written:

$$c_\infty - c_{s,1} = \frac{\dot{m}_{sys,1}}{\pi D f(\theta) R_{c,1}} + \frac{\dot{m}_{sys,2}}{\pi D f(\theta) |\vec{r}_1 - \vec{r}_2|} \tag{E8}$$

$$c_\infty - c_{s,2} = \frac{\dot{m}_{sys,1}}{\pi D f(\theta) |\vec{r}_2 - \vec{r}_1|} + \frac{\dot{m}_{sys,2}}{\pi D f(\theta) R_{c,2}} \tag{E9}$$

where $c_{s,1}$ and $c_{s,2}$ are the water vapor concentration at the surface of the droplets, which are assumed uniform along the interface of the droplets. By making a similar algebraic manipulations and using the same assumptions described in Section 3.1.2.2, equations (E8) and (E9) can re-written as the system of linear equations:

$$1 = \eta_1 + \eta_2 \left(\frac{c_\infty - c_{s,2}}{c_\infty - c_{s,1}} \right) \frac{R_{c,2}}{|\vec{r}_1 - \vec{r}_2|} \tag{E10}$$

$$1 = \eta_1 \left(\frac{c_\infty - c_{s,1}}{c_\infty - c_{s,2}} \right) \frac{R_{c,1}}{|\vec{r}_2 - \vec{r}_1|} + \eta_2 \tag{E11}$$

Solving for the correction factors of the η_1 and η_2 one can arrive to similar expressions to the ones obtained for a pair of condensing droplets in Section 3.2.1:

$$\eta_1 = \frac{1 - \left(\frac{c_\infty - c_{s,2}}{c_\infty - c_{s,1}} \right) \frac{R_{c,2}}{p}}{1 - \frac{R_{c,1} R_{c,2}}{p^2}} \qquad \eta_2 = \frac{1 - \left(\frac{c_\infty - c_{s,1}}{c_\infty - c_{s,2}} \right) \frac{R_{c,1}}{p}}{1 - \frac{R_{c,1} R_{c,2}}{p^2}} \tag{E12}$$

The rate of condensation/evaporation of each droplet can be calculated from this set of equations, and subsequently the concentration of water vapor around the pair of droplets can be mapped by replacing those values in equation into equation (3.11).

Consider a pair of equally sized ($R_{c,1}$ = $R_{c,2}$ = 1.0 mm) droplets freezing on a cooled substrate and separated 4.0 mm, comparable to the cases examined in Chapter 6. The time-dependent vapor concentration above the droplets shown in Figure E-2 is construed based on a temperature for the substrate equal to T_{sub} = -8.5 °C, a temperature at the equilibrium equal to T_f

= 0 °C, an increase of the temperature of the neighboring droplet equal to T_{1-2} = 1 °C, and the freezing time (t_f = 7.5s); all of these values are based on the temperatures observed from freezing experiments presented in Section 6.3. The sudden increase in the concentration of vapor above the droplets at t = 1 s and t = 9.5 s, and the subsequent decrease, represent freezing of droplet 1 and 2, respectively. During the time in between droplets 1 and 2 freezing (8.5 s < t < 9.5 s), the difference between the concentration of vapor above the surface represent sink/source interaction between a frozen droplet and a supercooled liquid neighbor. Contour plots of the concentration of vapor in the air before (at t = 0 s) and after (at t = 1.1 s) freezing of droplet 1 are shown in Figure E-3 with zoomed-in regions near the center of the domain showing the gradients of concentration with black arrows between 4.5mm < x < 5.5 mm in parts (c) and (d). By comparing Figure E-3 (a) and (b), it can be observed that the concentration of water vapor around droplet 1 shrinks after freezing, which will lead to a net flux of vapor towards droplet 1 as shown in Figure E-3 (b). This result provides further evidence that shows neighboring droplets can induce evaporation from a freezing droplet.

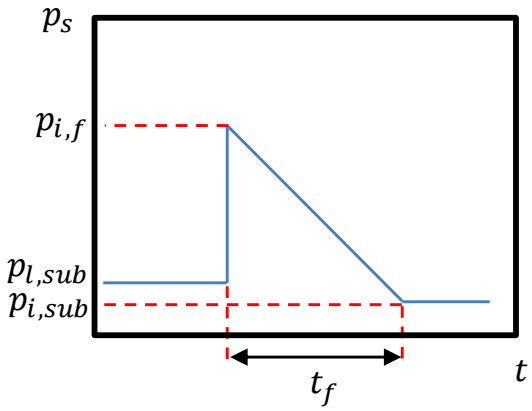

Figure E-1. Schematic plot of the simplified point/sink model for vapor pressure above a single droplet freezing.

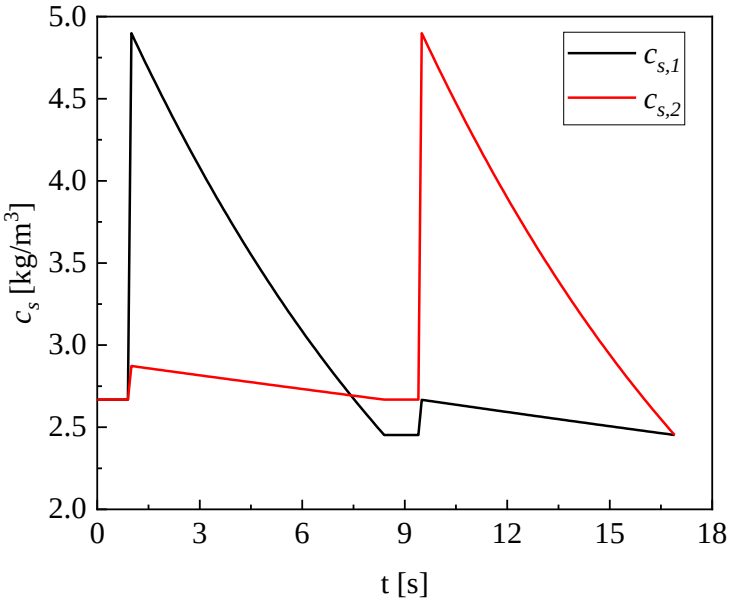

Figure E-2. Evolution of vapor concentration above the surface of a pair of equally sized droplets with the onset of freezing occurring at t = 1s for droplet 1 and t = 8.5s for droplet 2.

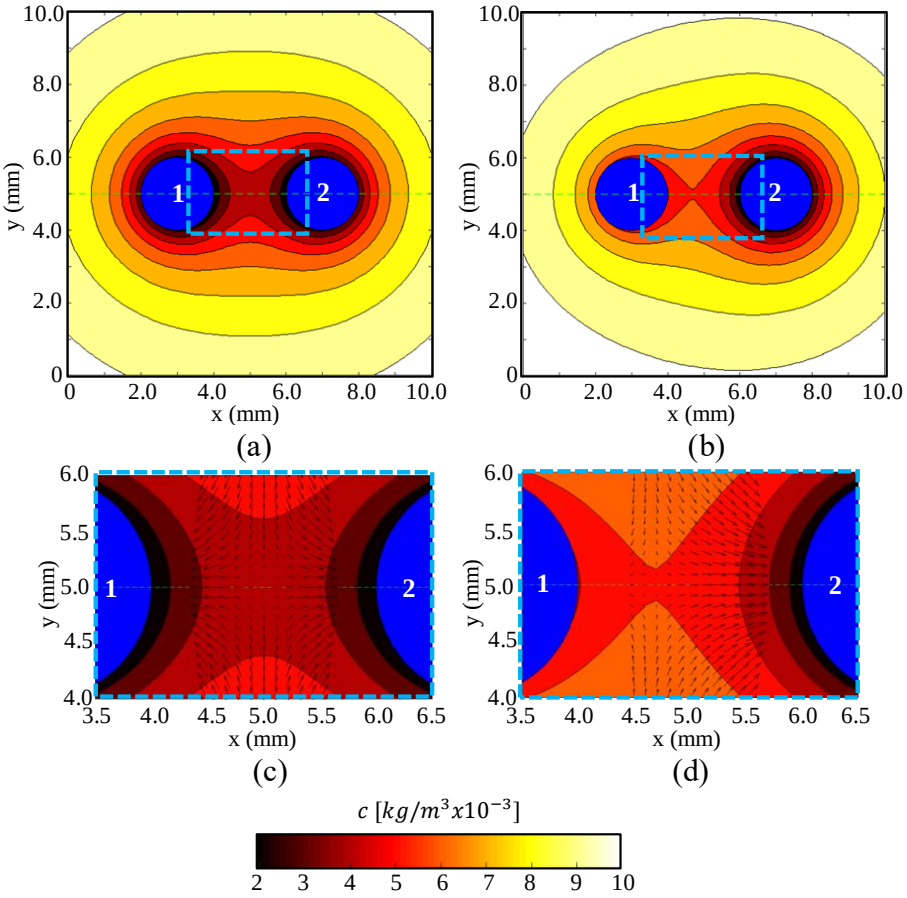

Figure E-3. Contour plots of the concentration of water vapor in the air around a pair of equally sized freezing droplets at (a) t = 0s and (b) t = 1.1s with their corresponding zoomed views near the centers of the droplet in (c) and (d).

REFERENCES

[1] C.R. Tracy, Laurence Nathalie, K.A. Christian, Condensation onto the skin as a means for water gain by tree frogs in tropical australia., The American Naturalist. 178 (2011) 553–558. https://doi.org/10.1086/661908.

[2] A.J. Hill, T.E. Dawson, O. Shelef, S. Rachmilevitch, The role of dew in Negev Desert plants, Oecologia. 178 (2015) 317–327. https://doi.org/10.1007/s00442-015-3287-5.

[3] M. Tomaszkiewicz, M. Abou Najm, D. Beysens, I. Alameddine, M. El-Fadel, Dew as a sustainable non-conventional water resource: a critical review, Environ. Rev. 23 (2015) 425–442. https://doi.org/10.1139/er-2015-0035.

[4] H. Vuollekoski, M. Vogt, V.A. Sinclair, J. Duplissy, H. Järvinen, E.-M. Kyrö, R. Makkonen, T. Petäjä, N.L. Prisle, P. Räisänen, M. Sipilä, J. Ylhäisi, M. Kulmala, Estimates of global dew collection potential on artificial surfaces, Hydrol. Earth Syst. Sci. 19 (2015) 601–613. https://doi.org/10.5194/hess-19-601-2015.

[5] D. Beysens, M. Muselli, I. Milimouk, C. Ohayon, S.M. Berkowicz, E. Soyeux, M. Mileta, P. Ortega, Application of passive radiative cooling for dew condensation, Energy. 31 (2006) 2303–2315. https://doi.org/10.1016/j.energy.2006.01.006.

[6] D. Beysens, I. Milimouk, V. Nikolayev, M. Muselli, J. Marcillat, Using radiative cooling to condense atmospheric vapor: a study to improve water yield, Journal of Hydrology. 276 (2003) 1–11. https://doi.org/10.1016/S0022-1694(03)00025-8.

[7] D. Milani, A. Abbas, A. Vassallo, M. Chiesa, D.A. Bakri, Evaluation of using thermoelectric coolers in a dehumidification system to generate freshwater from ambient air, Chemical Engineering Science. 66 (2011) 2491–2501. https://doi.org/10.1016/j.ces.2011.02.018.

[8] A. Lee, M.-W. Moon, H. Lim, W.-D. Kim, H.-Y. Kim, Water harvest via dewing, Langmuir. 28 (2012) 10183–10191. https://doi.org/10.1021/la3013987.

[9] P.S. Mahapatra, A. Ghosh, R. Ganguly, C.M. Megaridis, Key design and operating parameters for enhancing dropwise condensation through wettability patterning, International Journal of Heat and Mass Transfer. 92 (2016) 877–883. https://doi.org/10.1016/j.ijheatmasstransfer.2015.08.106.

[10] J.E. Castillo, J.A. Weibel, S.V. Garimella, The effect of relative humidity on dropwise condensation dynamics, International Journal of Heat and Mass Transfer. 80 (2015) 759–766. https://doi.org/10.1016/j.ijheatmasstransfer.2014.09.080.

[11] I.O. Ucar, H.Y. Erbil, Use of diffusion controlled drop evaporation equations for dropwise condensation during dew formation and effect of neighboring droplets, Colloids and Surfaces A: Physicochemical and Engineering Aspects. 411 (2012) 60–68. https://doi.org/10.1016/j.colsurfa.2012.07.002.

[12] M.-G. Medici, A. Mongruel, L. Royon, D. Beysens, Edge effects on water droplet condensation, Phys. Rev. E. 90 (2014) 062403. https://doi.org/10.1103/PhysRevE.90.062403.

[13] D. Beysens, Dew nucleation and growth, Comptes Rendus Physique. 7 (2006) 1082–1100. https://doi.org/10.1016/j.crhy.2006.10.020.

[14] R. Carriveau, A. Edrisy, P. Cadieux, R. Mailloux, Ice adhesion issues in renewable energy infrastructure, Journal of Adhesion Science and Technology. 26 (2012) 447–461. https://doi.org/10.1163/016942411X574592.

[15] T.K. Mideksa, S. Kallbekken, The impact of climate change on the electricity market: A review, Energy Policy. 38 (2010) 3579–3585. https://doi.org/10.1016/j.enpol.2010.02.035.

[16] J.L. Laforte, M.A. Allaire, J. Laflamme, State-of-the-art on power line de-icing, Atmospheric Research. 46 (1998) 143–158. https://doi.org/10.1016/S0169-8095(97)00057-4.

[17] Y. Cao, Z. Wu, Y. Su, Z. Xu, Aircraft flight characteristics in icing conditions, Progress in Aerospace Sciences. 74 (2015) 62–80. https://doi.org/10.1016/j.paerosci.2014.12.001.

[18] J.C. Andrey, Relationships between weather and traffic safety., (1990).

[19] O. Parent, A. Ilinca, Anti-icing and de-icing techniques for wind turbines: Critical review, Cold Regions Science and Technology. 65 (2011) 88–96. https://doi.org/10.1016/j.coldregions.2010.01.005.

[20] W.S. Pike, Extreme warm frontal icing on 25 February 1994 causes an aircraft accident near Uttoxeter, Meteorological Applications. 2 (1995) 273–279. https://doi.org/10.1002/met.5060020310.

[21] Aircraft De-Icing Market Worth $1.30 Billion by 2020, PR Newswire; New York. (2015). http://search.proquest.com/docview/1671049892/abstract/1B3EBAE187214796PQ/1 (accessed October 20, 2018).

[22] D.F. Vitaliano, An economic assessment of the social costs of highway salting and the efficiency of substituting a new deicing material, Journal of Policy Analysis and Management. 11 (1992) 397–418. https://doi.org/10.2307/3325069.

[23] M. Amer, C.-C. Wang, Review of defrosting methods, Renewable and Sustainable Energy Reviews. 73 (2017) 53–74. https://doi.org/10.1016/j.rser.2017.01.120.

[24] L. Fay, X. Shi, Environmental impacts of chemicals for snow and ice control: state of the knowledge, Water Air Soil Pollut. 223 (2012) 2751–2770. https://doi.org/10.1007/s11270-011-1064-6.

[25] S. Nath, S.F. Ahmadi, J.B. Boreyko, A review of condensation frosting, Nanoscale and Microscale Thermophysical Engineering. 21 (2017) 81–101. https://doi.org/10.1080/15567265.2016.1256007.

[26] J.B. Boreyko, C.P. Collier, Delayed frost growth on jumping-drop superhydrophobic surfaces, ACS Nano. 7 (2013) 1618–1627. https://doi.org/10.1021/nn3055048.

[27] J.B. Boreyko, R.R. Hansen, K.R. Murphy, S. Nath, S.T. Retterer, C.P. Collier, Controlling condensation and frost growth with chemical micropatterns, Scientific Reports. 6 (2016). https://doi.org/10.1038/srep19131.

[28] X. Sun, V.G. Damle, A. Uppal, R. Linder, S. Chandrashekar, A.R. Mohan, K. Rykaczewski, Inhibition of condensation frosting by arrays of hygroscopic antifreeze drops, Langmuir. 31 (2015) 13743–13752. https://doi.org/10.1021/acs.langmuir.5b03869.

[29] T.M. Schutzius, S. Jung, T. Maitra, P. Eberle, C. Antonini, C. Stamatopoulos, D. Poulikakos, Physics of Icing and rational design of surfaces with extraordinary icephobicity, Langmuir. 31 (2015) 4807–4821. https://doi.org/10.1021/la502586a.

[30] M.J. Kreder, J. Alvarenga, P. Kim, J. Aizenberg, Design of anti-icing surfaces: smooth, textured or slippery?, Nature Reviews Materials. 1 (2016) 15003. https://doi.org/10.1038/natrevmats.2015.3.

[31] M. Wen, L. Wang, M. Zhang, L. Jiang, Y. Zheng, Antifogging and icing-delay properties of composite micro- and nanostructured surfaces, ACS Applied Material and Interfaces. 6 (2014) 3963–3968. https://doi.org/10.1021/am405232e.

[32] S. Nath, J.B. Boreyko, On localized vapor pressure gradients governing condensation and frost phenomena, Langmuir. 32 (2016) 8350–8365. https://doi.org/10.1021/acs.langmuir.6b01488.

[33] J.L. Viovy, Scaling description for the growth of condensation patterns on surfaces, Physics Review A. 37 (1988) 4965–4970. https://doi.org/10.1103/PhysRevA.37.4965.

[34] D. Fritter, C.M. Knobler, D.A. Beysens, Experiments and simulation of the growth of droplets on a surface (breath figures), Physics Review A. 43 (1991) 2858–2869. https://doi.org/10.1103/PhysRevA.43.2858.

[35] J. Blaschke, T. Lapp, B. Hof, J. Vollmer, Breath figures: Nucleation, growth, coalescence, and the size distribution of droplets, Physical Review Letters. 109 (2012). https://doi.org/10.1103/PhysRevLett.109.068701.

[36] R.N. Leach, F. Stevens, S.C. Langford, J.T. Dickinson, Dropwise condensation: Experiments and simulations of nucleation and growth of water drops in a cooling system, Langmuir. 22 (2006) 8864–8872. https://doi.org/10.1021/la061901+.

[37] X. Chen, R. Ma, H. Zhou, X. Zhou, L. Che, S. Yao, Z. Wang, Activating the Microscale Edge effect in a hierarchical surface for frosting suppression and defrosting promotion, Scientific Reports. 3 (2013) srep02515. https://doi.org/10.1038/srep02515.

[38] Y.O. Popov, Evaporative deposition patterns: Spatial dimensions of the deposit, Physics Review E. 71 (2005) 036313. https://doi.org/10.1103/PhysRevE.71.036313.

[39] W.A. Sirignano, Advances in droplet array combustion theory and modeling, Progress in Energy and Combustion Science. 42 (2014) 54–86. https://doi.org/10.1016/j.pecs.2014.01.002.

[40] K. Annamalai, W. Ryan, S. Chandra, Evaporation of multicomponent drop arrays, Journal of Heat Transfer. 115 (1993) 707–716. https://doi.org/10.1115/1.2910742.

[41] X. Zhang, X. Liu, X. Wu, J. Min, Experimental investigation and statistical analysis of icing nucleation characteristics of sessile water droplets, Experimental Thermal and Fluid Science. 99 (2018) 26–34. https://doi.org/10.1016/j.expthermflusci.2018.07.027.

[42] G. Chaudhary, R. Li, Freezing of water droplets on solid surfaces: An experimental and numerical study, Experimental Thermal and Fluid Science. 57 (2014) 86–93. https://doi.org/10.1016/j.expthermflusci.2014.04.007.

[43] A. Alizadeh, M. Yamada, R. Li, W. Shang, S. Otta, S. Zhong, L. Ge, A. Dhinojwala, K.R. Conway, V. Bahadur, A.J. Vinciquerra, B. Stephens, M.L. Blohm, Dynamics of Ice Nucleation on water repellent surfaces, Langmuir. 28 (2012) 3180–3186. https://doi.org/10.1021/la2045256.

[44] S. Jung, M.K. Tiwari, N.V. Doan, D. Poulikakos, Mechanism of supercooled droplet freezing on surfaces, Nature Communications. 3 (2012) 615. https://doi.org/10.1038/ncomms1630.

[45] F. Aliotta, P.V. Giaquinta, R.C. Ponterio, S. Prestipino, F. Saija, G. Salvato, C. Vasi, Supercooled water escaping from metastability, Scientific Reports. 4 (2014) 7230. https://doi.org/10.1038/srep07230.

[46] S. Chavan, D. Park, N. Singla, P. Sokalski, K. Boyina, N. Miljkovic, Effect of latent heat released by freezing droplets during frost wave propagation, Langmuir. (2018). https://doi.org/10.1021/acs.langmuir.8b00916.

[47] S. Jung, M.K. Tiwari, D. Poulikakos, Frost halos from supercooled water droplets, Proceedings of the National Academy of Sciences U S A. 109 (2012) 16073–16078. https://doi.org/10.1073/pnas.1206121109.

[48] L. Yin, Q. Xia, J. Xue, S. Yang, Q. Wang, Q. Chen, In situ investigation of ice formation on surfaces with representative wettability, Applied Surface Science. 256 (2010) 6764–6769. https://doi.org/10.1016/j.apsusc.2010.04.086.

[49] F. Feuillebois, A. Lasek, P. Creismeas, F. Pigeonneau, A. Szaniawski, Freezing of a subcooled liquid droplet, Journal of Colloid and Interface Science. 169 (1995) 90–102. https://doi.org/10.1006/jcis.1995.1010.

[50] S. Tabakova, F. Feuillebois, On the solidification of a supercooled liquid droplet lying on a surface, Journal of Colloid and Interface Science. 272 (2004) 225–234. https://doi.org/10.1016/j.jcis.2003.10.029.

[51] L. Huang, Z. Liu, Y. Liu, Y. Gou, L. Wang, Effect of contact angle on water droplet freezing process on a cold flat surface, Experimental Thermal and Fluid Science. 40 (2012) 74–80. https://doi.org/10.1016/j.expthermflusci.2012.02.002.

[52] Z. Jin, S. Jin, Z. Yang, Visualization of icing process of a water droplet impinging onto a frozen cold plate under free and forced convection, J Vis. 16 (2013) 13–17. https://doi.org/10.1007/s12650-012-0154-x.

[53] L. Karlsson, A numerical and experimental investigation of the internal flow of a freezing water droplet, DIVA. (2015). http://urn.kb.se/resolve?urn=urn:nbn:se:ltu:diva-17930 (accessed August 9, 2018).

[54] T.V. Vu, G. Tryggvason, S. Homma, J.C. Wells, Numerical investigations of drop solidification on a cold plate in the presence of volume change, International Journal of Multiphase Flow. 76 (2015) 73–85. https://doi.org/10.1016/j.ijmultiphaseflow.2015.07.005.

[55] J.H. Snoeijer, P. Brunet, Pointy ice-drops: How water freezes into a singular shape, American Journal of Physics. 80 (2012) 764–771. https://doi.org/10.1119/1.4726201.

[56] A.G. Marín, O.R. Enríquez, P. Brunet, P. Colinet, J.H. Snoeijer, Universality of tip singularity formation in freezing water drops, Physics Review Letters. 113 (2014) 054301. https://doi.org/10.1103/PhysRevLett.113.054301.

[57] H. Zhang, Y. Zhao, R. Lv, C. Yang, Freezing of sessile water droplet for various contact angles, International Journal of Thermal Sciences. 101 (2016) 59–67. https://doi.org/10.1016/j.ijthermalsci.2015.10.027.

[58] X. Zhang, X. Liu, X. Wu, J. Min, Simulation and experiment on supercooled sessile water droplet freezing with special attention to supercooling and volume expansion effects, International Journal of Heat and Mass Transfer. 127 (2018) 975–985. https://doi.org/10.1016/j.ijheatmasstransfer.2018.07.021.

[59] An icing physics study by using lifetime-based molecular tagging thermometry technique, International Journal of Multiphase Flow. 36 (2010) 672–681. https://doi.org/10.1016/j.ijmultiphaseflow.2010.04.001.

[60] Y. Wang, Z. Wang, Sessile droplet freezing on polished and micro-micro-hierarchical silicon surfaces, Applied Thermal Engineering. 137 (2018) 66–73. https://doi.org/10.1016/j.applthermaleng.2018.03.068.

[61] T.V. Vu, Fully resolved simulations of drop solidification under forced convection, International Journal of Heat and Mass Transfer. 122 (2018) 252–263. https://doi.org/10.1016/j.ijheatmasstransfer.2018.01.124.

[62] R.J. Cheng, Water drop freezing: ejection of microdroplets, Science. 170 (1970) 1395–1396.

[63] T.V. Vu, G. Tryggvason, S. Homma, J.C. Wells, Numerical investigations of drop solidification on a cold plate in the presence of volume change, International Journal of Multiphase Flow. 76 (2015) 73–85. https://doi.org/10.1016/j.ijmultiphaseflow.2015.07.005.

[64] J.B. Dooley, Determination and characterization of ice propagation mechanisms on surfaces undergoing dropwise condensation, Thesis, 2011. http://oaktrust.library.tamu.edu/handle/1969.1/ETD-TAMU-2010-05-8038 (accessed June 11, 2018).

[65] J. Guadarrama-Cetina, A. Mongruel, W. González-Viñas, D. Beysens, Percolation-induced frost formation, Europhysics Letters. 101 (2013) 16009. https://doi.org/10.1209/0295-5075/101/16009.

[66] J. Petit, E. Bonaccurso, General Frost Growth Mechanism on solid substrates with different stiffness, Langmuir. 30 (2014) 1160–1168. https://doi.org/10.1021/la404084m.

[67] S. Nath, J.B. Boreyko, On localized vapor pressure gradients governing condensation and frost phenomena, Langmuir. 32 (2016) 8350–8365. https://doi.org/10.1021/acs.langmuir.6b01488.

[68] R. Le Gall, J.M. Grillot, C. Jallut, Modelling of frost growth and densification, International Journal of Heat and Mass Transfer. 40 (1997) 3177–3187. https://doi.org/10.1016/S0017-9310(96)00359-6.

[69] K.-S. Lee, S. Jhee, D.-K. Yang, Prediction of the frost formation on a cold flat surface, International Journal of Heat and Mass Transfer. 46 (2003) 3789–3796. https://doi.org/10.1016/S0017-9310(03)00195-9.

[70] D.-K. Yang, K.-S. Lee, Dimensionless correlations of frost properties on a cold plate, International Journal of Refrigeration. 27 (2004) 89–96. https://doi.org/10.1016/S0140-7007(03)00118-X.

[71] H. Asakawa, G. Sazaki, K. Nagashima, S. Nakatsubo, Y. Furukawa, Two types of quasi-liquid layers on ice crystals are formed kinetically, Proceedings of the National Academy of Sciences U.S.A. 113 (2016) 1749–1753. https://doi.org/10.1073/pnas.1521607113.

[72] B. Na, R.L. Webb, New model for frost growth rate, International Journal of Heat and Mass Transfer. 47 (2004) 925–936. https://doi.org/10.1016/j.ijheatmasstransfer.2003.09.001.

[73] B. Na, R.L. Webb, Mass transfer on and within a frost layer, International Journal of Heat and Mass Transfer. 47 (2004) 899–911. https://doi.org/10.1016/j.ijheatmasstransfer.2003.08.023.

[74] A. El Cheikh, A. Jacobi, A mathematical model for frost growth and densification on flat surfaces, International Journal of Heat and Mass Transfer. 77 (2014) 604–611. https://doi.org/10.1016/j.ijheatmasstransfer.2014.05.054.

[75] B. Na, R.L. Webb, A fundamental understanding of factors affecting frost nucleation, International Journal of Heat and Mass Transfer. 46 (2003) 3797–3808. https://doi.org/10.1016/S0017-9310(03)00194-7.

[76] F.R. Loyola, V.S. Nascimento, C.J.L. Hermes, Modeling of frost build-up on parallel-plate channels under supersaturated air-frost interface conditions, International Journal of Heat and Mass Transfer. 79 (2014) 790–795. https://doi.org/10.1016/j.ijheatmasstransfer.2014.08.055.

[77] C. Schäfle, P. Leiderer, C. Bechinger, Subpattern formation during condensation processes on structured substrates, Europhysics Letters. 63 (2003) 394–400. https://doi.org/10.1209/epl/i2003-00540-7.

[78] L. Mishchenko, M. Khan, J. Aizenberg, B.D. Hatton, Spatial control of condensation and freezing on superhydrophobic surfaces with hydrophilic patches, Advanced Functional Materials. 23 (2013) 4577–4584. https://doi.org/10.1002/adfm.201300418.

[79] Aurélia Léoni, M. Mondotbm, F. Durierbm, R. Revellinam, P. Haberschill, State-of-the-art review of frost deposition on flat surfaces, International Journal of Refrigeration. 68 (2016) 198–217. https://doi.org/10.1016/j.ijrefrig.2016.04.004.

[80] J. Guadarrama-Cetina, A. Mongruel, W. González-Viñas, D. Beysens, Frost formation with salt, Europhysics Letters. 110 (2015) 56002. https://doi.org/10.1209/0295-5075/110/56002.

[81] K. Carpenter, V. Bahadur, Saltwater icephobicity: Influence of surface chemistry on saltwater icing, Scientific Reports. 5 (2015) 17563. https://doi.org/10.1038/srep17563.

[82] J. Guadarrama-Cetina, R.D. Narhe, D.A. Beysens, W. González-Viñas, Droplet pattern and condensation gradient around a humidity sink, Physics Review E. 89 (2014) 012402. https://doi.org/10.1103/PhysRevE.89.012402.

[83] X. Sun, K. Rykaczewski, Suppression of frost nucleation achieved using the nanoengineered integral humidity sink effect, ACS Nano. 11 (2017) 906–917. https://doi.org/10.1021/acsnano.6b07505.

[84] J.E. Castillo, J.A. Weibel, A point sink superposition method for predicting droplet interaction effects during vapor-diffusion-driven dropwise condensation in humid air, International Journal of Heat and Mass Transfer. 118 (2018) 708–719. https://doi.org/10.1016/j.ijheatmasstransfer.2017.11.045.

[85] Y.O. Popov, Evaporative deposition patterns: Spatial dimensions of the deposit, Physics Review E. 71 (2005) 036313. https://doi.org/10.1103/PhysRevE.71.036313.

[86] S. Chavan, H. Cha, D. Orejon, K. Nawaz, N. Singla, Y.F. Yeung, D. Park, D.H. Kang, Y. Chang, Y. Takata, N. Miljkovic, Heat transfer through a condensate droplet on hydrophobic and nanostructured superhydrophobic surfaces, Langmuir. 32 (2016) 7774–7787. https://doi.org/10.1021/acs.langmuir.6b01903.

[87] A. Phadnis, K. Rykaczewski, The effect of Marangoni convection on heat transfer during dropwise condensation on hydrophobic and omniphobic surfaces, International Journal of Heat and Mass Transfer. 115 (2017) 148–158. https://doi.org/10.1016/j.ijheatmasstransfer.2017.08.026.

[88] Z. Pan, J.A. Weibel, S.V. Garimella, Influence of surface wettability on transport mechanisms governing water droplet evaporation, Langmuir. 30 (2014) 9726–9730. https://doi.org/10.1021/la501931x.

[89] ANSYS, Inc., ANSYS FLUENT 19.4 User's Guide, (2019).

[90] J.E. Castillo, J.A. Weibel, Predicting the growth of many droplets during vapor-diffusion-driven dropwise condensation experiments using the point sink superposition method, International Journal of Heat and Mass Transfer. 133 (2019) 641–651. https://doi.org/10.1016/j.ijheatmasstransfer.2018.12.068.

[91] B.J. Briscoe, K.P. Galvin, Growth with coalescence during condensation, Physics Review A. 43 (1991) 1906–1917. https://doi.org/10.1103/PhysRevA.43.1906.

[92] A. Steyer, P. Guenoun, D. Beysens, C.M. Knobler, Two-dimensional ordering during droplet growth on a liquid surface, Physics Review B. 42 (1990) 1086–1089. https://doi.org/10.1103/PhysRevB.42.1086.

[93] P. Meakin, Dropwise condensation: the deposition growth and coalescence of fluid droplets, Physics Scripta. 1992 (1992) 31. https://doi.org/10.1088/0031-8949/1992/T44/004.

[94] V.R. Voller, C. Prakash, A fixed grid numerical modelling methodology for convection-diffusion mushy region phase-change problems, International Journal of Heat and Mass Transfer. 30 (1987) 1709–1719. https://doi.org/10.1016/0017-9310(87)90317-6.

[95] V.R. Voller, C.R. Swaminathan, Eral source-based method for solidification phase change, Numerical Heat Transfer, Part B: Fundamentals. 19 (1991) 175–189. https://doi.org/10.1080/10407799108944962.

[96] V.R. Voller, M. Cross, N.C. Markatos, An enthalpy method for convection/diffusion phase change, International Journal for Numerical Methods in Engineering. 24 (1987) 271–284. https://doi.org/10.1002/nme.1620240119.

[97] D.M. Murphy, T. Koop, Review of the vapour pressures of ice and supercooled water for atmospheric applications, Quarterly Journal of the Royal Meteorological Society. 131 (2005) 1539–1565. https://doi.org/10.1256/qj.04.94.

[98] H. Wang, J.Y. Murthy, S.V. Garimella, Transport from a volatile meniscus inside an open microtube, International Journal of Heat and Mass Transfer. 51 (2008) 3007–3017. https://doi.org/10.1016/j.ijheatmasstransfer.2007.09.011.

[99] Z. Pan, S. Dash, J.A. Weibel, S.V. Garimella, Assessment of water droplet evaporation mechanisms on hydrophobic and superhydrophobic substrates, Langmuir. 29 (2013) 15831–15841. https://doi.org/10.1021/la4045286.

[100] S.H. Tirmizi, W.N. Gill, Effect of natural convection on growth velocity and morphology of dendritic ice crystals, Journal of Crystal Growth. 85 (1987) 488–502. https://doi.org/10.1016/0022-0248(87)90482-9.

[101] J.S. Langer, R.F. Sekerka, T. Fujioka, Evidence for a universal law of dendritic growth rates, Journal of Crystal Growth. 44 (1978) 414–418. https://doi.org/10.1016/0022-0248(78)90007-6.

[102] W.J. Boettinger, J.A. Warren, The phase-field method: simulation of alloy dendritic solidification during recalescence, Metallurgical and Materials Transactions A. 27 (1996) 657–669. https://doi.org/10.1007/BF02648953.

[103] S. Jung, M. Dorrestijn, D. Raps, A. Das, C.M. Megaridis, D. Poulikakos, Are superhydrophobic surfaces best for icephobicity?, Langmuir. 27 (2011) 3059–3066. https://doi.org/10.1021/la104762g.

[104] S. Chavan, D. Park, N. Singla, P. Sokalski, K. Boyina, N. Miljkovic, Effect of latent heat released by freezing droplets during frost wave propagation, Langmuir. 34 (2018) 6636–6644. https://doi.org/10.1021/acs.langmuir.8b00916.

[105] W. Kong, H. Liu, A theory on the icing evolution of supercooled water near solid substrate, International Journal of Heat and Mass Transfer. 91 (2015) 1217–1236. https://doi.org/10.1016/j.ijheatmasstransfer.2015.08.005.

[106] A. Chandramohan, J.A. Weibel, S.V. Garimella, Spatiotemporal infrared measurement of interface temperatures during water droplet evaporation on a nonwetting substrate, Applied Physics Letters. 110 (2017) 041605. https://doi.org/10.1063/1.4975003.

[107] A. Wexler, Vapor pressure formulation of ice, Journal of Research of the National Institute of Standards and Technology Section A, Physics and Chemistry. 81 A (1977) 5–20. https://doi.org/10.6028/jres.081A.003.

[108] A. Wexler, Vapor Pressure Formulation for Water in Range 0 to 100 °C, Journal of Research of the National Institute of Standards and Technology Section A, Physics and Chemistry. 81 A (1977) 5–20. https://doi.org/10.6028/jres.081A.003.

[109] P.M. Morse, H. Feshbach, G.P. Harnwell, Methods of Theoretical Physics, Part I, McGraw-Hill Book Company, Boston, Mass, 1953.

VITA

Julian Castillo received his Bachelor of Science (BS) in Mechanical Engineering from Universidad del Valle in 2009 and his Master of Science (MSME) in Mechanical Engineering in 2014 from Purdue University. He is currently pursuing a PhD in Mechanical Engineering at Purdue University under the advisement of Dr. Justin A. Weibel. For his PhD studies he was awarded a Colciencias-Fulbright Scholarship. His research interests focus on understanding phase change phenomena with applications in heat transfer.

PUBLICATIONS

J. E. Castillo, J. A. Weibel, and S. V. Garimella, "The effect of relative humidity on dropwise condensation dynamics," International Journal of Heat and Mass Transfer, vol. 80, pp. 759–766, 2015.

J. E. Castillo and J. A. Weibel, "A point sink superposition method for predicting droplet interaction effects during vapor-diffusion-driven dropwise condensation in humid air," International Journal of Heat and Mass Transfer, vol. 118, pp. 708–719, 2018.

J.E. Castillo, J.A. Weibel, Predicting the growth of many droplets during vapor-diffusion-driven dropwise condensation experiments using the point sink superposition method, International Journal of Heat and Mass Transfer. 133 (2019) 641–651.

J. E. Castillo, Yanbo Huang, Zhenhai Pan, and J. A. Weibel, "Quantifying the pathways of latent heat dissipation during droplet freezing on cooled substrates" (Submitted for publication, in review).

J. E. Castillo, Yanbo Huang, Zhenhai Pan, and J. A. Weibel, "Asymmetrical solidification during droplet freezing in the presence of a neighboring droplet" (Submitted for publication, in review).